2024-07

Spatio-Temporal Variability Of Aerosols Over East Africa-Ethiopia Using Modis Satellite Data

Ambachew, Abeje

SPATIO-TEMPORAL VARIABILITY OF AEROSOLS OVER EAST AFRICA-ETHIOPIA USING MODIS SATELLITE DATA

By:

Ambachew Abeje Alemu

A THESIS SUBMITTED TO THE SCHOOL OF GRADUATE STUDIES
IN THE PARTIAL FULFILLMENT OF THE REQUIREMENTS FOR
THE DEGREE OF DOCTOR OF PHILOSOPHY IN ATMOSPHERIC PHYSICS
AT
BAHIR DAR UNIVERSITY
BAHIR DAR, ETHIOPIA
30 JULY 2024

BAHIR DAR UNIVERSITY

SCHOOL OF GRADUATE STUDIES

DEPARTMENT OF PHYSICS

Supervisor:

Dr. U. Jaya Prakash Raju
Assistant Professor in Atmospheric Physics
Department of Physics, Bahir Dar University, Ethiopia

Examiners:

Chairman:

Dr. Tamiru Negussie Wondim(**HoD**)
Associate Professor in Solid State Physics
Department of Physics, Bahir Dar University, Ethiopia

BAHIR DAR UNIVERSITY

Date: **30 July 2024**

Author: **Ambachew Abeje Alemu**

Title: **Spatio-Temporal Variability of Aerosols Over East Africa-Ethiopia Using MODIS Satellite Data**

Department: **Physics**

Degree: **PhD** Convocation: **24 June** Year: **2024**

Permission is herewith granted to Bahir Dar University to circulate and to have copied for non-commercial purposes, at its discretion, the above title upon the request of individuals or institutions.

Signature of Author

Dedicated with Love to my:

*Wife Dasash Tiruneh Guadie '**TiG**',*

*Daughters Tsion '**TiT**'and Elsabet '**ElS**'Ambachew*

*and Mother Emahoy Mullu Ayalew Tassew '**MaM**'!*

Table of Contents

List of Tables

List of Figures

List of Acronyms

3B43 Monthly Precipitation Estimates

AA The Addis Ababa Site

AB The Aseb Port Site

ACPIs Aerosol-Cloud-Precipitation Interactions

AE, AET Ångström Exponent

AIC Akaike Information Criterion

AOD Aerosol Optical Depth

ARI Aerosol-Radiation Interactions

AS Awassa Site

AW The Agnuak Site

AWV Atmospheric Water Vapor

BB Biomass Burning Aerosol Types

BC Black Carbon

BD The Bahir Dar Site

C_2H_2 Acetylene Molecule

CERES Clouds and the Earth‘s Radiant Energy System

CFM Mean Cloud Fraction

CCN Cloud Condensation Nuclei

COA Spatial Correlation of AOD with AET

COF Spatial Correlation of AOD with CFM

COP Spatial Correlation of AOD with CTP

COT Spatial Correlation of AOD with CTT

COW Spatial Correlation of AOD with AWV

Cp The Specific Heat Capacity at Constant Pressure

CrIS Cross-track Infrared Sounder

CTP Cloud Top Pressure

CTT Cloud Top Temperature

CV Coefficient of Variance

DD Desert Dust Aerosol Types

DJ, DT The Djibouti Site

DG The Dangote Site

DL The Dahlak Island Site

DS Dust Aerosol Types

EA The Erta Ale Site

EAE East Africa-Ethiopia

E Geographical Eastern Hemisphere

EC Elemental Carbon

ED The Great Ethiopia Renascence Dam Site

EOS Earth Observing System

ER Eritrea

ETC Etcetera

Fig Figure

$\mathbf{F_{TOA}}$ Top of Atmosphere Radiative Forcing

$\mathbf{F_{Surf}}$ Surface Radiative Forcing

$\mathbf{F_{CLR}}$ Aerosol-free Radiative Forcing

$\mathbf{F_{AER}}$ Cloud-free Aerosol Radiative Forcing

$\mathbf{F_{Atm}}$ Atmospheric Radiative Forcing

H Hydrogen Atom

$\mathbf{H_2O}$ Water Molecule

$\mathbf{H_2SO_4}$ Sulfuric Acid

HDF Hierarchical Data Format

HIRS High-Resolution Infrared Radiation Sounder

$\mathbf{HNO_3}$ Nitric Acid

HoD Head of Department

hPa hecto-Pascal

HR The Humera Site

HYSPLIT HYbrid Single-Particle Lagrangian Integrated Trajectory

IASI Infrared Atmospheric Sounding Interferometer

IN The Ice Nuclei

JB The Juba Site

K The Kernel-Kelvin

KC The Kombolcha Site

KD The Kebri Dahar Site

km^2 Square Kilo Meters

E(t) The Mann-Kendall Distribution

S(t) The Mann-Kendall Statistic Test

Z(t) The Mann-Kendall Transformation

Var(t) The Mann-Kendall Variance

MATLAB MAtrix LABoratory

MLR Multiple Linear Regression

MODIS Moderate Resolution Imaging Spectroradiometer

MOD04_3K Swath 3km Resolution MODIS Terra Level-2 Daily Collection 61 Product

MOD08_M3–61 Gridded MODIS Terra Level-3 Monthly Collection 61 Global Product

MPL Micro-Pulse Lidar

MR Marine Aerosol Types

MSc Master of Sciences

MX Mixed Aerosol Types

MYD04_3K Swath 3km Resolution MODIS Aqua Level-2 Daily Collection 61 Product

MYD08_M3–61 Gridded MODIS Aqua Level-3 Monthly Collection 61 Global Product

N Geographical Northern Hemisphere

NASA National Aeronautics and Space Administration

NASDA National Space Development Agency

NH_3 Ammonia Molecule

NOAA National Oceanic and Atmospheric Administration

NO Nitric Oxide

i,n Number of Observations

O_2 Oxygen Molecule

O_3 Ozone Molecule

OA Organic Aerosols

OC Organic Carbon

OLR Out-going Long-wave Radiation

P Pressure

PBAPs Primary Biological Aerosol Particles

PCs, PCA Principal Component Analysis

PDF Portable Document Format

PhD Doctor of Philosophy

PM Particulate Matter

POA Primary Organic Aerosols

PPT Precipitation

QQ Quantile-Quantile

REOFs Rotation of Empirical Orthogonal Functions

RF Radiative Forcing

RG The Raga Site

S Geographical Southern Hemisphere

SAGE Stratospheric Aerosol and Gas Experiment

S-NPP Suomi National Polar-Orbiting Partnership

SO_2 Sulfur Dioxide

SOA Secondary Organic Aerosols

SPM Suspended Particulate Matter

SS South Sudan

SSE Sum of Squared Errors

F_{down} Surface Reaching Solar Intensity

T Temperature in Kelvin

t Time in Second

TG The Tonga Site

TOA Top of Atmosphere

TRMM Tropical Rainfall Measuring Mission

TSP Total Suspended Particulate

TSPM Total Suspended Particulate Matter

F_{up} The Up-scattered Solar Radiation

UR Urban Aerosol Types

UV Ultra-Violet

VIFs Variable Inflation Factors

W Geographical Western Hemisphere

Wm^{-2} Watt Per Meter Square

List of Symbols

τ Aerial Mean Optical Depth

$\mathbf{x}_i$ The AOD Values

$\bar{\mathbf{x}}$ Average of the AOD Values

h The Bandwidth

π Circumference to Diameter Ratio of Circle

β Coefficient of Regression-Turbidity

Δ The Change Symbol

$\mathbf{A}_c$ Cloud Cover Fractional

$^{\mathbf{0}}$ The Degree Symbol

$\bar{R}_s$ The Mean Albedo of Underlying Surface

μ One Millionth 10^{-6}

% The Percentage Symbol

R Coefficient of Correlation

e Expositional Function

g The Gravitational Acceleration

$\bar{\beta}$ Radiation Fraction Scattered by Aerosol Column

ϕ_e^{i-t} Received-Transmitted Spectral Radiant Flux

sgn The Sign of Real Number

ln Natural Logarithm

$\mathbf{F}_T$ The Solar Constant 1370 W/m^2

T_λ Spectral Transmittance in Wavelength

$\mathbf{S}_d$ Standard Deviation

$\sum$ The Summation Symbol

$\hat{f}_n(y)$ Traditional Kernel Estimator Function

λ Wavelength

List of Publications

Alemu, A. A. and Raju, J. P.: Classification of Aerosol Particles and Their Temporal Distribution Over East Africa–Ethiopia Using MODIS Satellite Data: Part 01, Journal of Quantitative Spectroscopy & Radiative Transfer JQSRT, Elsevier, 325, 109085, 2024.

Alemu, A. A. and Raju, J. P.: Long–Term Trend Analysis and Spatial Distribution of Aerosol Particles Over East Africa–Ethiopia Using MODIS Satellite Data: Part 02, Journal of Atmospheric & Solar-Terrestrial Physics JASTP, Elsevier, X, XXX–XXX, 2024.

Alemu, A. A. and Raju, J. P.: Effects of Aerosol Particles on Precipitation and Cloud Parameters Over East Africa-Ethiopia Using MODIS Satellite Data: Part 01, Ethiopian Journal of Science and Technology EJST, African Journals Online, 17(1), 029–056, 2024.

Alemu, A. A. and Raju, J. P.: Correlation of Aerosol Particles with Clouds and Radiation Budget Over East Africa-Ethiopia Using MODIS Satellite Data: Part 02, Journal of Quantitative Spectroscopy & Radiative Transfer JQSRT, Elsevier, X, XXX–XXX, 2024.

Seminars and Conferences

Training Attendance on: Second Summer School on Space Research, Technology and Applications for young scientists and PhD students, National Astronomical Observatory Rozhen, Bulgaria, 3-10 July 2022.

Alemu, A. A. and Raju, J. P.: Classification of Aerosol Particles and Their Temporal Distribution Over East Africa–Ethiopia Using MODIS Satellite Data: Part 01, Journal of Quantitative Spectroscopy & Radiative Transfer JQSRT, Elsevier, 325, 109085, 2024.

Alemu, A. A. and Raju, J. P.: Effects of Aerosol Particles on Precipitation and Cloud Parameters Over East Africa-Ethiopia Using MODIS Satellite Data: Part 01, Ethiopian Journal of Science and Technology EJST, African Journals Online, 17(1), 029–056, 2024.

General Abstract

Aerosols are tiny mixtures of liquid-solid particulate matter suspended in the atmosphere that play significant roles in human health and climate dynamics, directly, indirectly, and semi-directly. There have been large spatiotemporal variations in the optical properties of aerosols, clouds, precipitation, and radiation due to environmental and meteorological conditions, industrial and agricultural influences, and other human and natural influences in each ecological functional area.

This study was conducted on the spatiotemporal variability of aerosols in sixteen selected stations clustered into four regions over East Africa-Ethiopia using satellite-based data that have not yet been studied for periods 2001–2022. This PhD thesis work reports the spatiotemporal variability of aerosol particles and their optical interactions with the cloud parameters and radiation budget over East Africa, with particular interest in Ethiopia. The study covers sixteen selected stations in East Africa-Ethiopia with neighbouring doughters Eritrea, Djibouti, and South Sudan countries clustered into four regions for the periods of 2001–2022 to obtain detailed information on the spatiotemporal behaviours of aerosol particles and their effects on clouds and radiation budget. The aerosol optical parameters, Ångström exponent AET calculated from the aerosol optical depth AOD, cloud top pressure CTP, cloud top temperature CTT, mean cloud fraction MCF, and atmospheric water vapor AWV were extracted from the Moderate Resolution Imaging Spectroradiometer MODIS satellite data. We collected precipitation PPT data from the Tropical Rainfall Measuring Mission TRMM, and outgoing long-wave radiation OLR flux is collected using clouds and the Earth's Radiant Energy System CERES satellites.

According to the results, there is a significant variation in the daily AOD and AET, with maximum values most likely occurring between August 11 and September 15 for Aqua and between June 22 and July 24 for both Terra and Aqua in the southeast and northeast clusters. The results range from 0.00 to 2.10 and 0.67 to 1.23. The OLR, CTP, and CTT parameters are out of phase with AOD and increase-decrease swings with AET,

AWV, CFM, and PPT. The majority of the parameters are focused on the southwest's western region of the research area. The maximum values from the northeast cluster in 2010 for AOD, AWV, and CFM; in 2009 for PPT; in 2011 and 2022 for CTP and CTT for both instruments; and in 2022 for all AOD, AWV, and CFM have their minimum at the southeast cluster in 2022.

Appropriate AOD and AET thresholds were used to classify the aerosol types into marine MR, dust DS, biomass burning BB, desert dust DD, urban UR, and the residual cases were considered mixture MX types. The marine aerosol particles show the most abundance at 47.71%, followed by urban aerosol particles at 28.29%, while desert dusts, enriched at 14.65%, accounted for the third place with free of dust particles. The Mann-Kendall statistical trend test was applied to the annual time series in all clustered regions, which reveals an almost positive increase in variability accompanied by a slight decrease in the forward series, and vice-versa. The parameters OLR and AWV had the lowest optimum significant PCs at the Humera and Dahlak sites, whereas the highest PCs were retained based on AET at the Awassa site and AWV at the Dangote site. Differences in the retained PCs indicate that distinct atmospheric dynamics are responsible for the behavior of the climate during different seasons of the year as well as the spatial coherence arising from intraseasonal and interannual variability. Furthermore, fire map analysis and the HYSPLIT model demonstrate that transported aerosols in East-African climate exhibit a variety of source regions, primarily the Arebian desert and southwest Indian Ocean.

The majority of the southwest study area regions show a western orientation for the spatial correlations. The clustered regions exhibit radiative forcing minimum at the southwest cluster for all F_{Surf} and at the southeast cluster for F_{TOA} in 2012. Their peaks for F_{Surf} and F_{TOA} from both instruments occur at the northwest cluster in 2022. As a result, the maximum are -0.58 and 63.80 Wm^{-2} for Terra and -1.37 and 58.83 Wm^{-2} for Aqua, and the minimum values are -23.83 and 8.37 Wm^{-2} for Terra and -22.95 and 7.68 Wm^{-2} for Aqua. In comparison with the northern clusters, the values for the parameters were greater in the southern clusters, more precisely in the southwest clusters. In the regression analysis, the AET was the most dominant variable with $0.02733<\beta_1<15.17547$, whereas the CFM was less influential. The study area regions exhibited optimal performance values throughout all seasons, with $0.93941<R<0.99958$. While their maximums are from Terra in Kiremt at Bahir Dar and in Tseday at Agnuak, the minimum values recorded in Bega at Kombolcha are from Aqua for both the dominant β_1 and performance R.

Acknowledgments

A humble expression of the deep debt of gratitude which once feels in once heart, but since there is no other word which can better express once feeling of gratitude than thanks. Above all, I would like to thank the **Almighty God** for His unreserved gift. "Trust in the Lord with all your heart. Do not put your confidence in your own understanding. In all your way acknowledge Him and He will direct your path" Proverbs 3:5-6. In this opportunity, I can't separate Saint Virgin Merry from thanking you for every good step. First and foremost, I would like to thank my supervisor, **Dr U Jaya Prakash Raju** for his valuable insight, direction, encouragement, and guidance throughout these years. It is with great and heartfelt appreciation that I thank **Dr UJP Raju** not only for sharing his deep wisdom, experience, and enlightening brotherhood discussion all the way through from the beginning but also for his tireless effort, commitment, and great contribution to advance Atmospheric Sciences in Bahir Dar University in particular and throughout the country at large. I would also like to express my admiration and thanks for his constant dedication, invaluable advise, thoughtful comments, and tremendous mentorship for the successful completion of this PhD study.

The authors would like to thank all anonymous reviewers for their time, expertise in making a thorough revision, and constructive comments, which greatly helped improve the quality of the manuscripts that are included in Part II of this dissertation. Warmly, we would like to thank the NASDA-NASA HDF-EOS Tools and Information Center Help Team for providing the MODIS, TRMM and CERES data on aerosol-cloud-precipitation parameters interactions. We also thank all institutions around the world that maintain and allow public access to the observational, reanalysis, reconstruction, and other datasets used in this study.

Special thanks go to the school of graduate studies at Bahir Dar University for accepting my application as a PhD student, and particularly to the academic and administrative staff of the physics department. I would also like to thank the previous and current

department heads, Dr Getasew Admasu, Dr Tesfaye Dagne, and Dr Tamiru Nigussie, for their consistent help and support and for every opportunity for the successful completion of my work. A special mention and thanks are also given to the department secretary, Wro Selam Berihun, for her efforts in facilitating my dealings with the department and providing resources and research facilities.

I heartily acknowledge Debre Tabor University for offering me the opportunity of my study leave and their consistent financial support over the last five years for the PhD fellowship, in general, for investing so much resource to train me as a part of academic staff development. I would also like to thank all the physics staff and the previous as well as current department heads at the university for their experience sharing, consistent help and support, and providing resources and research facilities.

In this opportunity, I would like to thank all my school teachers from the beginning grade up to this end in general, with special thanks to my elementary school science teacher Mr Mezgebu Mekonnen, my MSc teacher and advisor Prof Gizaw Mengistu, and Advaced and Computational Statistical Methods teacher in my PhD studies Dr Melsew Nigussie. Confidentially, I can say that those specially mentioned teachers made the basement, building, and roof for my academic journey.

This dissertation work is dedicated to my incredibly wonderful wife, Wro Dasash Tiruneh, who has been a constant source of support and encouragement during the challenges of my research, and my daughters, Tsion Ambachew and Elsabet Ambachew, who have always been a source of inspiration over the years to get me to where I am now through your tolerable encouragement.

Lastly, I would like to pay tribute to my parents, officemates, classmates, and friends for their continuing support and tolerance. I thank my mother, brothers, and sister, who have been a source of strength and motivation from the beginning, and all the people who supported me with this dissertation.

Ambachew Abeje Alemu

Bahir Dar, Ethiopia

July, 2024

Chapter 1

INTRODUCTION

Our planet Earth consists of the atmosphere, hydrosphere, cryosphere, land surface and biosphere, a complex system interacting with physical, chemical and biological processes that acts like a natural laboratory (Council et al., 2001; Kerényi et al., 2020). For this PhD research work, satellite-based remote sensing techniques were employed over East Africa-Ethiopia to explore the spatiotemporal variability of aerosol particles and their interactions with the radiation budget. The PhD thesis dissertation introduction aims to provide background to the study, statement of the problem, study objectives and outlines.

1.1 Background of the Study

The term "aerosol" in Amharic "binagn" comes from the two Greek words, namely "aero" to mean an air and "sol", which is to mean a solution. In atmospheric physics, the terms "aerosol" and "aerosol particle" are often used interchangeably with each other. In this terminology, atmospheric aerosols are all particles in the atmosphere larger than the most common air molecules and smaller than the cloud droplets. Atmospheric aerosol particles differed in their sources, sizes, shapes and compositions, with lifetimes depending on their origin and subsequent atmospheric processing (Grythe, 2017; Kafle and Coulter, 2013). The aerosol particles consist of the solid-liquid particulate materials that are suspended in the air. They are present everywhere in the atmosphere and are seen as dust and smoke

haze that originate from both natural and human sources. Dust and sea salt are the most common natural sources worldwide. At the local-regional levels, the industrialized and highly populated regions are dominated by aerosol particles of anthropogenic origin, such as from different fired combustion sources and intense biomass burning (Joksić et al., 2009; Arfin et al., 2023; Querol et al., 2006). Primarily, atmospheric aerosol particles could be emitted from the Earth to atmosphere through natural and anthropogenic sources, which include biomass burning, the incomplete combustion of fossil fuels, volcanic eruptions, wind-driven or traffic-related suspension of the road, soil, mineral dust, sea salt, sand and biological materials. The chemical reactions through the atmosphere are also secondary sources for the aerosol particles (Chi et al., 2019; Behera, 2016; Gaffney et al., 2006a).

The aerosol particles have effects on human health and the atmosphere. They affect the atmosphere by altering the properties of the radiation energy budget directly through scattering and absorbing solar radiation, indirectly through affecting the cloud properties and semi-directly in such a way that the absorbed radiation energy by aerosol particles would increase the temperature of the surrounding air, then resulting in the evaporation of cloud droplets (Kaufman et al., 2000a; Li et al., 2021a). Those effects on the atmosphere are characterized using the Ångström exponent AE, which determines the size distribution of the aerosol particles and the aerosol optical depth AOD, which deals with their loading concentrations. The concentrations and distributions of atmospheric aerosol particles are highly variable in space and time. The spatio-temporal variability of the aerosol optical depth AOD and its size distribution AE are influenced by many environmental factors, such as meteorological condition changes, atmospheric pollution and topographic changes. Therefore, observing the atmospheric trace gases and suspended aerosol particles has become the global issue for which the observation findings are used for environmental policymakers as evidence (Kokhanovsky, 2008; Loeb et al., 2018).

The spatio-temporal distribution of aerosol particles in the free troposphere is important for estimating their impact on climate. To be able to correctly interpret and understand

the climate change, there is a need to understand and quantify the impact of aerosol particles on cloud parameters and the radiation budget (Rahman, 2023). This can only be effectively done through focusing on their relationship and the response to large-scale weather systems. Those of the cloud parameters focused on include: the amount of water dissolved in the air, which is called atmospheric water vapor AWV; the fraction of the atmosphere occupied by clouds, which is known as the mean cloud fraction CFM; the location of the radiating top of the clouds, called cloud top pressure CTP; and the cloud top temperature CTT, which is the atmospheric temperature observed at the top of a cloud (Lee et al., 2007; Anderson et al., 2003; Myhre et al., 2007b). To understand their emissions and long-range transport patterns of the aerosol particles, the ground-based *in situ* remote sensing techniques with the space-borne observations are more essential. Instruments such as sunphotometers and surface Micro-Pulse Lidar MPL measurements can directly observe the vertical distribution of aerosol particles in the free troposphere (Liou, 2002; Jian-Ping et al., 2008). The atmospheric monitoring from the satellites is the key method in the local-regional-global monitoring of the air pollutions with temporally continuous datasets (Kaufman et al., 1990; Tian et al., 2023; Park et al., 2023). The Fire-Map and the Hybrid Single-Particle Lagrangian Integrated Trajectory HYSPLIT Models were used to compute the trajectory of aerosol particles dispersion and disposition simulations (Ngaina, 2015; Draxler and Rolph, 2003).

Ethiopia is a neighbor to marine countries like Eritrea and Djibouti, which can be exposed to oceanic dusts. And also, Ethiopia is undergoing a boom of infrastructural development, like an increase in urbanization, which comes with a boom of development like building and road constructions, expansion of industries, traffic density etc, which contributes to air pollution by different ways (Lenhardt and Oppenheimer, 2014; Apollo and Mbah, 2021; Marchand et al., 2017). Due to those facts and activities, solid materials, loading into the atmosphere, mostly the dusts and minerals. The accumulation of these particulate matters affects the country's solar energy budget, health, visibility, etc. This needs scientific

observation to quantify their optical parameters. Hence, it is the right time to give the right attention to air quality and climate change impacts, as they are the nightmare issues nowadays. In the previous studies, there were very few studies on atmospheric aerosol particles over East Africa-Ethiopia. These includes Milkessa G. et al. (Homa et al., 2017), who studied stratospheric aerosol climatology from the SAGE II satellite over Ethiopia. In this study, the researchers focused more on stratospheric aerosol particles. However, most of the aerosol particles are found in the troposphere (Raes et al., 2000; Froyd et al., 2009). Anteneh G. (Getachew, 2009) had also studied aerosol microphysical and optical parameters derived from the sun photometer over Addis Ababa city only. But none of them had reported on the spatio-temporal variability of aerosols and their interactions with cloud parameters and radiation budget.

Therefore, to fill those gaps from the previous research works, this PhD dissertation study will focus on (I) the spatio-temporal variability of aerosol particles and (II) the interactions of the aerosol particles with cloud parameters, precipitation, and radiation budget over the eastern part of Africa-Ethiopia. The aerosol optical properties and the cloude parameters daily-monthly data were taken from satellite measurements using Moderate Resolution Imaging Spectroradiometer MODIS Terra and Aqua instruments. We extracted monthly precipitation PPT from the Tropical Rainfall Measuring Mission TRMM 3B43 data and calculated the out-going long-wave radiation flux OLR parameters using the Clouds and the Earth's Radiant Energy System CERES Terra and Aqua satellites.

1.2 Statements of the Problem

Over the past century, there has been a significant increase in both the natural as well as human-caused activities, which has led to a concentration of various trace gases and aerosol particles of anthropogenic origin in the atmosphere. This has been polluting the atmosphere and altered the Earth's climate (Taylor, 2008; Manisalidis et al., 2020;

Breitner-Busch et al., 2023). Now a days, the environmental change-variation with the space-time has become one of the most important local-regional-global issues in facing the society to observe the atmospheric composition and its process (Burrows et al., 2011; Chu and Karr, 2017). This is increasingly recognized as a critical challenge for the ecological health, human well-being and future development. Changing the chemical compositions and its process of the atmosphere have become the focus of heated scientific, political and social debates around the world.

Therefore, an understanding of the atmospheric compositions and their processes is needed to make correct decisions for future improvements (Ebner et al., 1999; Sitch et al., 2008). The understanding of the various aspects of climate change with space-time is based on new scientific evidence and research. In doing so, the scientists apply the principles of remote sensing techniques to collect atmospheric parameters from space-born and the *in situ* ground-based measurements in worldwide (Levelt et al., 2014; Bai et al., 2020; Balsamo et al., 2019). These kinds of studies are rare throughout East Africa, especially in Ethiopia. Our PhD dissertation study was inspired by the researchers' keen interest in monitoring space-time variations in the atmospheric aerosol particle composition and process over East Africa-Ethiopia.

1.3 The Research Questions

In this PhD work, the authors addressed the following main research questions:

1. What sizes of aerosol particles were observed over the East Africa-Ethiopia EAE?
2. Which types of aerosol particles are more prevalent in East Africa-Ethiopia EAE?
3. Which are the main sources of aerosol particle transportation to the EAE sectors?
4. Do the aerosol particles have an impact on the radiation budget over EAE sectors?

In our PhD dissertation, we developed and designed the following objectives in order to address the aforementioned questions:

1.4 Objectives of the Study

General Objective: the main objective of this PhD dissertation is to determine the spatiotemporal variability of aerosol particles and their effects on clouds and radiation budget over East Africa-Ethiopia using MODIS, TRMM, and CERES satellite data.

Specific Objectives: the specific objectives of the study are:

- ☞ To Classify Atmospheric Aerosol Particles and Their Temporal Distribution Over East Africa-Ethiopia Using MODIS Satellite Data,
- ☞ To Study Long-Term Trend Analysis and Spatial Distribution of Aerosol Particles Over East Africa-Ethiopia Using MODIS Satellite Data,
- ☞ To Study Effects of Aerosol Particles on Precipitation and Cloud Parameters Over East Africa-Ethiopia Using MODIS Satellite Data,
- ☞ To Investigate Correlation of Aerosol Particles with Clouds and Radiation Budget Over East Africa-Ethiopia Using MODIS Satellite Data.

1.5 Significance of the Study

Accurate quantification of the amounts of trace gases and particulate matters emitted from vegetation fires and other sources of biomass burning on a regional and global basis is required by a number of users, including scientists studying a wide range of atmospheric processes, national governments who are required to report greenhouse gas emissions, and those interested in quantifying the sources of the air pollution that affect human

health at regional scales. The contribution of this research is the provision of correlative measurements of atmospheric aerosol particles, which are useful for validating *in-situ* case measurements, unique scientific investigations, and climate models. Additionally, these measurements can be utilized by Ethiopian meteorology agencies.

1.6 Outlines of the Thesis

This PhD thesis work reports the spatiotemporal variability of aerosol particles and their optical interactions with the cloud parameters and radiation budget over East Africa, with particular interest in Ethiopia. The study covers sixteen selected stations in East Africa-Ethiopia with neighbouring doughters Eritrea, Djibouti, and South Sudan countries clustered into four regions for the periods of 2001–2022 to obtain detailed information on the spatiotemporal behaviours of aerosol particles and their effects on clouds and radiation budget. One of the major types of aerosol particles that contribute to the climate effect of aerosol particles in East Africa-Ethiopia is biomass burning and a larger percentage of this comes from India ocean neighboring countries like Egypt, Kenya and Arabian deserts (Negash, 2010). The research begins by describing the major atmospheric compositions, followed by the instruments used in this research work. Then the data and methods are clearly explained before the results and discussion parts are presented.

The thesis work focused largely on the sources, sinks, classifications, types, effects, and interactions of aerosol particles using satellite-based remote sensing instruments. The satellite-based instruments we have used for this study include the Moderate Resolution Imaging Spectroradiometer MODIS, Tropical Rainfall Measuring Mission TRMM, and Clouds and the Earth‘s Radiant Energy System CERES. The daily and monthly products of both the MODIS-CERES Terra and the Aqua, as well as the 25^0 x 25^0 TRMM 3B43, were employed in this study. In addition, other web-based software models like Fire-Maps and HYSPLIT trajectories are also employed.

In chapter 4, we studied classification of aerosol particles and their temporal distributions using MODIS satellite data over East Africa–Ethiopia. **This chapter can be cited as:**
Alemu, A. A. and Raju, J. P.: Classification of Aerosol Particles and Their Temporal Distribution Over East Africa–Ethiopia Using MODIS Satellite Data: Part 01, Journal of Quantitative Spectroscopy & Radiative Transfer JQSRT, Elsevier, 325, 109085, 2024.
In chapter 5, the optical parameters AOD and AE were extracted and calculated from MOD04_3K and MYD04_3K in order to gain detailed knowledge of the long-term trends of aerosol particles and their spatial distribution behaviors both seasonally and annually in East Africa–Ethiopia with its neighbors Eritrea, Djibouti, and South Sudan regions for the period 2001–2022. **This chapter is to be cited as:**
Alemu, A. A. and Raju, J. P.: Long–Term Trend Analysis and Spatial Distribution of Aerosol Particles Over East Africa–Ethiopia Using MODIS Satellite Data: Part 02, Journal of Atmospheric & Solar-Terrestrial Physics JASTP, Elsevier, X, XXX–XXX, 2024.
Chapter 6 reports the effects of atmospheric aerosol particles on the cloud parameters, precipitation, and radiation budget over East Africa-Ethiopia using MODIS, TRMM and CERES satellite data. **The Chapter is to be cited as:**
Alemu, A. A. and Raju, J. P.: Effects of Aerosol Particles on Precipitation and Cloud Parameters Over East Africa-Ethiopia Using MODIS Satellite Data: Part 01, Ethiopian Journal of Science and Technology EJST, African Journals Online, 17(1), 029–056, 2024.
In Chapter 7, we observed the correlation of aerosol particles with clouds and the radiation budget over East Africa-Ethiopia using the MODIS, TRMM and CERES satellite data. **The chapter is to be cited as:**
Alemu, A. A. and Raju, J. P.: Correlation of Aerosol Particles with Clouds and Radiation Budget Over East Africa-Ethiopia Using MODIS Satellite Data: Part 02, Journal of Quantitative Spectroscopy & Radiative Transfer JQSRT, Elsevier, X, XXX–XXX, 2024.
Chapter 8 summarizes the dissertation research works, concludes the results presented with some insights into further work recommendations.

Chapter 2

ATMOSPHERIC COMPOSITION

The atmosphere stems from two Greek root words, namely the "atmos" which means "steam or vapor" and the "spharia" which means "sphere or globe". It is layers of gasses and suspended liquid-solids extending from the Earth's surface up many thousands of miles, becoming increasingly thinner with distance but always held by the gravitational pull of the Earth (Engledew, 2018; Fowler et al., 2009). The atmosphere is composed of a plethora of different gases in different amounts and of particles suspended in these gases called aerosol particles. Atmospheric composition may vary considerably depending on the area of the globe and the proximity to sources, which may be both natural and anthropogenic (Samson, 2018; Pöschl, 2005; Popescu and Ionel, 2010).

Both atmospheric gases and aerosol particles may be directly emitted into the atmosphere from different sources, either as primary ones or from atmospheric processes as secondary ones. Particularly, the primary aerosol particles may consist of mineral dust, sea salt, carbonaceous aerosol, or be of biogenic origin (Myhre et al., 2013; Draxler and Rolph, 2003). Depending on their size and chemical composition, atmospheric aerosol particles may act as cloud condensation nuclei CCN or as ice nuclei IN, affecting climate and weather, penetrate the human respiratory track, affecting health, or deposit on the Earth and ocean, affecting radiation budgets and ecosystems. Parts of the atmospheric aerosol particles are characterized as the primary biological aerosol particles PBAPs, which are the airborne particles of biological origin, including viable or nonviable microorganisms

and reproductive or other cellular forms, shed or produced by bacteria, archaea, fungi, plants, lichens, etc. The PBAPs play a key role in genetic exchange between remote habitats and can cause adverse health effects and spread diseases not only to humans but also to flora and fauna (Fan et al., 2010; Tomasi and Lupi, 2017; Romero-Guzmán et al., 2021). In this context, this chapter deals with atmospheric aerosol particles, source-sinks of aerosol particles, classification of aerosol particles, types of aerosol particles, effects of aerosol particles, and interactions of aerosol particles.

2.1 Atmospheric Aerosol Particles

The research work on atmospheric aerosol particles has recently become one of the most favorite topics in the field of atmospheric sciences. The term aerosols, interchangeably named with the phrase atmospheric aerosol particles, refers to any dispersed system of liquid-solid particles suspended in the atmosphere. Atmospheric aerosol particles consist of small particles of solids like dust materials and liquids like the water vapor. They differ

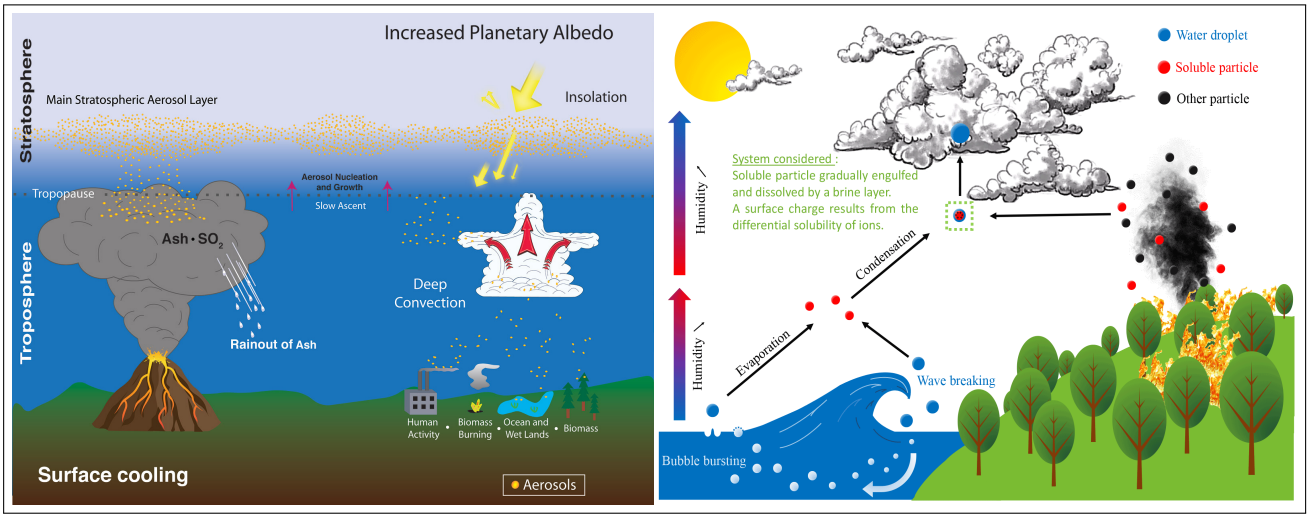

Figure 2.1: Atmospheric Aerosol Particles.

in their sources, sizes, shapes, compositions, optical properties and lifetimes depending on their origins and on the subsequent atmospheric processings (Grythe, 2017; Kafle

and Coulter, 2013). Figure 2.1 shows the schematic components for atmospheric aerosol particles, while Figure 2.2 is to describe their sizes and life times.

The amount of aerosol particles in the atmosphere, sometimes called aerosol loading, can be quantified either by mass concentration or an optical measure known as aerosol optical depth AOD. The AOD is a dimensionless quantity, the integral of the product of particle number concentration and particle extinction cross-section. It accounts for the individual

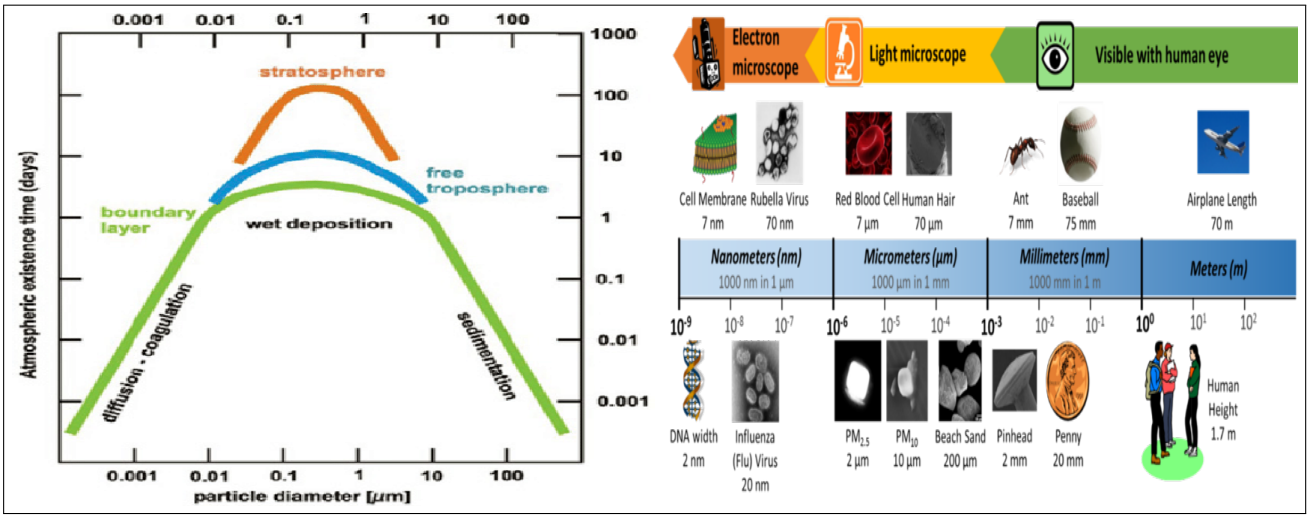

Figure 2.2: Aerosol Particles Size and Life Time.

aerosol particles scattering plus absorption along a path length through the atmosphere, usually measured vertically. The other aerosol particles optical properties parameter, Ångström exponent AE, which is related to the size distribution of aerosol particles, can be calculated from the AOD (Adesina, 2015; Falah et al., 2022b).

2.2 Source-sinks of Aerosol Particles

Primarily, atmospheric aerosol particles are released from the Earth into the atmosphere. These sources include biomass burning, incomplete combustion of fossil fuels, volcanic eruptions, wind-driven and traffic-related suspension of roads, soil and mineral dust, sea salts, sand and biological materials. In addition, some aerosol particles are also formed

through the various physical and chemical processes in the atmosphere as secondary sources. Figure 2.3 depict the main processes for source-sinks of atmospheric aerosol particles. A key precursor gas is the sulfuric acid H_2SO_4, which is produced within the atmosphere by oxidation of the sulfur dioxide SO_2 emitted from fossil fuel combustion, volcanoes and other sources (Behera, 2016; Li et al., 2015b; Huang et al., 2020).

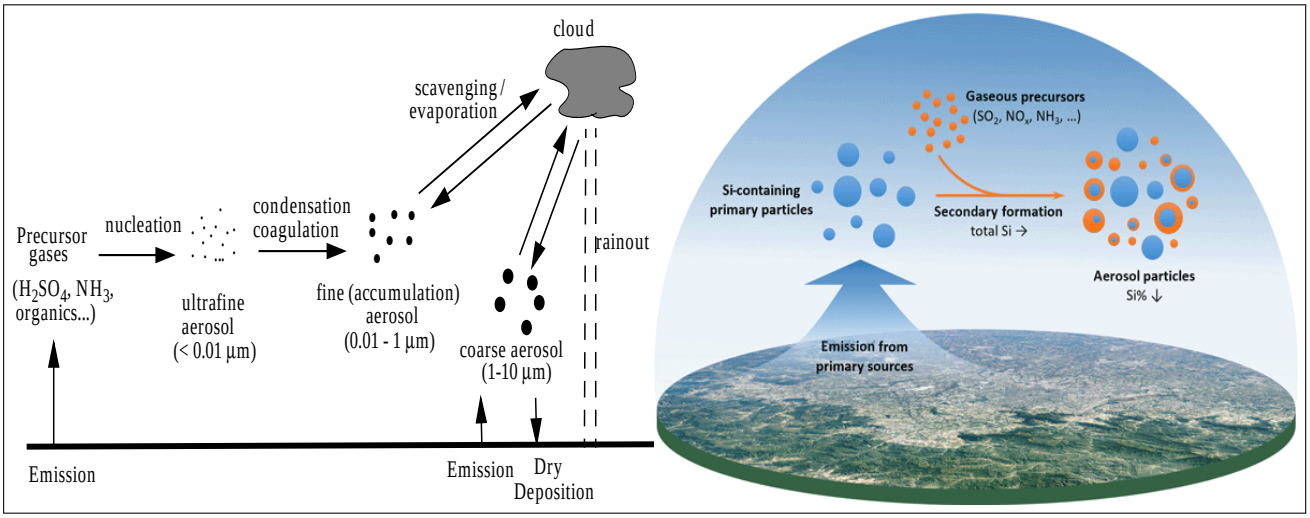

Figure 2.3: Source-sinks of Aerosol Particles.

The SO_2 is oxidized to H_2SO_4 and the rate of conversion is influenced by the presence of heavy metal ions, e.g., Fe and Mn. Some of the proposed chemical reactions can be shown using (Kokhanovsky, 2008; Chen et al., 2019):

$$SO_3 + H_2O \rightarrow H_2SO_4;$$

$$NO + O_2 + H \rightarrow HNO_3;$$

$$SO_2 + C_2H_2 + \text{allene} \rightarrow C_3H_4S_2O_3;$$

$$NO_2 + \text{hydrocarbons} + \text{photochemistry} \rightarrow \text{organic nitrates};$$

$$SO_2 + \text{alkanes} \rightarrow \text{sulfinilic acid};$$

$$O_3 + \text{olefins} \rightarrow \text{organic particles}.$$

The H_2SO_4 has a low vapor pressure over H_2SO_4-H_2O solutions and condenses under all atmospheric conditions to form aqueous sulfate particles. The composition of these sulfate particles can then be modified by the condensation of other gases with low vapor

pressure, including NH_3, HNO_3 and organic compounds. Organic carbon represents a major fraction of the fine aerosol and is contributed mainly by the condensation of large hydrocarbons of biogenic and anthropogenic origin. Another important component of the fine aerosol is soot, produced by the condensation of gases during combustion. Soot, as commonly defined, includes both elemental carbon and black organic aggregates. Particles coarser than 10 µm are not easily lifted by the wind and have short atmospheric lifetimes because of their large sedimentation velocities (Hartz et al., 2007; Kokhanovsky, 2008). Once formed, atmospheric aerosol particles do not remain suspended in the air indefinitely; they can be destroyed, altered or removed. Their residence time is affected by their size, location and atmospheric conditions. The sinks for the aerosol particles occur in wet and dry depositions. When aerosol deposition involves water it is termed 'wet deposition' and it takes several forms: sweepout, rainout, washout and occult deposition. And when aerosols fall under gravity, they are said to undergo 'dry deposition'. The fall is determined by the diffusion coefficient and the fall velocity. The fall rate is proportional to the size and inversely proportional to the density of the atmosphere.

2.3 Classification of Aerosol Particles

The aerosol particles sometimes called particulate matter PM, by synonymous terms also called Suspended Particulate Matter SPM and Total Suspended Particulate TSP or Total Suspended Particulate Matter TSPM. In broadly category for aerosol sources, atmospheric aerosol particles originate from both natural and anthropogenic activities. Natural aerosol particles originate from natural occurrences such as dust storms, sea spray, volcanoes and forest and grassland fires, while anthropogenic aerosols come from man-made activities such as industrial emissions, vehicular emissions and burnings from biomass and fossil fuels. Figure 2.4 and Table 2.1 illustrate the classification of atmospheric aerosol particles by their major sources.

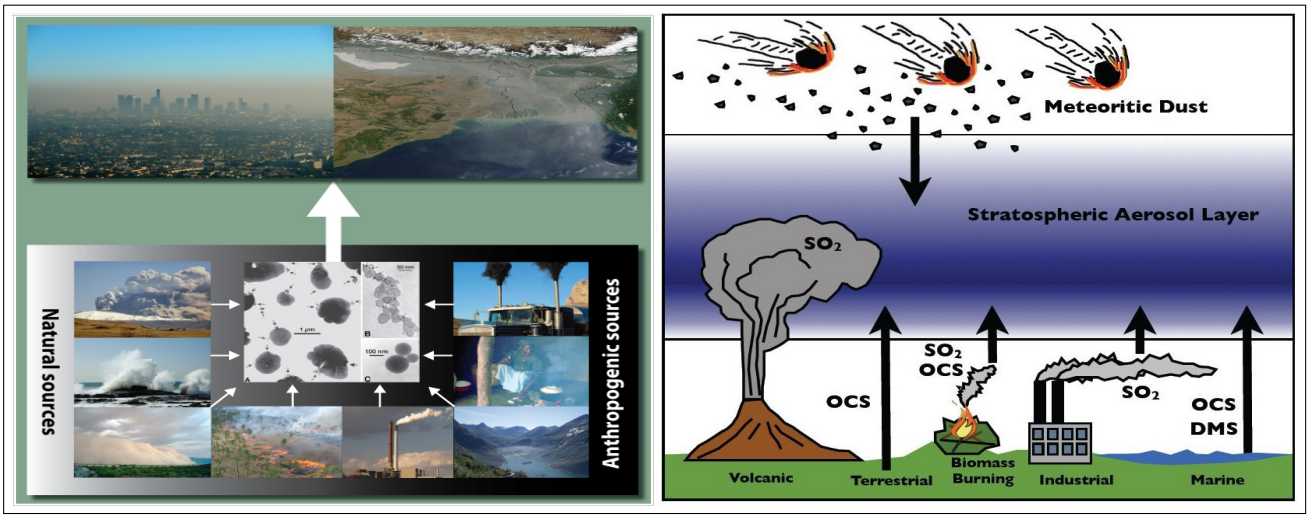

Figure 2.4: Classification of Aerosol Particles.

Marine Aerosol Particles: are either formed mechanically by the sea waves or by the gas-to-particle conversion process of precursor gases in the marine atmosphere. These oceanic-origin aerosols are estimated to form 30% of total aerosol loading. Those that are formed by mechanical processes are termed sea-salt aerosol particles, while those formed by gas-to-particles are non-sea-salt aerosols, e.g., dimethyl sulphide (Hoppel, 1979; Prospero et al., 1983; Charlson et al., 1987).

Mineral Aerosol Particles: are very common in desert areas where there exist either a low or sparse vegetative cover. Surface winds over these areas often inject the dry soils into the atmosphere and at other times they can result from human activities such as construction, agriculture, transportation and deforestation. Their lifetime is affected by their size. In dealing with these types of aerosols, their radiative effect can only be quantified when their microphysical properties are known (Tegen and Fung, 1994).

Volcanic Aerosol Particles: formed through the condensation of volcanic ash and the fragmentation of magma or lava during a volcanic eruption as dust and gaseous sulphur. The sulphur thus produced is more efficient in producing the sulphate aerosol particles about 4.5 times more than those of anthropogenic origin, because they have a lower deposition rate (Balsamo et al., 2018; Graf et al., 1997).

Sulphates: are produced from activities such as oil refining and smelting, coal and oil combustion and though they are mainly submicron particles, they are capable of being conveyed from their sources over long distances. SO_2 can be quantified as 72% from fossil fuel burning, about 2% from biomass burning, about 19% from dimethyl sulphide emission by phytoplankton and about 7% from volcanoes. They can indirectly influence the optical properties of clouds by forming cloud condensation nuclei because they are hydrophilic. Sulphate aerosol has a direct radiative forcing RF of about -0.4±0.2 Wm^{-2} (Takemura et al., 2000; Haywood and Boucher, 2000).

Nitrates: are formed by the oxides of Nitrogen like NO_2, N_2O, N_2O_4 and the volatile acids of nitrogen which originates from biomass burning, fertilizers, bacterial actions on soil and vehicular exhaust. The most predominant type is the ammonium nitrate. Nitrate aerosol has direct RF of about -0.10±0.10 Wm^{-2} although this is subject to further investigations (Hidy, 2012; Pruppacher et al., 1978).

Soot Aerosol Particles: are arisen from complex mixture of organic carbon OC and elemental carbon EC. OC and black carbon BC come from incomplete combustion of carbonaceous materials. They are the most important sunlight-absorbing aerosol particles in the atmosphere serve as catalysts in some chemical reactions within the atmosphere. They are the most significant for their absorption properties and their inhibition of cloud formation. BC has direct radiative forcing of -0.20±0.15 Wm^{-2} has semi-direct effect is non-inclusive, while OC has direct radiative forcing of -0.05 ±0.05 Wm^{-2} (Gundel et al., 1989; Tanré et al., 1997; Shekar and Venkataraman, 1999; Ackerman et al., 2000).

2.4 Types of Aerosol Particles

Aerosol particles are generally classified into three sizes: Ultra-Fine-Nucleation-Aitken mode aerosol particles in the radius range 0.001 – 0.1 µm, Accumulation mode have radius of 0.1 – 1.0 µm and Coarse mode > 1.0 µm in radius. And also, due to the fact

Table 2.1: Properties of the main aerosol species in the troposphere (Adesina, 2015).

Aerosol Species	Size Distribution	Main Sources	Main Sinks	Tropospheric Lifetime	Key Climate Relevant Properties
Sulphate	Primary: Aitken, accumulation and coarse modes Secondary: Nucleation, Aitken, and accumulation modes	Primary: marine and volcanic emissions. Secondary: oxidation of SO2 and other S gases from natural and anthropogenic sources	Wet deposition Dry deposition	~ 1 week	Light scattering. Very hygroscopic. Enhances absorption when deposited as a coating on black carbon. Cloud condensation nuclei (CCN) active.
Nitrate	Accumulation and coarse modes	Oxidation of NOx	Wet deposition Dry deposition	~ 1 week	Light scattering. Hygroscopic. CCN active.
Black carbon	Freshly emitted: <100 nm Aged: accumulation mode	Combustion of fossil fuels, biofuels and biomass	Wet deposition Dry deposition	1 week to 10 days	Large mass absorption efficiency in the shortwave. CCN active when coated. May be ice nuclei (IN) active.
Organic aerosol	POA: Aitken and accumulation modes. SOA: nucleation, Aitken and mostly accumulation modes. Aged OA: accumulation mode	Combustion of fossil fuel, biofuel and biomass. Continental and marine ecosystems. Some anthropogenic and biogenic non-combustion sources	Wet deposition Dry deposition	~ 1 week	Light scattering. Enhances absorption when deposited as a coating on black carbon. CCN active (depending on aging time and size).
... of which brown carbon	Freshly emitted: 100–400 nm Aged: accumulation mode	Combustion of biofuels and biomass. Natural humic-like substances from the biosphere	Wet deposition Dry deposition	~ 1 week	Medium mass absorption efficiency in the UV and visible. Light scattering.
... of which terrestrial PBAP	Mostly coarse mode	Terrestrial ecosystems	Sedimentation Wet deposition Dry deposition	1 day to 1 week depending on size	May be IN active. May form giant CCN
Mineral dust	Coarse and super-coarse modes, with a small accumulation mode	Wind erosion, soil resuspension. Some agricultural practices and industrial activities (cement)	Sedimentation Dry deposition Wet deposition	1 day to 1 week depending on size	IN active. Light scattering and absorption. Greenhouse effect.
Sea spray	Coarse and accumulation modes	Breaking of air bubbles induced e.g., by wave breaking. Wind erosion.	Sedimentation Wet deposition Dry deposition	1 day to 1 week depending on size	Light scattering. Very hygroscopic. CCN active. Can include primary organic compounds in smaller size range
... of which marine POA	Preferentially Aitken and accumulation modes	Emitted with sea spray in biologically active oceanic regions	Sedimentation Wet deposition Dry deposition	~ 1 week	CCN active.

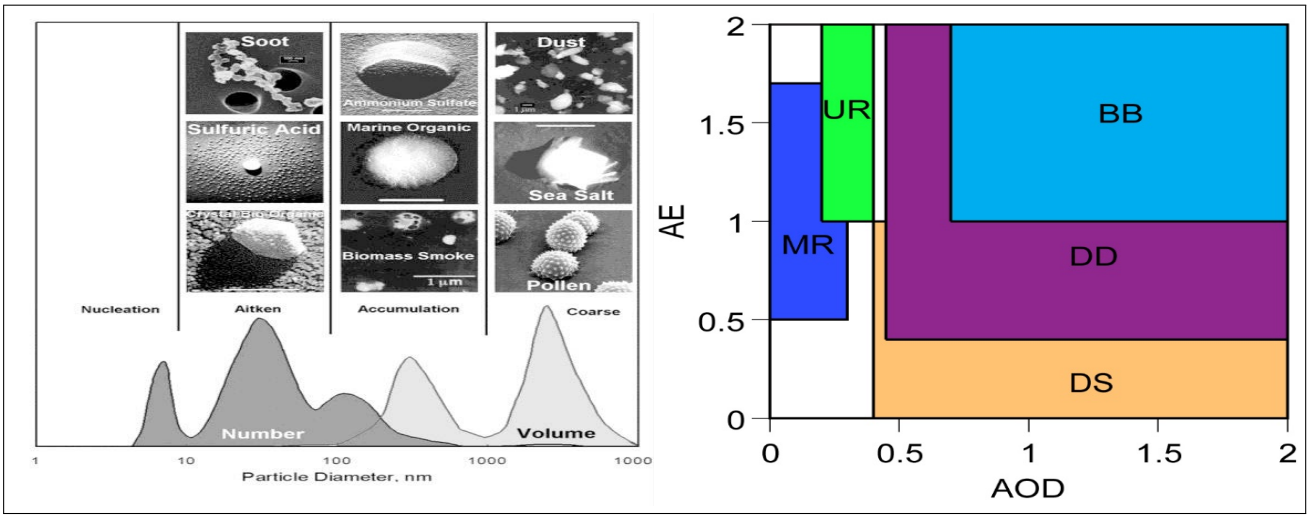

Figure 2.5: Types of Aerosol Particles.

that aerosol particles are formed by different processes and are subject to both vertical and horizontal circulation in the atmosphere, they are mixed together at the micro-scale and through large-scale diffusion and coagulation. Figure 2.5 depicts the classification of aerosol particles by their sizes. Aerosol particles types largely depend on sources and the nature of production.

Soil-Derived Aerosol Particles: are formed by the weathering of soil and ejected into the atmosphere as ultra-fine particles by wind, especially in the arid regions of the world. They form a significant constituent of aerosol particles even in locations far away from their sources due to their transportation by convection currents and general circulation systems. They exist in the coarse mode, especially in the source region. As they are transported to distant regions, their radius becomes smaller in the range of $0.1 < r < 5$ µm. They exist mainly in the troposphere, having high variability in the imaginary part of the refractive index, which determines their climate forcing. The reported range of direct RF goes from -0.56 to + 0.1 Wm^{-2}.

Sea-Salt Aerosol Particles: their production is normally associated with the bursting of whitecap bubbles. After production, they rise by evaporation until they attain equilibrium with the ambient relative humidity. They remain either as crystalline matter or as a

solution droplet. Their radius is generally less than 0.1 µm and contributes the highest percentage to the global aerosol population (Blanchard and Woodcock, 1980).

Polar Aerosol Particles: the number concentration of this type of aerosol particles are influenced significantly by Arctic haze. Apart from the fact that they are aged, they contain carbonaceous material from sea salt, mineral dust and mid-latitude pollen sources.

Rural Aerosol Particles: in rural areas, aerosol particles are less from anthropogenic sources but more of natural origin. They are characterized by two modes of number distribution with diameters of about 0.02 and 0.08 µm, while the mass distribution of the coarse mode is centered about 7 µm (Hobbs et al., 1985; Jaenicke, 1993).

Urban Aerosol Particles: in the urban areas, aerosols are multi-modal in nature, consisting of nucleation, accumulation and coarse modes. The mechanically generated coarse mode is more dust and sea salt, whereas the accumulation mode is primarily from combustion sources and the nucleation mode is a gas-to-particle conversion resulting from chemical reactions of nitrates, sulphates and ammonium. The accumulation mode tends to have a higher concentration than the other modes.

Remote Aerosol Particles: this type of aerosol particles can be characterized by three modes of number distribution with diameters of 0.02, 0.1 and 2 µm are made up of pollens, dust and waxes (Koutsenogii and Jaenicke, 1994; Jaenicke, 1993).

Extra-Terrestrial Aerosol Particles: these types of aerosols are commonly found in the stratosphere, with a size ranging from tenths of a micron to several millimeters in diameter. They are formed from meteor showers and comet debris and are responsible for zodiacal light.

2.5 Effects of Aerosol Particles

Atmospheric aerosol particles have large impacts on the climate and human health. The aerosol particles have multidimensional effects, including visibility reduction, respiratory

disease, interference with photosynthesis and climate effects. The effects are both health and non-health-related and can be briefly summarized as follows:

Health effects

Effect of the aerosol particles on health issues are determined by three factors; toxicity concentration, susceptibility of individuals and duration of exposure. Aerosols can cause: cardio-vascular diseases, carcinogenic effects, respiratory hazards, morphological changes, increase the mortality and morbidity. The effects are more pronounced in people with

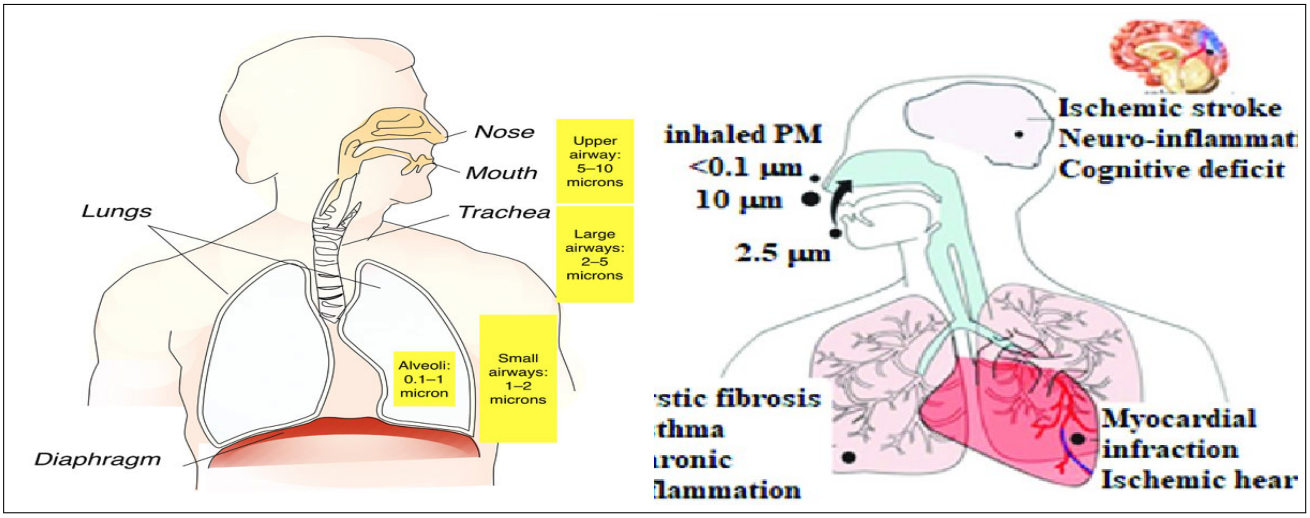

Figure 2.6: Aerosol Particles Health Effect.

asthma, cardiovascular problems and general respiratory problems. Figures 2.6 and 2.7 are used to illustrate the aerosol particles climatic and health effects.

Non-Health Effects

There is clear and rapidly growing evidence that the atmospheric aerosol particles have profound impacts on the thermodynamics and radiative energy budgets of the Earth. The aerosol particles affect the atmosphere: directly by altering the properties of the radiation energy budget through scattering and absorbing the solar radiation; indirectly by affecting the cloud microphysical properties; and semi-directly through the absorbed radiation energy by aerosol particles, which is able to increase the temperature of the surrounding air, resulting in the evaporation of cloud droplets and ice particles. The

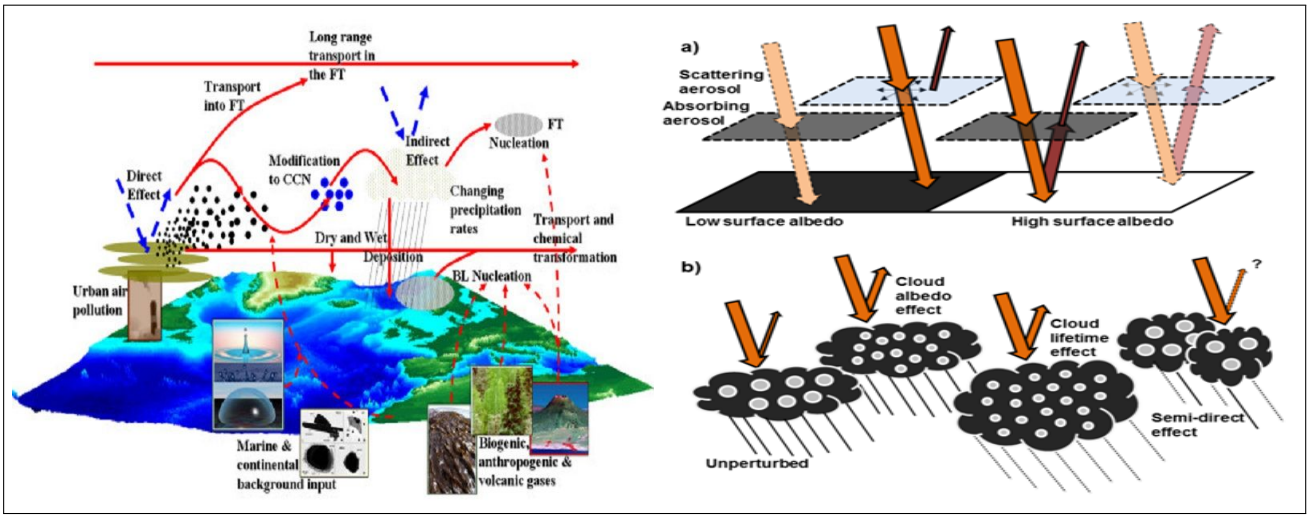

Figure 2.7: Aerosol Particles Atmospheric Effect.

aerosol particles have an impact on regional and global climates; these effects have been attracting attention among all nations. It causes visibility impairment and damage to vegetation. The long-term effects of industrial pollutants such as lead, arsenic and fluorine lead to low fertility, reduced milk production and also block the stomata in plants.

2.6 Interactions of Aerosol Particles

The formation and life cycle of clouds are altered by anthropogenic aerosol as shown by a wide range of measurements (Quaas, 2015). Figure 2.8 is to depict the interactions of aerosol particles on the various atmospheric components. To be able to correctly interpret and understand climate change there is a need to understand and quantify the microphysical impact of aerosols on clouds. This can only be effectively done through focusing on their microphysical relationship and their response to large-scale weather systems (Kim et al., 2003; Khedidji et al., 2020; Myhre et al., 2007a; Charlson et al., 2007). The impact of aerosol particles on clouds can be summarized into:

Effect on Water Cloud Droplets: when there is an increase in cloud condensation nuclei as a result of aerosol loading, the number of water cloud droplets is enhanced, though with reduced sizes. This will result in an increase in cloud optical thickness and

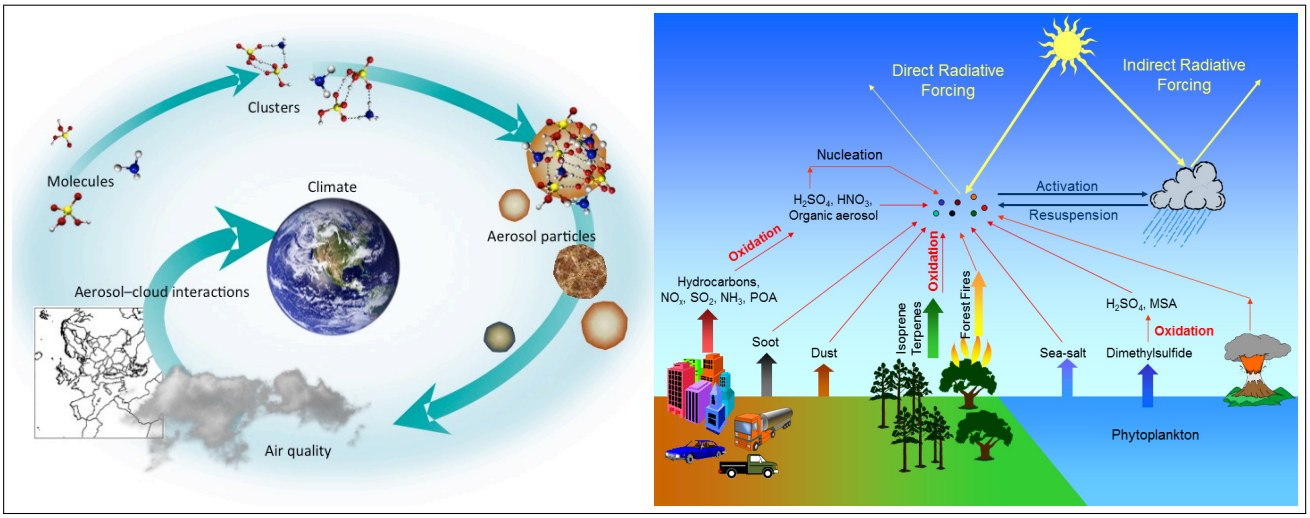

Figure 2.8: Aerosol Particles Interaction.

solar insolation reflectivity. When the cloud droplet size is reduced, precipitation can be inhibited, which in turn can increase cloud lifetime so that clouds evolve to greater height, thereby resulting in an increase in the cloud optical thickness. Here, increased aerosol particles leading to an increase in CCN are known to increase cloud droplet concentration and cloud albedo, decreasing cloud droplet size if the water content in the cloud remains unchanged (Twomey, 1977; Khain et al., 2005; Williams et al., 2002).

Effect on Cloud Cover: aerosol particles cause the evaporation of existing clouds and the blocking of surface heating. These have a very strong impact on the radiative balance. Studies on ice clouds show that the number of ice nuclei is potentially influenced by anthropogenic aerosols. When precipitation is suppressed, the aerosol particles are capable of changing the structure of the clouds so that open Bernard cells can be closed, thus increasing the cloud cover (Johnson et al., 2004; Penner et al., 2003; Rosenfeld et al., 2006). As efforts are being geared towards reducing the uncertainty of the contribution of anthropogenic aerosol particles to climate change, scientists see the need to obtain and analyze data from coordinated multiple platforms involving *in-situ* measurements, numerical modeling, remote sensing from ground-based, satellite, aircraft and ship etc (Anderson et al., 2005; Diner et al., 2004; Kaufman et al., 2002).

Radiative Effects: aerosol particles scatter radiation beams in their paths when their direction of propagation is altered without absorption taking place. Scattering may take place by reflection, refraction or diffraction of the radiation beam. Scattering is the maximum for a particle radius corresponding to the wavelength of radiation. Larger particles also scatter radiation efficiently, while smaller particles are inefficient scatterers. Atmospheric aerosols in the accumulation mode are efficient scatterers of solar radiation because their size is of the same order as the wavelength of radiation; in contrast, gases are not efficient scatterers because they are too small. Some aerosol particles, such as soot, also absorb radiation (Piyush and S, 2016; Satheesh and Moorthy, 2005).

The scattering of solar radiation by the aerosol particles is the main process limiting the visibility in the troposphere. The anthropogenic aerosol particles in urban environments typically reduce visibility by one order of magnitude relative to the unpolluted conditions. The visibility reduction is greatest at high relative humidities when the aerosol particles swell by uptake of water, increasing the cross-sectional area for scattering; this is the phenomenon known as the haze (Piyush and S, 2016; Quaas, 2015).

Scattering of solar radiation by aerosol particles increases the Earth's albedo because a fraction of the scattered light is reflected back to space. The resulting cooling of the Earth's surface is manifest following large volcanic eruptions, which inject large amounts of aerosol particles into the stratosphere. Remarkably, the optical depth of the stratospheric aerosol following a large volcanic eruption is comparable to the optical depth of the anthropogenic aerosol in the troposphere. The natural experiment offered by erupting volcanoes thus strongly implies that anthropogenic aerosols exert a significant cooling effect on the Earth's climate. Because of their short lifetime, aerosol concentrations are highly variable from region to region, which makes determining their radiative effect extremely difficult (Satheesh and Moorthy, 2005; Quaas, 2015).

2.7 The Optical Parameters from Satellite Data

This section deals with the parameters of the aerosol optical depth AOD, Ångström exponent AE or AET, atmospheric water vapor AWV, mean cloud fraction CFM, cloud top pressure CTP and cloud top temperature CTT that were retrieved from the MODIS satellite data; the precipitation PPT that was retrieved from the TRMM satellite data and the outgoing long-wave radiation OLR flux that was retrieved using the CERES satellites. In addition, atmospheric aerosol particles radiative forcing parameters are discussed.

Aerosol Optical Depth AOD: is the measure of the extinction of the solar beam by dust and haze. In other words, particles in the atmosphere can block sunlight by absorbing or scattering light. The AOD tells us how much direct sunlight is prevented from reaching the ground by these aerosol particles. It is a dimensionless number that is related to the amount of aerosol in the vertical column of the atmosphere over the observation location. A value of 0.01 corresponds to an extremely clean atmosphere, and a value of 0.4 would correspond to a very hazy condition. As an example, the average aerosol optical depth in the US is 0.1 to 0.15 (Augustine et al., 2008; Gehlot et al., 2015).

Ångström Exponent AE-AET: describes the spectral dependence of light absorption by aerosols. The AE is an important aerosol particles optical parameter that is used for aerosol characterization and apportionment studies. It is a parameter that describes how the optical thickness of an aerosol particles typically depends on the wavelength of the light. For example, the Ångström exponent of black carbon BC particles is widely accepted to be 1.0, although observational estimates give quite a wide range of 0.6–1.3. The AE with the AOD is typically used to differentiate between the different types of atmospheric aerosol particles classifications (Liu et al., 2018; Benkovitz et al., 1994).

Atmospheric Water Vapor AWV: is the gaseous phase of water. Over 99% of the atmospheric moisture is in the form of water vapor, and this vapor is the principal source of the atmospheric energy that drives the development of weather systems on short time

scales and influences the climate on longer time scales. Water vapor is a critical component of Earth's climate systems. It is the Earth's primary greenhouse gas, trapping more heat than carbon dioxide. The movement of water vapor and its associated latent heat of vaporization is also responsible for about 50% of the transport of heat from the tropics to the poles. The movement of water vapor is also important for determining the amount of precipitation a region receives (Buis, 2022; Held and Soden, 2000).

Total column water vapor is a measure of the total gaseous water contained in a vertical column of the atmosphere. It is quite different from the more familiar relative humidity, which is the amount of water vapor in the air relative to the amount of water vapor the air is capable of holding. Atmospheric water vapor is the absolute amount of water dissolved in the air. When measured in linear units mm, it is the height or depth the water would occupy if the vapor were condensed into liquid and spread evenly across the column. Using the density of water, we can also report the water vapor in $kgm^{-2} = 1$ mm or $gcm^{-2} = 10$ mm (Després et al., 2012).

Mean Cloud Fraction CFM: the cloud fraction is the percentage of each pixel in satellite imagery or each grid-box in a weather or climate model that is covered with clouds. A cloud fraction of one means the pixel is completely covered with clouds, while a cloud fraction of zero represents a totally cloud-free pixel. In the assessment of the climate effect of clouds, mean cloud fraction is one of the most crucial climatological variables. Measurements of this cloud parameter have been widely used to evaluate and parameterize global climate models. A joint distribution of the parameters serves better in constraining parametrization schemes in climate models (Yang and Di Girolamo, 2008).

Cloud Top Pressure CTP: cloud pressure is the weight of the cloud per unit area. The cloud top, or top of the cloud, is the highest altitude of the visible portion of the cloud. It is traditionally expressed either in meters above the Earth or on the planetary surface, with the corresponding pressure level in hectopascal hPa, equivalent to the traditional but now obsolete millibar. Cloud top pressure is determined from cloud top temperature,

which the satellite measures more directly using a profile of atmospheric temperature with pressure. It can be considered equivalent to the cloud-top height above the mean sea level. The cloud top pressure product contains an image with pixel values identifying the atmospheric pressure at the top of a cloud layer. The product is generated in combination with the cloud top height and cloud top temperature products by the same algorithm. The product includes data quality information that provides an assessment of the cloud top height data values for on-earth pixels. When the retrieval has failed due to missing or incorrect input data, the pixels will have an unknown value (Marchand et al., 2010).

Cloud Top Temperature CTT: is the atmospheric temperature observed at the top of a cloud. The baseline cloud top height temperature estimates the temperature of the cloud top in degrees Celsius; it is generally more accurate than individual channel brightness temperatures that can be affected by absorption by gases. This parameter can be used to monitor cloud-top temperature changes during convection and also temperature thresholds for events (Wielicki et al., 1995).

The Precipitation PPT: is all types of moisture reaching the surface of the Earth from the atmosphere. The moisture entering the atmosphere as a result of evaporation from water and land surfaces is transported with air fluxes; it condenses and again falls as precipitation on the surface of the Earth. Precipitation is the water in a liquid or solid state falling from clouds or formed on the Earth's surface and ground objects due to the condensation of airborne water vapor. Depending on the mechanism of cloud development and structure, precipitation may be continuous, temperate-intense, produced predominantly from stratocumulus clouds, heavy from cumulonimbus clouds, or drizzle, often from stratus clouds (Trenberth, 1998).

Outgoing Long-Wave Radiation OLR: measures the amount of terrestrial radiation that released into space and, by extension, the amount of cloud cover and water vapor that intercept that radiation in the atmosphere. Input data for the OLR record primarily comes from high-resolution infrared radiation sounder HIRS radiance observations since

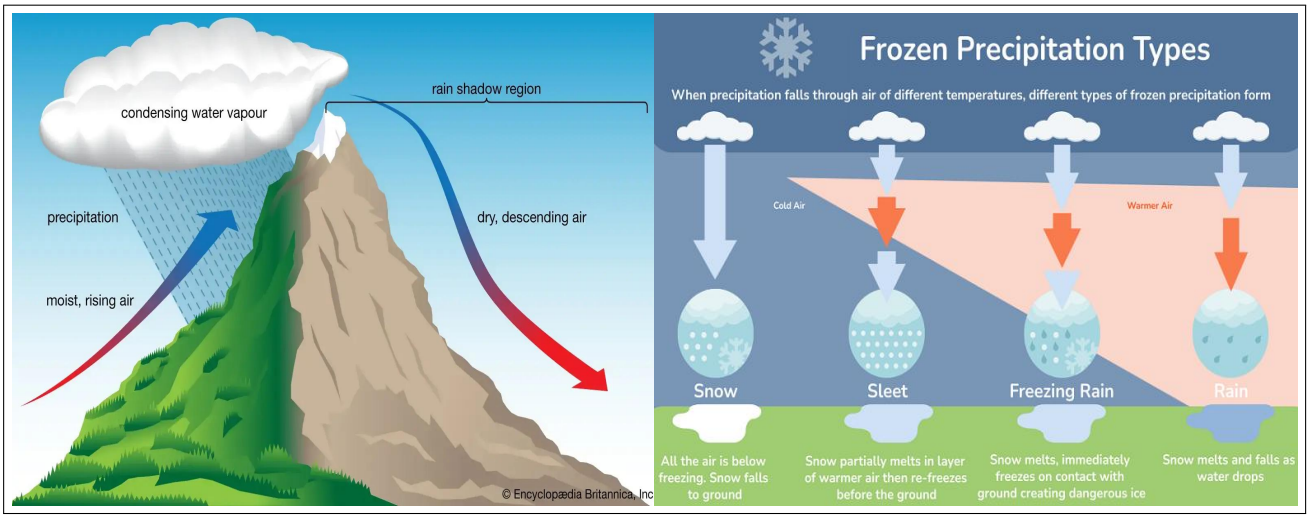

Figure 2.9: The Precipitation and Its Types.

1979 and new generation infrared hyperspectral sounder radiance data, including from the Infrared Atmospheric Sounding Interferometer IASI since 2007 and the Cross-track Infrared Sounder CrIS since 2012. The OLR is also retrieved from a combination of operational geostationary imagers, which helps to achieve better accuracy for the OLR integral. The final record is generated through a combination of statistical techniques, including OLR regression, instrument ambient temperature prediction coefficients, and inter-satellite bias corrections. The record technique for outgoing long-wave radiation flux spans from 1979 - present (Lee et al., 2007).

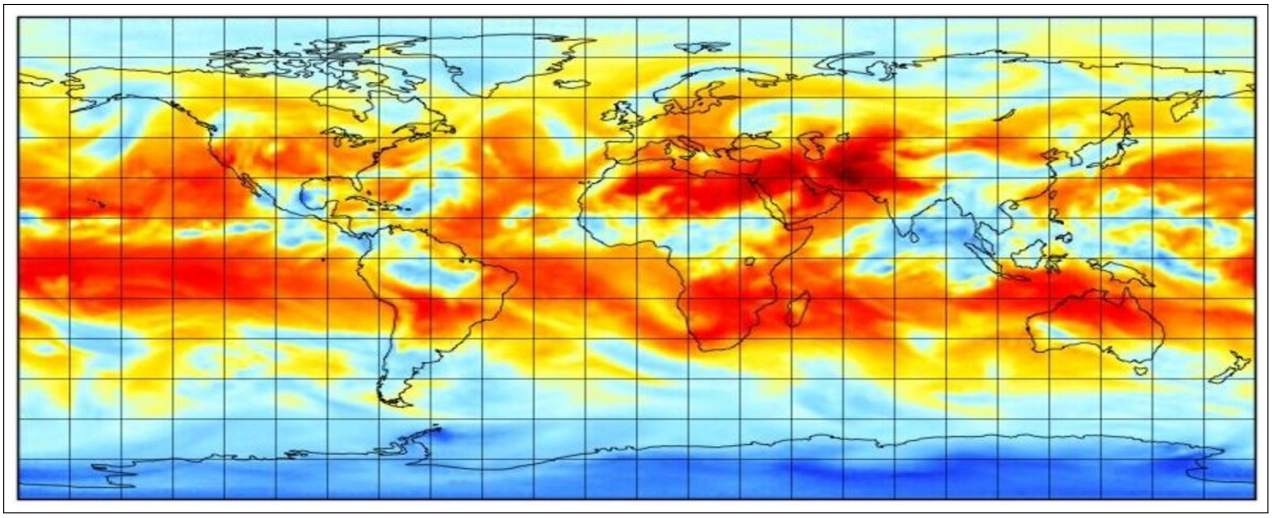

Figure 2.10: The Outgoing Long-Wave Radiation.

Aerosol Particles Radiative Forcing: atmospheric aerosol particles directly affect the radiation budget by back-scattering or absorbing sunlight, as well as semi-directly or indirectly by altering the atmosphere and cloud properties. The effective radiative forcing by aerosol-radiation interactions ARI includes both the instantaneous effect and the so-called rapid adjustment of the atmosphere to aerosol effects due to changes in local heating rates caused by aerosol absorption, which can affect atmospheric stability or cloud cover. Furthermore, aerosols have a micro-physical influence on the formation of cloud droplets and ice crystals and also contribute to effective radiative forcing in this indirect way via aerosol-cloud interactions ACI. Atmospheric aerosols reduce downward solar radiation at the surface, which is called surface dimming. On the land surface, this dimming by absorbent aerosols can lead to a significant reduction in the upwelling latent and sensible heat fluxes at the surface (Li et al., 2016).

Ethiopia is part of East Africa: it is neighbor to both the continental and maritime daughter countries Kenya, Sudan, Eritrea, Somalia, and Djibouti, which are exposed to forest, volcanic, and oceanic dusts (Lee et al., 2010; Apollo and Mbah, 2021). And also, Ethiopia is experiencing infrastructural development such as increasing urbanisation accompanied by a development boom such as building and road construction, industrial expansion, traffic density, both active and inactive volcanoes, etc., which increase air pollution in various ways (Wassie, 2020; Homa et al., 2017). Because of these facts and activities, the atmosphere is loaded with solid matter, mainly dust and minerals (Myhre et al., 2013; Barnsley, 1999; Ferronato and Torretta, 2019; Gheorghe and Ion, 2011).

Generally, the East African-Ethiopian climate has been categorized into the four major seasons: during December–February, called the winter in Amharic Bega season; during March–May, the spring in Amharic Tseday season; during June–August the summer in Amharic Kiremt season; and during September–November the autumn in Amharic Belg season (Makokha et al., 2017a; Aga, 2023; Ayanlade et al., 2019; Kalisa et al., 2023).

Chapter 3

INSTRUMENTATION

The optical properties of atmospheric aerosol particles, their effects on health-climate related changes and radiative forcing became an important field of studies few years before the close of the last century (Charlson et al., 1992; Twomey et al., 1984). The major challenge faced since that time has been the difficulty in estimating and predicting the changes that occur in climate due to the uncertainty in the contribution of aerosol particles and their radiative forcing. The transient and heterogeneous nature of aerosol particles make their contribution difficult to quantify (Christopher et al., 1996; Tegen et al., 1996). This gave rise to remote sensing instruments that are capable of measuring with precision a radiative forcing of the order of 1 Wm^{-2} when the optical depth changes in excess of 0.1. In particular, ground-based and satellite-based remote sensing have become increasingly useful tools for carrying out such measurements. While the ground-based system has the advantage of being simple, reliable and being supportive in the validation of satellite retrievals, it does not have the long-term data acquisition capability of reliable measurement and efficient processing of data, thereby leading to disjointed data sets that cannot be used for scientific assessments (Salau et al., 2009). This chapter is to present the Remote Sensing Techniques RST and the satellite-based instruments that include the Moderate Resolution Imaging Spectroradiometer MODIS, Tropical Rainfall Measuring Mission TRMM and Clouds and Earth‘s Radiant Energy System CERES used for the imagery data sources in the study. Additionally, optical parameter retrieval is discussed.

3.1 The Study Areas and Sites

This study was conducted in East Africa, specifically in Ethiopia. The daughter countries Djibouti and Eritrea, formerly part of Ethiopia, and South Sudan were purposefully included in the research areas of the study. Sixteen sites, i.e., ten from Ethiopia, three from South Sudan, two from Eritrea, and one from Djibouti, were selected and then divided into four clustered regions: southwest, southeast, northwest, and northeast.

Division	Station	Longitude	Latitude
Southwest	Juba[SS]	31.58	04.86
	Agnuak	34.59	08.25
	Raga[SS]	26.04	08.55
Southeast	Awassa	38.48	07.06
	Kebri Dahar	44.26	06.74
	Addis Ababa	38.75	09.03
Northwest	Dangote	38.34	09.42
	Tonga[SS]	31.70	09.56
	Ethiopian Renascence Dam	35.09	11.23
	Bahir Dar	37.39	11.59
	Humera	36.61	14.29
Northeast	Kombolcha	39.73	11.09
	Djibouti[DJ]	43.00	11.73
	Aseb[ER]	41.98	13.88
	Erta Ale	40.66	13.06
	Dahlak[ER]	40.06	16.33

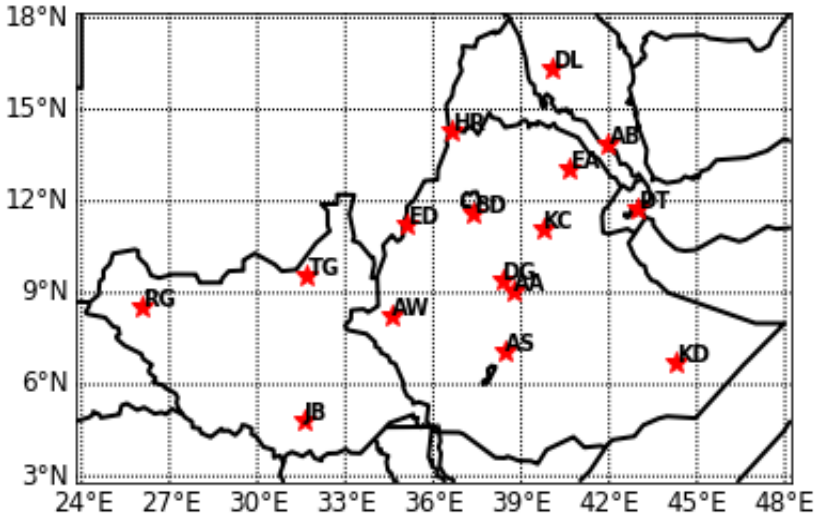

Figure 3.1: Latitudinal and longitudinal sites of the study area.

The sites are assigned with two capital letters, i.e., **MN** = Mean, **JB** = Juba, **RG** = Raga and **TG** = Tonga which are taken from South Sudan; whereas the **AW** = Agnuak, **AS** = Awassa, **HR** = Humera, **KD** = Kebri Dahar, **AA** = Addis Ababa, **DG** = Dangote, **ED** = Great Ethiopian Renascence Dam, **BD** = Bahir Dar, **KC** = Kombolcha, and **EA** = Erta Ale are sites selected from Ethiopia; **DT** = Djibouti is one of the selected sites from Djibouti; and **DL** = Dahlak and **AB** = Aseb are sites chosen from Eritrea. Figure 3.1 shows four East African countries, namely Ethiopia, Eritrea, Djibouti, and South Sudan{3–18^0 N, 24–48^0 E} which have been taken as the study areas{1,897,129 km^2} of this research, along with details of those sites in their clustered regions. In general, the study areas and selected sites consist of both continental and marine sources of aerosols.

3.2 Remote Sensing Techniques RST

Remote sensing is the art of taking measurements without any physical contact with the objects under observation. It is the science of acquiring information about the Earth using instruments that are remote to the surface of the Earth, usually from aircraft and-or satellites. Those instruments may use visible light, infrared waves and radar to obtain data. Remote sensing offers the ability to observe and collect data for large areas relatively quickly and is an important source of data. This is done by sensing and recording reflected or emitted energy and processing, analyzing and applying that information. It is basically divided into two categories: active and passive remote sensing.

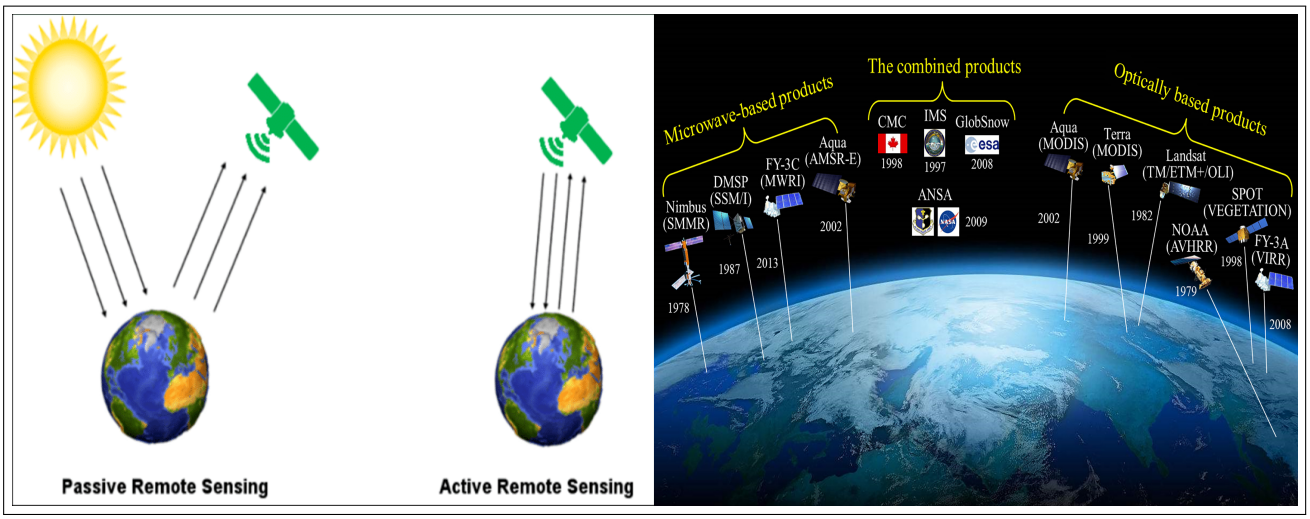

Figure 3.2: Remote Sensing Techniques.

When an instrument depends on energy reflected or emitted from the object, it is a passive instrument, but when it has its own energy source, it is active. In most cases, the external source of reflection is sun radiation (Schanda, 2012; Chuvieco, 2020). Figure 3.2 illustrates the remote sensing categories with some common instruments. Moreover, the descriptive nomenclatures of some common remote sensors that are used for the study will be discussed in the upcoming sections.

3.3 Moderate Resolution Imaging Spectroradiometer MODIS

For the majority of atmospheric science investigations, satellite-based remote sensing data with high geographical and temporal resolution is more valuable (Verma et al., 2019b). For this PhD research work, 22 years of daily-monthly imagery data were collected from the Moderate Resolution Imaging Spectroradiometer MODIS satellite web-site portal: https://ladsweb.modaps.eosdis.nasa.gov/ from January 01, 2001 to December 31, 2022. Here, the atmospheric aerosol particles optical parameters were collected from the Terra MOD04_3K and Aqua MYD04_3K daily satellite data, while the cloud cover parameters were collected from the Terra MOD08_M3 and Aqua MYD08_M3 monthly data. The following subtopics deal with the MODIS satellites.

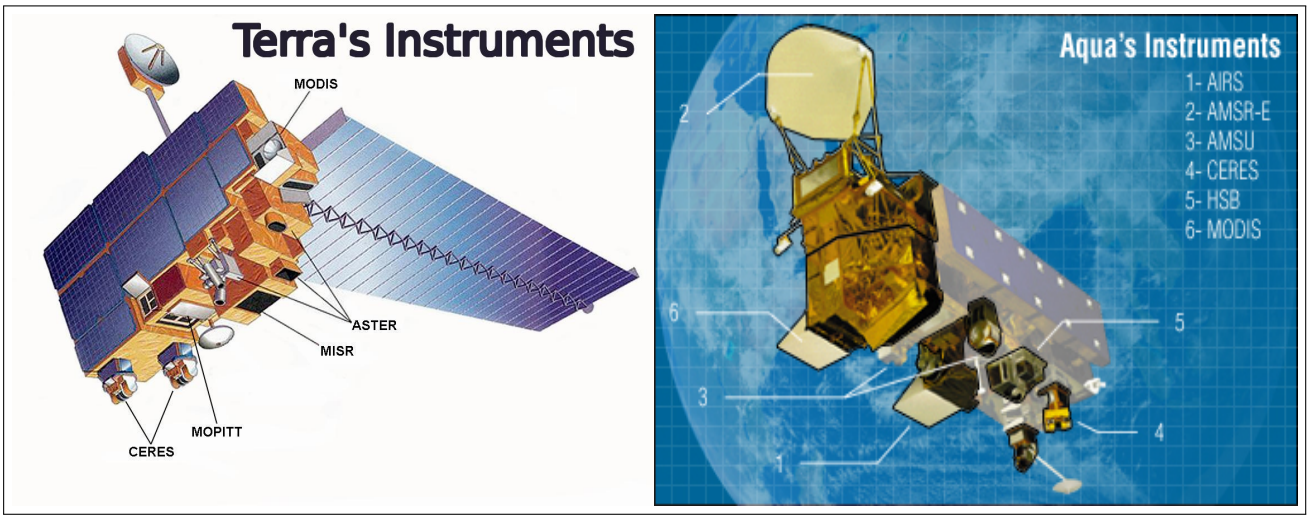

Figure 3.3: The MODIS Satellite Instruments.

MODIS Satellite: It is a key instrument that consists of Terra and Aqua satellites onboard. The Terra satellite orbits around the Earth during the morning at 10:30 local time, descending in the north-to-south direction, while Aqua orbits during the afternoon at 13:30 local time, ascending in the south-to-north direction. Both of these instruments capture the same area on Earth with 36 spectral bands. They can observe the Earth surface every 1–2 days (Verma et al., 2019a).

MODIS measures various aerosol optical properties that include AOD, identification types of aerosol particles and aerosol size distribution, which enable us to understand the complex atmospheric processes and varying climate dynamics over land and oceans. It provides long-term and continuous measurement of different aerosol properties over a very long period of time, which plays an important role in validating and developing new models to predict climate change (Verma et al., 2019b).

Out of 36 bands, the first 19 are used for land, clouds, aerosol particles, ocean color, atmospheric water vapor, biogeochemistry etc., while the remaining 17 bands are used for the surface, clouds, atmospheric profile, cloud water vapor etc (Liu et al., 2021). Table 3.1 and Figure 3.3 present the general characteristics and schematic of the MODIS satellites.

Table 3.1: General characteristics of MODIS satellite used for aerosol retrievals.

S.No	Characteristics	Terra	Aqua
1	Spatial_resolution_at_Nadir(km)	0.25 (bands 1-2) 0.50 (bands 3-7) 1.00 (bands 8-36)	0.25 (bands 1-2) 0.50 (bands 3-7) 1.00 (bands 8-36)
2	Pixel resolution (km)	Along-track 1, 3, 5 and 10	Along-track 1, 3, 5 and 10
3	Swath width (km)	Cross-track 2330	Cross-track 2330
4	Channel_and_spectral_range(wavelength)	(Bands 1-19)620–965nm (Bands 20-36)3.6–14.39μm	(Bands1-19)620–965nm (Bands20-36)3.6–14.39μm
5	Launch year (LT)	18th December 1999	4th May 2002
6	Equator crossing time and mode (LT)	10:30 (descending)	13:30 (ascending)
7	Multiview observations	No MvO with FoV:110^0	No MvO with FoV:110^0
8	Altitude (km)	705-sun-synchronous, near-polar, circular	705-sun-synchronous, near-polar, circular

3.4 Tropical Rainfall Measuring Mission TRMM

The TRMM is a research satellite that was in operation from 1997–2019 and designed to improve our understanding of the distribution and variability of the precipitation within the tropics as part of water cycle in the current climate system. The TRMM provided much-needed information on rainfall and its associated heat release, which helps to power the global atmospheric circulation that shapes both weather and the climate by covering the tropical and sub-tropical regions of Earth. In coordination with the other satellites in the NASA's Earth Observing System, TRMM provided important precipitation PPT information using several space-borne instruments to increase our understanding of the interactions in between atmospheric aerosol particles, the cloud parameters and precipitation that are central to regulating Earth's climate (Rosenfeld et al., 2014). Figure 3.4 depicts the tropical rainfall measuring mission TRMM satellite schemes. A 22 years of monthly satellite data, from January 1998 to December 2019, were collected from the TRMM satellite web-site portal: https://daac.gsfc.nasa.govdatasets/TRMM_3B43_7/summary?keywords=TRMM_3B43_7/ for this PhD research works.

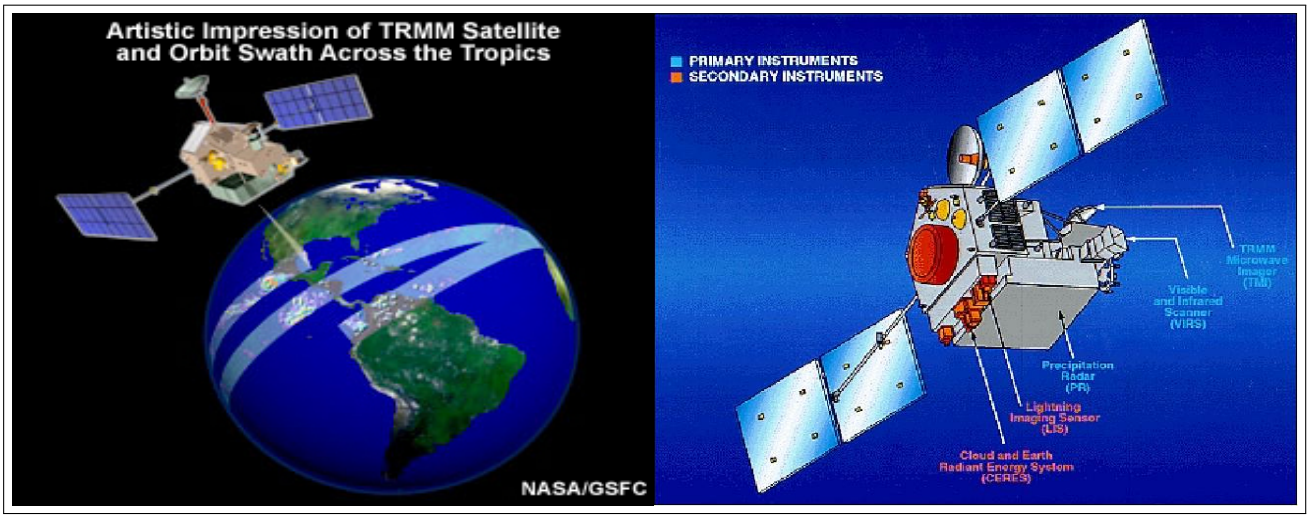

Figure 3.4: The TRMM Satellite Instruments.

Since its launch in 1997, TRMM has provided critical precipitation measurements in the tropical and subtropical regions of our planet Earth. The Precipitation Radar PR looked

through the precipitation column and provided new insights into tropical storm structure and intensification. The TRMM Microwave Imager TMI measured microwave energy emitted by the Earth and its atmosphere to quantify the water vapor, the cloud water and the rainfall intensity in the atmosphere. The TRMM precipitation measurements have made critical inputs to tropical cyclone forecasting, numerical weather prediction and precipitation climatologies, among many other topics, as well as a wide array of societal applications (Simpson et al., 1996).

The TRMM satellite officially ended on 15 April 2015, after the spacecraft depleted its fuel reserves. TRMM was turned off and re-entered Earth's atmosphere on June 15, 2015, over the South Indian Ocean. Originally designed for 3 years, TRMM continued to provide groundbreaking 3-D images of rain and storms for more than 22 years. TRMM has helped spur additional precipitation measurement satellites that contain microwave radiometers, such as the GPM Core Observatory (Kummerow et al., 2000).

3.5 Clouds and Earth's Radiant Energy System CERES

The CERES team has been collecting the Earth Energy Bedget ERB data since 1997, when the first CERES instrument was launched aboard the TRMM satellite. Since then, the CERES instruments have been launched aboard the Terra, Aqua, Suomi National Polar-Orbiting Partnership S-NPP and NOAA-20 satellites. The CERES instruments provide direct measurements of reflected solar radiation and the emission of the thermal infrared radiation into space across all wavelengths between ultraviolet and far-infrared (Wielicki et al., 1998). Those parts of the CERES instruments are already illustrated schematically using Figure 3.3 in Section 3.3 previously. For this PhD research work, the 22 years of monthly satellite data from January 2001 to December 2022 have been collected from Clouds and the Earth's Radiant Energy System CERES satellite web-site portal: https://asdc.larc.nasa.gov/data/CERES/ES4/.

The CERES measurements, together with measurements from higher-resolution imagers on polar orbiting and geostationary satellites, are used along with other input data sources to produce data products that describe the ERB at the top of the atmosphere, within the atmosphere and at the surface. The CERES data products capture variations in ERB at hourly, daily and monthly timescales and at spatial scales ranging from 20 km to global. The data are used by the climate, weather and applied science research communities to address a range of research topics that involve the exchange of energy between the Earth and space and between the major components of the Earth system (Su et al., 2020).

3.6 The Data Analysis Methods

This section deals with retrieval, density estimation, trend test analysis, PCA analysis, Fire-Map model, HYSPLIT trajectory analysis, correlation analysis, and MLR analysis. The MATrix LABoratory MATLAB software was used for the extraction of the satellite imagery data and temporal plots. In addition, we have used the Python programming language for the data extraction and spatial plots.

3.6.1 Satellite Data Retrieval

After the daily-monthly hierarchical data format HDF datasets had been browsed from the MODIS, TRMM, and CERES websites, we extracted the aerosol, clouds, precipitation, and outgoing long-wave radiation parameters, namely AOD, AWV, CFM, CTP, CTT, PPT, and OLR, and then AE-AET was calculated from AOD both using MATLAB and Python codes. This subsection describes the methods we have used to derive the details of those parameter retrievals from the satellite datasets.

The parameter of aerosol optical depth AOD is the measure of the turbidity-opacity of an environment or medium (Chen et al., 2020; Wu et al., 2021; LeBlanc et al., 2020). The optical parameter AOD describes the section of light removed from a beam by scattering

and absorption during its path through the environment (Jin et al., 2023). The AOD values that depend on the sizes, shapes, numbers, concentrations, and the indexes of refraction of the aerosol particles, which are related to the wavelength, can be determined by using the equation as (Symeonidis, 2017):

$$AOD(\lambda) = ln\left(\frac{\phi_e^i, \lambda}{\phi_e^t, \lambda}\right) = -ln(T_\lambda) \tag{3.6.1}$$

where:

ϕ_e^i, λ is the spectral radiant flux in wavelength received;

ϕ_e^t, λ is the spectral radiant flux in wavelength transmitted;

T_λ is the spectral transmittance in wavelength λ.

Typically, the AOD(0.55μm) ranges from 0.05 to 1 over the remote ocean, to 2.0 or even 5.0 during the time of heavy pollution, smoke and dust (B AL-Taie et al., 2020; Patel and Application, 2016). For AOD values x_i, the mean $\bar{x}$ could be calculated as follows (Hopkins and Weeks, 1990; Bryhn and Dimberg, 2011):

$$\bar{x} = \sum_{i=1}^{n}\left(\frac{x_i}{n}\right). \tag{3.6.2}$$

So, the standard deviation S_d is given by:

$$S_d = \sqrt{\frac{1}{n}\sum_{1}^{n}(x_i - \bar{x})^2}. \tag{3.6.3}$$

And the coefficient of variation CV in % is:

$$CV(\%) = \frac{S_d}{\bar{x}} \times 100\%. \tag{3.6.4}$$

The parameter Ångström exponent AET is one of the basic optical parameters that widely used in the atmospheric sciences, dealing with the optical properties of aerosol particles. This optical parameter is treated as the indirect measure of the aerosol size in a given column of air. Given the turbidity coefficient β, then AET had been calculated from the

AOD values using the equation from (Thapa et al., 2016):

$$AOD(\lambda) = \beta\lambda^{-AET} \text{ and then,}$$
$$AET = \frac{ln(\beta) - ln\{AOD(\lambda)\}}{ln(\lambda)}. \tag{3.6.5}$$

3.6.2 Density Distribution Estimation

There are various attempts to estimate the density distribution between the dependence values and independence observations (Bulmer, 1975; Chung et al., 2019). The kernel density distribution estimator for dependent data is exactly the same as for independent data, which means that when designing methods to estimate the density distribution, we can proceed exactly as for independent data (Hall and Ooi, 2004; Okabe et al., 2009; Zambom and Ronaldo, 2013). The traditional kernel estimator of f(y) at point y can be expressed as (Izenman, 2008):

$$\hat{f}_n(y) = \frac{1}{nh}\sum_{i=1}^{n} K\left(\frac{y - y_i}{h}\right) \tag{3.6.6}$$

where:

n is the number of observations,

h is the bandwidth which determines the smoothness of the density estimate, and

K(·) is a non-negative kernel function that integrates into one with a mean zero.

More specifically, the gaussian form of the kernel density distribution estimator for the parameters could be expressed as follows (Harvey and Oryshchenko, 2012):

$$K(u) = \frac{1}{\sqrt{2\pi}} e^{-\frac{1}{2}u^2}. \tag{3.6.7}$$

3.6.3 Mann-Kendall Trend Test

A statistical test for a trend is used to assess whether a set of data values is increasing or decreasing over time and whether the trend in either direction is statistically significant (Jung et al., 2019; Helsel and Frans, 2006; Bryhn and Dimberg, 2011). The trend test

component of the time series is determined by using the Mann-Kendall rank statistic to detect abrupt changes in the satellite-derived estimates (McLeod, 2005; Patakamuri et al., 2020; Jiang et al., 2007). This technique, the statistically ranked trend test, is considered the most appropriate for the analysis of climatic changes in climatological time series for the detection of a climatic discontinuity (Sneyers et al., 1991; Chrysoulakis and Cartalis, 2002; Partal and Kahya, 2006). The test employs the ranks y^i of all the terms, x^i in a series that has been arranged in increasing order of magnitude. The number n^i of elements y^i preceding it (i > j) is calculated for each element y^i so that $y^i > y^j$, which is given by the test statistic as (Zhang et al., 2018; Zarenistanak et al., 2014; Khattak et al., 2011; Ahmad et al., 2015):

$$t^i = \sum_i n^i. \tag{3.6.8}$$

The Mann-Kendall statistic test is calculated using (Hirsch et al., 1982; Duffney et al., 2023):

$$S(x) = \sum_{j=1}^{n-1} \sum_{i=j+1}^{n} sgn(x^i - x^j) \tag{3.6.9}$$

with $x = x^i - x^j$:

$$sgn(x) = \begin{cases} 1 & if\ x > 0, \\ 0 & if\ x = 0, \\ -1 & if\ x < 0. \end{cases} \tag{3.6.10}$$

The variance of the MK test statistic can be computed as:

$$Var(t) = \frac{n(n-1)(2n+5)}{72}. \tag{3.6.11}$$

The statistic S is approximately normal distributed provided that the following Z-transformation is employed:

$$Z = \begin{cases} \frac{S-1}{\sqrt{Vat(S)}} & if\ S > 0, \\ 0 & if\ S = 0, \\ \frac{S+1}{\sqrt{Vat(S)}} & if\ S < 0. \end{cases} \tag{3.6.12}$$

The distribution function under the null hypothesis is asymptotically normal with mean and variance calculated as follows:

$$E(t) = \frac{n(n-1)}{4}. \tag{3.6.13}$$

And for large values of u(t);

$$u(t) = \frac{n(t) - E(t)}{\sqrt{Var(t)}}. \tag{3.6.14}$$

A probability a_1 can be determined using a standard normal distribution table such that:

$$a_1 = P(|u| > |u(t)|)\frac{n(t) - E(t)}{\sqrt{Var(t)}}. \tag{3.6.15}$$

Finally, rejecting or accepting the null hypothesis at a level depends on whether $a_1 > a_0$ or $a_1 < a_0$. If the absolute values of u(t) are higher than 1.96, they indicate an increasing or decreasing trend (Ngaina, 2015; Ahmad et al., 2015; Nasri and Modarres, 2009). In the case of a significant trend at $a_0 = 0.05$ on the series, the start of the phenomena is located through sequential analysis. The total number of observations is given as N. Therefore, the values of u'(t) for the reversed series can be calculated similarly to u(t). Curves that overlap several times indicate the absence of a trend. In this study, the significance level a_0 is considered to be 0.05, i.e., at the 95% confidence interval.

3.6.4 Principal Component Analysis

The principal component analysis PCA is useful for compressing geophysical data in space-time and separating noise from meaningful data that converts the data to a new coordinate system. PCA involves the transformation of variables into a linear combination of orthogonal components. A series of axes provides location of each data points which represents separate uncorrelated information. The output is covariance matrix denoting transformation coefficients listed in decreasing order of variation. Let P be an m x n matrix of daily data, where m is the number of days and n is the number of stations. This matrix can be decomposed into linear functions of m temporal and n spatial vectors so

that the observation P_{ij} on day i at station j is given by (Stephenson et al., 1999; Gitau et al., 2013; Ledesma and Valero-Mora, 2019):

$$P_{ij} = \sum_{k=1}^{n} a_{ik} e_{jk}, \quad P = \sum P_{ij} = ae \tag{3.6.16}$$

where a_{ik} is the element for day i in k^{th} time vector and $e_{jk}$the element for station j in k^{th} space vector.

The standardized dataset(A_{ij}) and symmetric n x n correlation matrix C are given as:

$$A_{ij} = \frac{P_{ij} - \bar{P}_{ij}}{S_d} \text{ and } C = \frac{A'A}{m-1} \tag{3.6.17}$$

The eigenvectors e are space vectors and the corresponding eigenvalues λ are measures of the explained variance accounted for each eigenvector. Decomposition of correlation matrix into eigenvectors e, and associated eigenvalues λ are obtained by solving:

$$(C - \lambda I)e = 0, \quad |(C - \lambda I)| = 0 \tag{3.6.18}$$

Given p x m matrix, U_m = (u_1, u_2, u_3 ...., u_m) of PCA loadings. Simplifying with rotation can be achieved by seeking an m x m rotation matrix R to construct rotation of the empirical orthogonal functions REOFs K according to (Hansen et al., 2008);

$$K = U_m \beta \tag{3.6.19}$$

Maximum factor loadings after rotation that is the correlation coefficients between the variables and factors will be used to determine the relation of selected variables, the parameters for the aerosol optical properties, clouds and precipitations. The simplicity criterion for choosing the rotation matrix for maximization problem is expressed by:

$$max f(U_m \beta). \tag{3.6.20}$$

3.6.5 HYSPLIT Trajectory Analysis

TThe air mass transport model, HYbrid Single-Particle Lagrangian Integrated Trajectory HYSPLIT is completed system for computing both simple air parcel trajectories and

complex dispersion and deposition simulations. The model calculation method is a hybrid between the Lagrangian approach and the Eulerian approach. The Lagrangian approach uses a moving frame of reference as the air parcel moves from their initial location. And the Eulerian approach uses a fixed three-dimensional grid as a frame of reference (Huang et al., 2009; Lu et al., 2022).

An advection and diffusion calculations are made in Lagrangian framework following the transport of the air parcel, while pollutant concentrations are calculated on a fixed grid. By using the model, advection of the particle can be computed from the average of the three-dimensional velocity vectors at the initial position P(t) and first-guess position P'(t+Δt). Respectively, the first guess and final positions are given by (Duy et al., 2022):

$$\begin{aligned} P'(t+\Delta t) &= P(t) + V(P,t)\Delta t \quad [first], \\ P(t+\Delta t) &= P(t) + 0.5V(P,t) + V(P',t+\Delta t)\Delta t \quad [final]. \end{aligned} \tag{3.6.21}$$

During the simulation, the integration time-step Δt can vary. Advection distance per time-step should be less than the grid spacing in all computation. The trajectory analysis uses an integration method (Kreyszig 1968). Greater precision cannot be achieved using higher order integration methods due to the linear interpolation of data from the grid to the integration point. If the trajectories exit the meteorological data grid, they are usually terminated. However, advection continues along the surface if the trajectories intersect the ground. For our study, starting points was identified at the center of sub-grids within the East Africa-Ethiopia domain and used to conduct back trajectory analysis from each center. For each sub-grid on each calendar day, precipitation anomalies were marched with the upwind aerosol at the endpoints

3.6.6 Multiple Linear Regression Analysis

Determination of the combined effect of aerosol particles and clouds on precipitation utilized a multiple linear regression MLR analysis. MLR analysis is to determine which variable in a set of variables is the best predictor of an outcome. The MLR first-order

models are given as (Ahmad et al., 2019; Abdullah et al., 2017; Ngaina, 2015):

$$Y_i = \beta_0 + \beta_1 x_{1i} + \beta_2 x_{2i} + \beta_3 x_{3i} + \cdots + \beta_k x_{ki} + \varepsilon_i \leftrightharpoons \mathbf{B_k} = [\mathbf{1}\ \mathbf{X_{ki}}] \backslash [\mathbf{Y_i} - \varepsilon_\mathbf{i}] \quad (3.6.22)$$

where:

Y_i is the value of the response variable in the i^{th} observation;

β_k is the slope parameter associated with the k^{th} variable;

β_0 is the intercept parameter;

x_{ki} is the k^{th} independent variable associated with the i^{th} observation;

ε_i is the random error term with mean $E(\epsilon_i) = 0$ and variance $\sigma^2(\epsilon_i) = \sigma^2$.

In MLR analysis, the least squares method is used to find a function that fits a given data. The method minimizes the sum of the n squared errors SSE of the observed values y_i and the predicted values on the fitted line $\hat{y}_i$.

$$\sum_{i=1}^{n} (y_i - \hat{y}^2) \quad (3.6.23)$$

The variable inflation factors VIFs measure the impact of the collinearity on the standard errors of the estimate variables. The square root of VIF shows the inflation of standard error by the other variables in the model. The VIF for each independent variable can be computed as follows (Young et al., 2008; Ostertagová, 2012):

$$VIF_k = (1 - R_k^2)^{-1} \quad (3.6.24)$$

Akaike information criterion AIC measures the relative quality of the statistical model for a given set of data with tradeoffs between complexity and goodness of fit of model. AIC statistic is calculated as:

$$AIC = nln\left(\frac{SSE}{n}\right) + 2p \quad (3.6.25)$$

where p and n represent the number of independent variables and observations.

And the residual normality of the model can be checked using the Quantile-Quantile QQ plots computed as follows:

$$Q_{yi}\langle\tau|x\rangle = \beta_0 + \beta_i x_i + F_u^{-1}(\tau) \tag{3.6.26}$$

where Q_{yi} is response variable conditional value and F_u the error common distribution function given τ.

3.6.7 Aerosol Particles Radiative Forcing

The knowledge of atmospheric aerosol particles loading is important as it can change the weather and climate patterns by perturbing the radiation budget over any region. Top of the atmosphere TOA and surface radiative forcing are defined as the perturbation in the upscattered solar radiation flux F_{up} and surface reaching solar intensity F_{down}, respectively, with change in the AOD. The surface radiative forcing has been calculated from the following equation (Christopher et al., 1996):

$$F_{Surf} = -0.5 F_T T^2 (1 - A_c)(1 - \bar{R}_s^2)\bar{\beta}\tau \tag{3.6.27}$$

where:

F_T is the solar constant 1370 W/m^2,

T is surface temperature in Kelvin,

A_c is the fractional cloud cover,

$\bar{R}_s$ is the mean albedo of the underlying surface,

$\bar{\beta}$ is the fraction of the radiation scattered upward by the aerosol column and

τ is the areal mean optical depth of the aerosol.

The TOA forcing has been estimated using the CERES Earth radiation budget data and the AOD data from MODIS data. The clear-sky TOA shortwave flux from the CERES has been taken as an estimate of cloud-free aerosol forcing F_{AER} over dusty areas, while the aerosol-free estimates of F_{CLR} come from the observations of the CERES (Christopher and Zhang, 2002).

Then the TOA forcing is given as:

$$F_{TOA} = F_{CLR} - F_{AER} \tag{3.6.28}$$

where:

F_{CLR} is aerosol free flux estimate,

F_{AER} is the flux estimate over aerosol laden areas.

The atmospheric forcing is given by the difference between TOA and surface:

$$F_{Atm} = F_{TOA} - F_{Surf} \tag{3.6.29}$$

The net atmospheric radiative forcing is converted into heat inside the layers containing the absorbing particles, which results in an increase in their temperature and alters the regional climate. Using the basic laws of thermodynamics, the derivation of the temporal rate of this increase is straight-forward (Liou, 2002; Pilewskie, 2007; Li et al., 2016):

$$\frac{\partial T}{\partial t} = \frac{g}{C_p}\frac{\Delta F}{\Delta P}. \tag{3.6.30}$$

where:

T is the temperature in Kelvin,

t is the time in seconds,

g is the gravitational acceleration in meter per second square,

ΔF is the radiative forcing difference between TOA and surface,

C_p is the specific heat capacity at constant pressure, and

ΔP is the height of the column containing the aerosol particles expressed as the difference of atmospheric pressure between its bottom and top.

Chapter 4

Classification of Aerosol Particles and Their Temporal Distribution Over East Africa–Ethiopia Using MODIS Satellite Data

This chapter is to be cited as:

Alemu, A. A. and Raju, J. P.: Classification of Aerosol Particles and Their Temporal Distribution Over East Africa–Ethiopia Using MODIS Satellite Data: Part 01, Journal of Quantitative Spectroscopy & Radiative Transfer JQSRT, Elsevier, 325, 109085, 2024.

4.1 Introduction

Atmospheric aerosol particles differ in their sources, sizes, shapes, compositions, and lifetimes depending on their origins and subsequent atmospheric processing (Kafle and Coulter, 2013; Grythe, 2017). According to their sources, aerosol particles can be broadly classified as maritime, urban, dust, sea salt, biomass burning and sulfate (Mukai, 2018; Briffa et al., 2020; Rizza et al., 2019; Falah et al., 2022a). Primarily, they are released from Earth to the atmosphere through both natural and anthropogenic sources that include biomass burning, incomplete combustion of fossil fuels, volcanic eruptions and wind-driven or traffic–related suspension of road, soil and mineral dust, sea salt, sand and biological

materials (Chi et al., 2019; Gaffney et al., 2006b; Filioglou et al., 2020). In addition, some aerosol particles are also formed through various physical and chemical processes in the atmosphere as their secondary sources (Behera, 2016; Li et al., 2015a; Huang et al., 2020). The aerosol optical properties, such as the aerosol optical depth AOD, which indicates aerosol concentration, and the Ångström exponent AE related to the size distribution of aerosol particles, are used in classifying various aerosol types by their sources (Shafique et al., 2022; B AL-Taie et al., 2020; Kumar et al., 2015). From the previous literature reviews, we found that there are few studies on atmospheric aerosols in the East Africa and Ethiopia regions using ground or satellite (Homa et al., 2017; Getachew, 2009; Eshet and Raju, 2022). However, to date, no one has reported the classification of major atmospheric aerosol particle types and their temporal size distribution variability using the Moderate Resolution Imaging Spectroradiometer MODIS satellite. Hence, in this study, we used the climatological database of AOD and AE from MODIS satellite instruments to identify the dominant types and sizes of aerosol particles over East Africa–Ethiopia.

4.2 Results and Discussion

After extracting the Hierarchical Data Format HDF datasets and collecting the daily AOD values from January 01, 2001–December 31, 2022, from MODIS satellites, daily AE values were calculated using the formula described in methodology section 3.6.1, and monthly, seasonal, and yearly averages were obtained for selected sites clustered into four regions, i.e., southwest, southeast, northwest, and northeast of the study area. In this section, we discuss the classification of aerosol particles and long-term trends using the Mann-Kendall statistical rank test.

4.2.1 Variability of Aerosol Concentration

Daily Variation of Aerosol Concentration

The daily fluctuations of the AOD and AE optical parameters for the chosen sites at four clustered regions are plotted in Figures 4.1(a)–(d). In the southwest cluster (Fig. 4.1(a)), the minimum AOD and AE are observed in South Sudan at the Juba site from both Terra and Aqua instruments, while the maximum AOD and AE is still observed at the Juba site from Aqua and Terra in Ethiopia at the Agnuak site. For the southeast cluster (Fig. 4.1(b)) both Terra and Aqua depict the minimum and maximum AOD and AE values in Ethiopia, with the minimum at the Kebri Dahar site and the maximum values at the Awassa site.

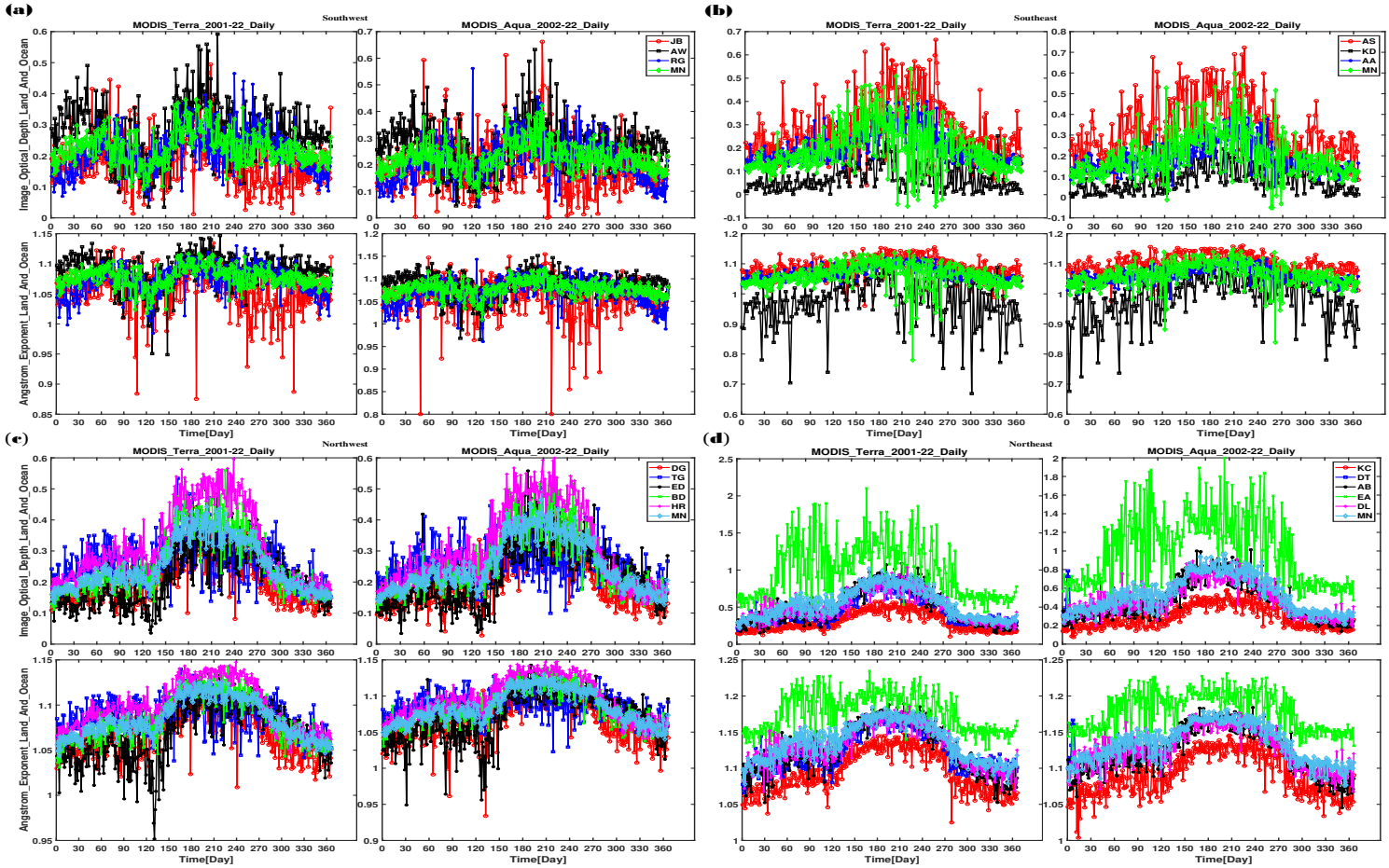

Figure 4.1: The aerosol optical parameters daily variation.

The northwest cluster shows (Fig. 4.1(c)) minimum AOD and AE values in Ethiopia, at the Ethiopian Renascence Dam and Dangote sites from both Terra and Aqua, while both AOD and AE maximum values are still observed in Ethiopia at the Humera site. And at the northeast cluster (Fig. 4.1(d)), both AOD and AE have minimums at the Kombolcha site, while their maximum values are at Erta Ale, both in Ethiopia.

In general, the minimum AOD and AE values were observed in the southeast cluster, while the maximum AOD and AE values were observed in the northeast cluster from both instruments. For the Terra satellite, those minimum values of AOD and AE were found to be 0.00 and 0.67 on December 16, while the maximum values were to be 2.10 and 1.23 observed on June 22. Similarly, for the Terra satellite, minimum values were observed on January 07 with 0.00 and 0.68, while the maximum values were 2.00 and 1.23 on July 24. We conclude that the minimum AOD and AE values observed at Kebri Dahar site, while the maximum values are at Erta Ale site, both are located in Ethiopia. Those maximum AOD and AE values were attributed to high aerosol productivity from the manufacturing industry and heavy traffic dusts at Juba and Awassa sites, biomass burning at Agnuak and Humera sites, and volcanic activities and the marines transportation at Erta Ale sites (Chi et al., 2019; Gaffney et al., 2006b; Filioglou et al., 2020; Kaufman et al., 1990).

Monthly Variation of Aerosol Concentration

Monthly mean values are constructed based on daily values of AOD and AE parameters for each site of the four clustered regions, and results are illustrated in Figures 4.2(a)–(d). In the southwest cluster (Fig. 4.2(a)), the minimum AOD and AE values are observed in South Sudan at the Juba site from Terra and at the Raga site for Aqua satellite, while the maximum values are observed in Ethiopia at the Agnuak site from both instruments. For the southeast cluster (Fig. 4.2(b)), the minimum AOD and AE values are observed at the Kebri Dahar site, and the maximum values are observed at the Awassa site of Ethiopia. For the northwest cluster (Fig. 4.2(c)), minimum AOD and AE values are observed

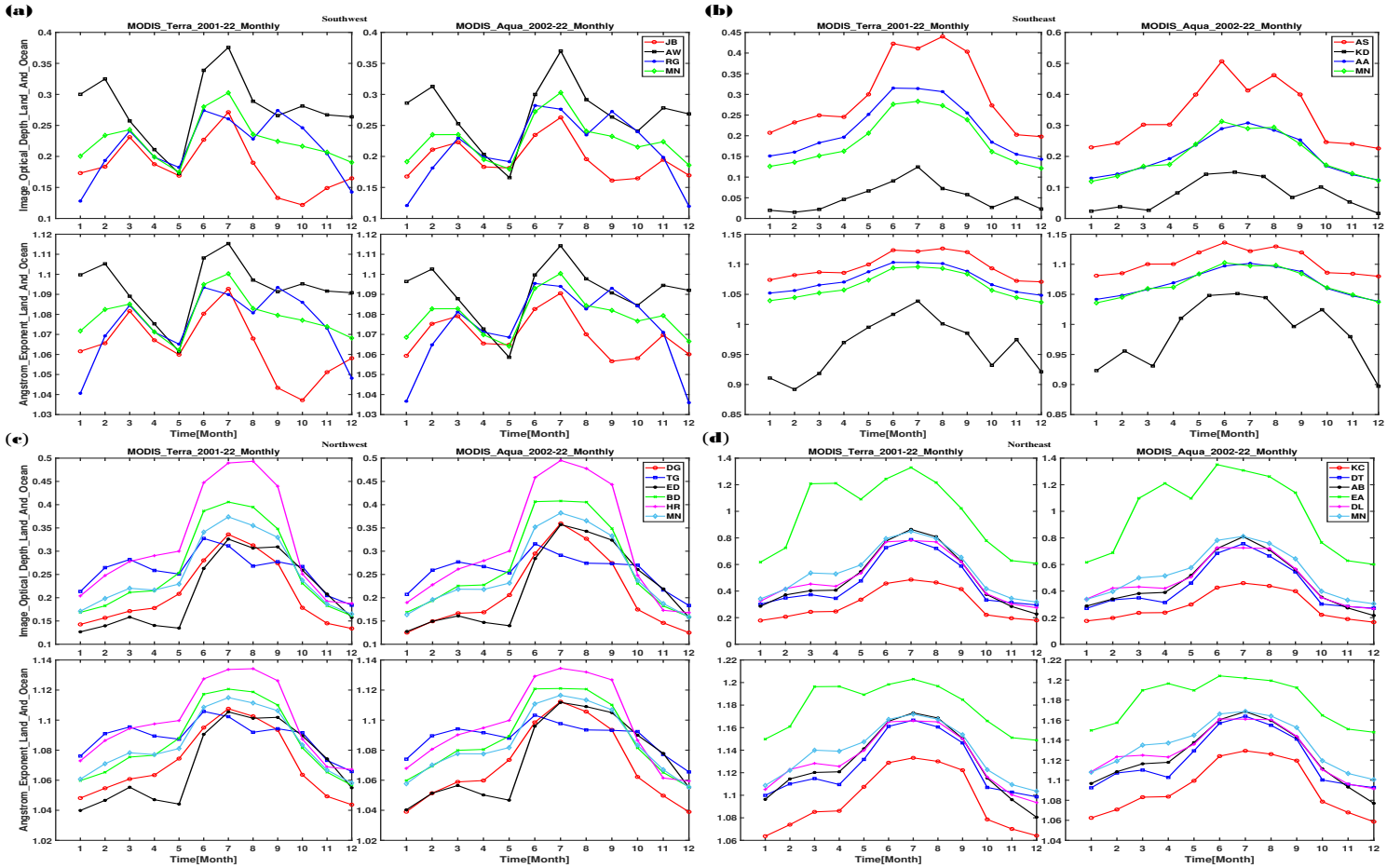

Figure 4.2: The aerosol optical parameters monthly variation.

in the Ethiopian Renascence Dam and Dangote sites of Ethiopia from Terra and Aqua instruments, while both AOD and AE maximum values are observed again in Ethiopia at the Humera site. When we move to the northeast cluster (Fig. 4.2(d)), both AOD and AE values were at their minimums at the Kombolcha site, while their maximum values were at Erta Ale, both in Ethiopia.

To generalize, the minimum AOD and AE values are observed in the southeast cluster, while the maximum AOD and AE values are observed in the northeast cluster from both instruments. For the Terra satellite, the minimum values of AOD and AE were found to be 0.02 and 0.89 in December and January, while the maximum values were to be 1.33 and 1.20 in June. Moreover, Aqua satellite also shows similar results, with minimum AOD and AE values observed during December and January with 0.02 and 0.90, respectively,

while the maximum values in July at the two clusters (Fig. 4.2(b, d)) are 1.35 and 1.20. From the figure, we can observe that all of the minimum AOD and AE values are at the Kebri Dahar site, while the maximum values are at the Erta Ale site, both in Ethiopia. The maximum AOD and AE values in June and July months confirmed that they were attributed to high aerosol production from the manufacturing industry and heavy traffic dusts at Juba and Awassa sites, biomass burning at Agnuak and Humera sites, and volcanic activities and the marines transportation at Erta Ale sites during those months (Filioglou et al., 2020; Homa et al., 2017; Eshet and Raju, 2022; Kaur et al., 2012).

Seasonal Variation of Aerosol Concentration

The seasonal variations of the aerosol particle optical parameters AOD and AE at the selected sites clustered into four areas are addressed in this section. The evolution of these parameters, estimated from the study periods of 2001–2022, is shown in Figures 4.3(a–d), together with their corresponding total average means. The minimum AOD and AE values are found in the Belg season except in the northwest cluster (Fig. 4.3(c)), which is in Baga, and the maximum values are in the Kiremt season in all clusters, which are similar to the findings and the reasons in the study (Liu et al., 2021) from eastern China. The minimum values are 0.15 and 1.03 in the Bega season for Terra and 0.16 and 1.03 in the Belg season for Aqua, and the maximum are all in the Kiremt season: 0.86 and 1.17 for Terra and 0.84 and 1.17 for Aqua, respectively.

Still, as in the previous results of sections 4.2.1 and 4.2.1, the Kombolcha site has minimum values and the Arta Ale site has maximum values in the cluster to which they belong, i.e., they both belong to the northeast cluster (Fig. 4.3(d)). The seasonal AOD and AE results were similar to those of the observations made in Austria (Yang et al., 2021), Algeria (Kharol et al., 2011), eastern China (Liu et al., 2021), and Hong Kong (Yu et al., 2022), despite the fact that there had been no prior studies on the sites in the clustered regions. The discrepancies we discovered were in the minimums with different data periods and

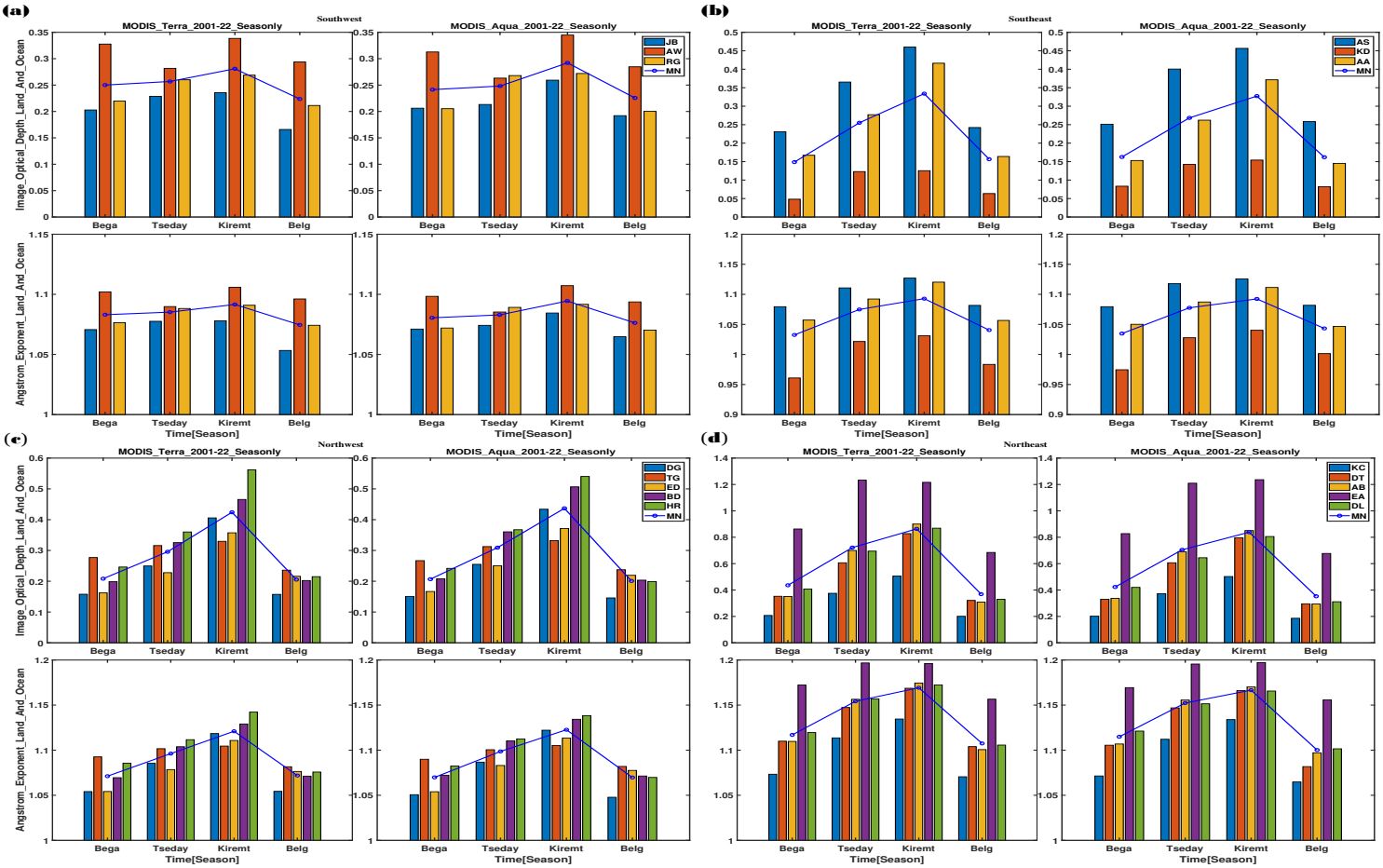

Figure 4.3: The aerosol optical parameters seasonal variation.

site selections. Furthermore, in the study conducted by (Yu et al., 2022) the minimums were primarily at Bega and the maximums at Kiremt. Therefore, almost all of the results in the figures indicate extreme values at similar locales, like those of the observations in Figures 4.1(a–d) and 4.2(a–d), with a few noted exceptions.

Yearly Variation of Aerosol Concentration

In this section, we summarise the total yearly variations of the aerosol particles optical parameters AOD and AE for all the selected sites belonging to the four clustered regions. The first panel in Figure 4.4(a) indicates the yearly variations for the AOD values from Terra and Aqua satellites, and the second panel represents the same with AE parameters corresponding to the selected sites in the southwest cluster, and the average of all the sites

is also superimposed on all plots. Similarly, Figures 4.4(b–d) produce yearly variations of AOD and AE for the remaining three clustered regions. The majority of the sites, both in the western and eastern cluster zones, clearly demonstrate interannual variability with frequent minimum and maximum values of AOD and AE optical parameters, as repeated in the aforementioned figures. The average of the clustered regions shows the minimum at the southeast cluster in 2003 from both instruments, and the maximum were at the northeast cluster in 2011 for the Terra satellite and in 2013 for the Aqua satellite. Accordingly, the AOD and AE minimum values are 0.11 and 1.03 for Terra

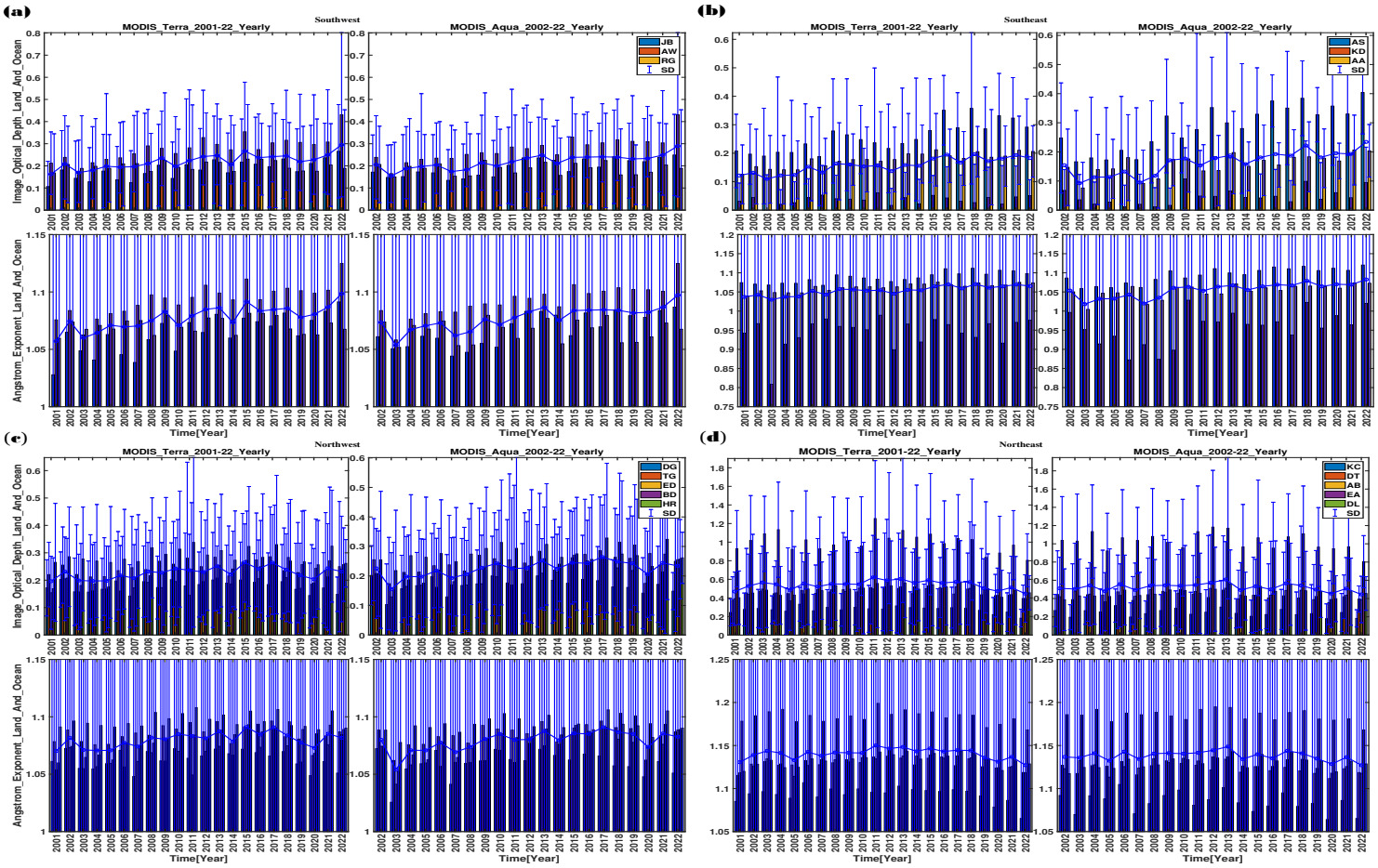

Figure 4.4: The aerosol optical parameters yearly variation.

and 0.09 and 1.02 for Aqua, and the maximum are 0.62 and 1.15 for Terra and 0.61 and 1.15 for Aqua, respectively. The AOD and AE maximum values during 2011 and 2013 confirmed that there were high aerosol productions from the manufacturing industry and

heavy traffic dusts at Juba and Awassa sites, biomass burning at Agnuak and Humera sites, and volcanic activities and marine transportation at Erta Ale sites during those years (Filioglou et al., 2020; Homa et al., 2017; Eshet and Raju, 2022; Kaur et al., 2012).

4.2.2 Aerosol Classification using Daily Concentration

This section deals with the classification of aerosol particles using the Kernel density distribution estimator formulation. First, we collected the daily AOD and AE values for 22 years, then, by applying the thresholds mentioned in Table 4.1, we classify the aerosols into five different types, i.e., (I) maritime MR, (II) dust DS, (III) biomass burning BB, (IV) desert dust DD, and (V) urban UR. The remaining values that do not fit into any of these groups are characterized as mixed MX types (B AL-Taie et al., 2020; Kumar et al., 2015; Pathak et al., 2012; Toledano et al., 2007). Here, some of the domains are difficult to separate because different aerosols types have overlapping characteristic parameters (Nicolae et al., 2019). Table 4.1 shows the criteria for classification of the dominant aerosol particles types.

Table 4.1: The threshold values based on AOD and AE for aerosol particles type classification.

Aerosol type	Aerosol optical depth (AOD)	Angstrom exponent (AE)
Maritime (MR)	< 0.3	0.5–1.7
Dust (DS)	> 0.4	< 1.0
Urban (UR)	0.2–0.4	> 1.0
Desert Dust (DD)	> 0.45	0.4–2.0
Biomass Burning (BB)	>0.7	>1.0
Mixed (MX)	- Remaining (R) -	- Remaining (R) -

The results shown in Figures 4.5(a)–(d) and 4.6(a)–(d) were computed using the density distribution estimation method with the daily AOD and AE values as inputs. These

values were obtained by using the optical properties retrieval procedures we covered in Sections 3.6.1 and 3.6.2. In the southwest cluster, the lowest MR and MX aerosol particles types were observed during the Kiremt season, while these aerosol particles types were found more dominantly during the Bega season from both Terra and Aqua satellites. In this cluster, low vales of UR were observed during the Kiremt season from the Terra and during the Tseday season from the Aqua, while they were found more dominantly during the Bega season. And the lowest dominant DD aerosol particles were observed during the Kiremt season from the Terra and during the Belg season from the Aqua, while they were found more dominantly during the Bega season from both instruments. The BB aerosol particles types were least dominant during the Belg season from both of

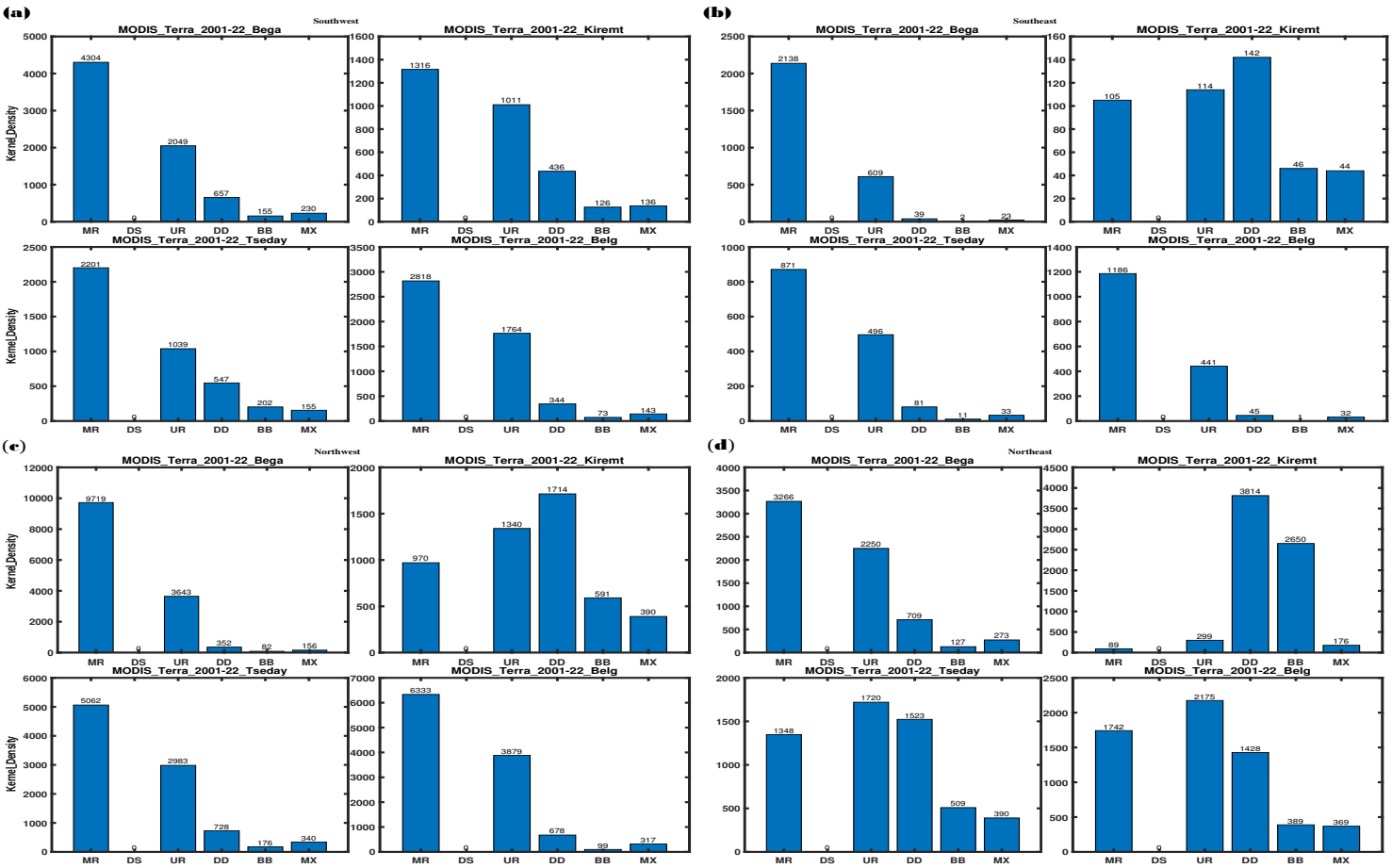

Figure 4.5: The AOD Vs AE Kernel density variation plots [Terra].

the instruments, while they were more dominant during the Tseday season from Terra and

Bega season from Aqua in the cluster. This cluster shows that the least dominant were the BB aerosol particles types observed during the Belg season, and the most dominant was the MR aerosol particle type observed during the Bega season from both Terra and Aqua instruments. And in the southeast cluster, the lowest dominant MR and UR aerosol particles types were observed during the Kiremt season, while these aerosol particles types were found more dominantly during the Bega season from both Terra and Aqua satellites. And the lowest dominant DD, BB, and MX aerosol particles types were observed during

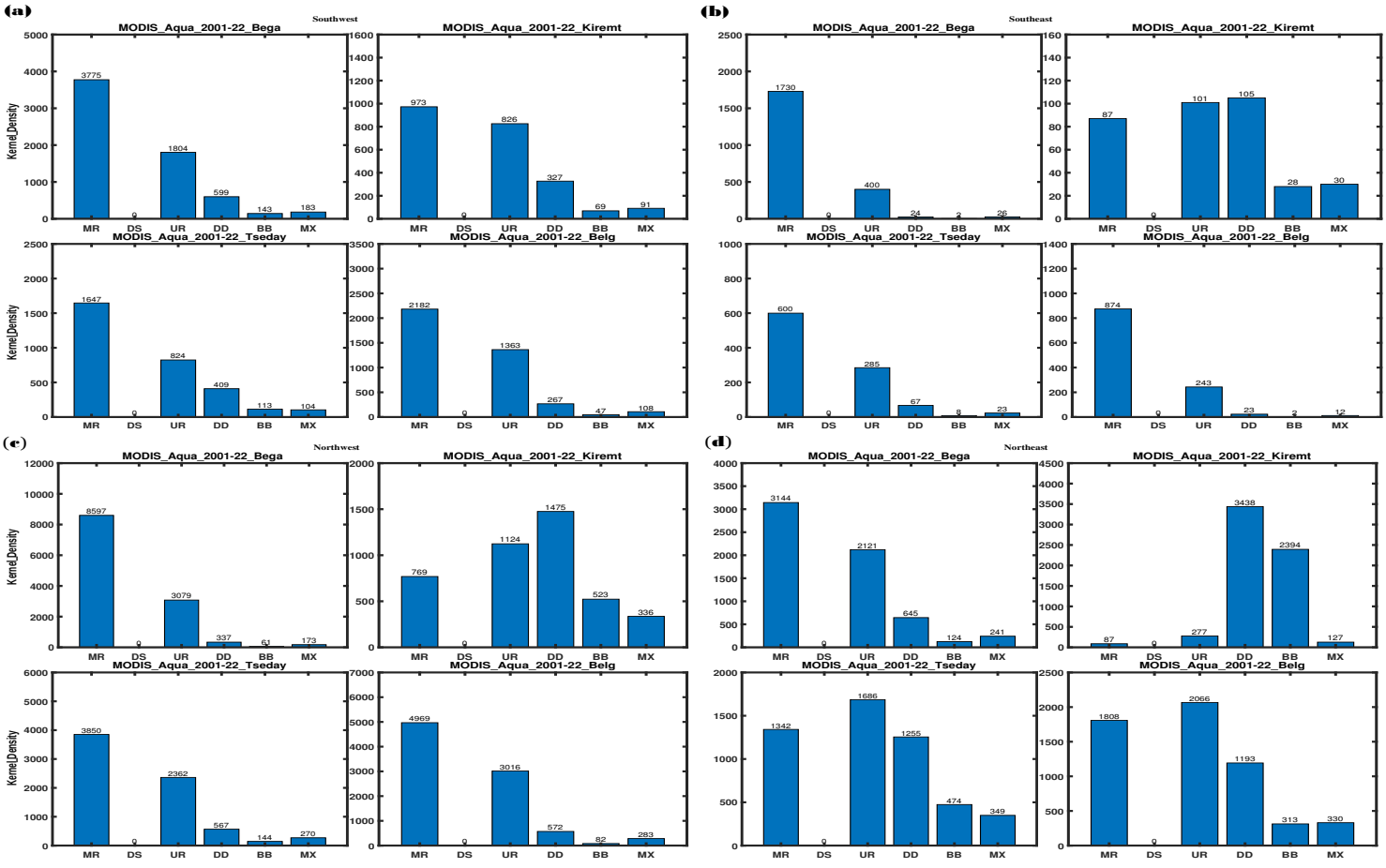

Figure 4.6: The AOD Vs AE Kernel density variation plots [Aqua].

Belg from both instruments. However, the lowest dominant DD and MX aerosol particles types occurred during the Baga season from Terra, while these aerosol particles types were found more dominantly during the Kiremt season from both instruments in the cluster. This cluster shows that the least dominant was the BB aerosol particle type

observed during the Belg season, and the most dominant was the MR aerosol particle type observed during the Bega season from both Terra and Aqua instruments.

In the northwest cluster, the lowest dominant MR and UR aerosol particles types were observed during the Kiremt season. These types of aerosol particles were found most dominantly during the Bega season on both the Terra and Aqua satellites. But the most dominant UR aerosol particle type occurred during the Belg season from Terra. And the lowest dominant DD, BB and MX aerosol particles types were observed during Bega from both instruments, while these aerosol particles types were found more dominantly during the Kiremt season from those instruments in the cluster. This cluster shows that the least dominant were the BB aerosol particles types observed during the Bega season, and the most dominant was the MR aerosol particle type still observed during the Bega season from both Terra and Aqua instruments. And coming to the southwest cluster, the lowest dominant MR, UR, and MX aerosol particles types were observed during the Kiremt season. These aerosol particles types were found more dominantly during the Bega season from both Terra and Aqua satellites, with the most dominant MX aerosol particles types occurring during the Tseday season from Terra. And the lowest dominant DD and BB aerosol particles types were observed during Bega from both instruments, while these aerosol particles types were found more dominantly during the Kiremt season from both instruments in the cluster. This cluster shows that the least dominant was the BB aerosol particle type observed during the Bega season, and the most dominant was the MR aerosol particle type still observed during the Bega season from both Terra and Aqua instruments.

The findings lead to the conclusion that 47.71% of marine MR-type aerosol particles were the most dominant in the study areas. Subsequently, 28.29% of urban UR types and 14.65% of Desert Dust DD types were the third dominant aerosol particles. 5.83% mixed MX types and 3.52% biomass burning BB types were less dominant aerosol particle types, 0.00% dust DS aerosol particles types in all clusters and seasons. The dominant

aerosol particles (MR and UR types) found in the study areas originate from natural or anthropogenic influences in local and regional areas and are transported from seabed countries such as Djibouti (Boiyo et al., 2018a; Torres-Delgado et al., 2021; Li et al., 2021c). In addition, the desert dust DD aerosol particles from Somalian and Eritrean countries could be transported to the study area (Eshet and Raju, 2022). The frequency of aerosol particles occurrence density varies between four clustered regions and four seasons from both satellites, with Kiremt season having minima in the southeastern clusters and Bega season having maxima in the southwestern clusters. The relative seasonal influence of each aerosol particle type depends significantly on local meteorology, air mass transport, aerosol particle mixing and chemical processes, and the mechanisms of formation and removal of the vertical atmospheric column (Matthias et al., 2004). In addition, increased relative humidity and hygroscopic growth of water vapour particles play an important role in changing aerosol particle concentration (Elansky et al., 2018; Filonchyk et al., 2020).

4.2.3 Trend Analysis of Aerosol Concentration

This section describes the annual statistical trend tests for the optical parameters of aerosol particles over the sixteen sites clustered in four regions. We have applied the Mann-Kendall rank forward statistical trend test with the Sen's slope method, which is described in the methodology section on yearly values of AOD and AE parameters, and the results are displayed in Figures 4.7(a)–(d) for the forward trend and Figures 4.8(a)–(d) for the backward-reverse trend for the four clustered regions. The left-hand side of the first vertical panel of Figures 4.7(a)–(d) shows trends for AOD and AE using the Terra satellite, and the right-side panel for the Aqua satellite. It is clearly evident that there is a slightly increasing forward and decreasing reverse trend variation at the southwest cluster of Juba and Agnuak, at the southeast cluster of Awassa and Addis Ababa, for the northwest cluster of Bahir Dar, and at the Ethiopian Renascence Dam sites. The remaining sites from these clusters and all the sites at the northeast cluster show almost

slightly up and down, and down parabolic vibrating trend variation respectively. The trend test is almost similar for both the Terra and Aqua instruments, with the minimum and maximum trend variations at the northwest and northeast clusters, respectively.

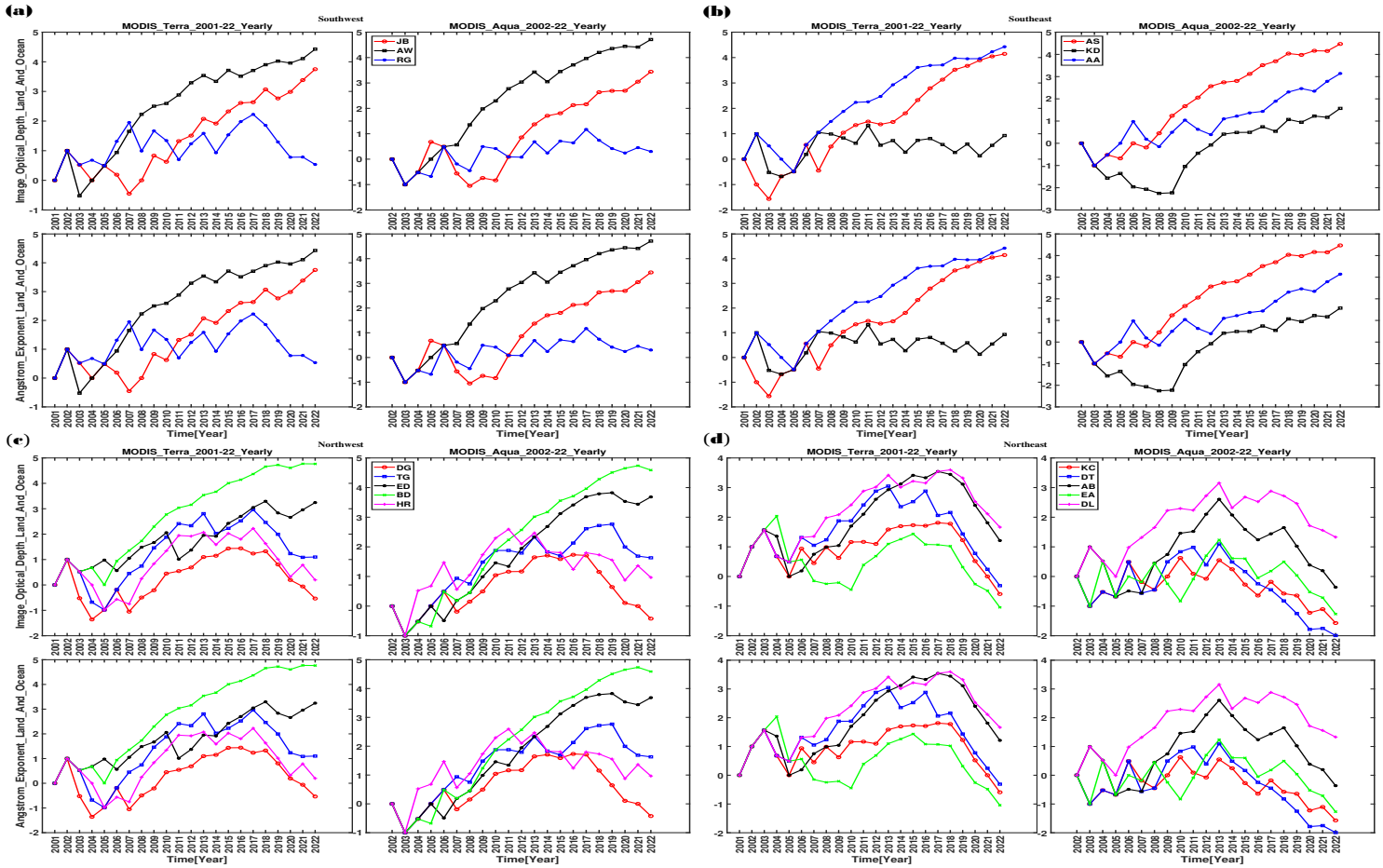

Figure 4.7: The Mann-Kendall rank forward statistic trends tes.

The statistical trend tests confirm the significance of the positively increasing aerosol particles concentration during the study period. Over the southern clusters, despite the increasing trend, declining aerosol particles concentration and size were observed during 2002–2003 at the Aguak site, during 2002–2007 at the Juba site, and during 2017–2022 at the Raga site, in the southwest cluster; and during 2001–2003 at the Awassa site, during 2002–2005 at the Addis Ababa site, and during 2002–2009 at the Kebri Dahar site, in the southeast cluster, respectively. And over the northern clusters, we find declining aerosol particles concentration and size during 2010–2022 at the Humera site, during 2017–2022

at the Dangote site, and during 2019–2022 at the Tonga site, in the northwest cluster; and during 2014–2022 at all of the sites, in the northeast cluster, respectively.

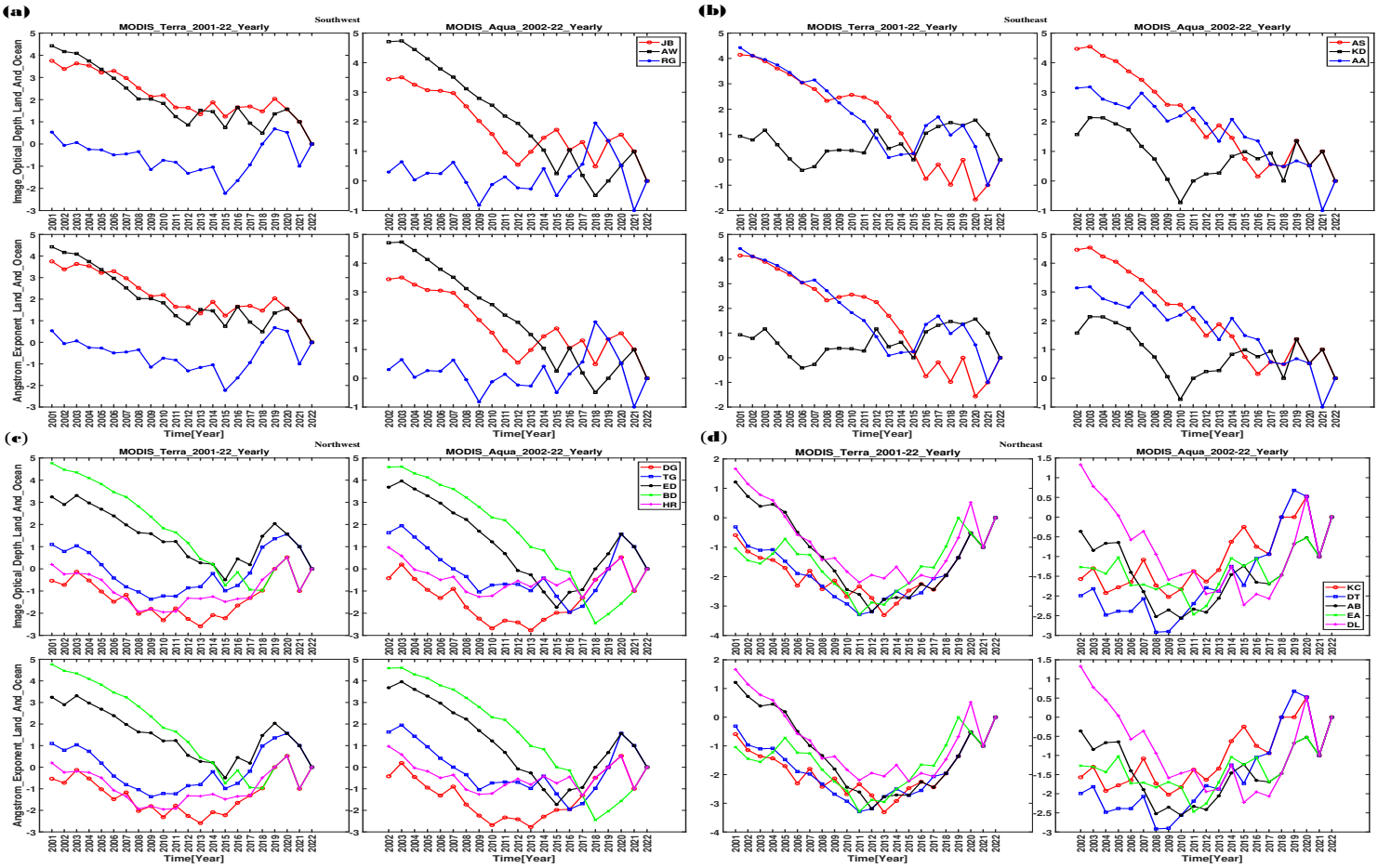

Figure 4.8: The Mann-Kendall rank backward statistic trends test.

Our results are consistent with previous results, with a small magnitude difference, for example: (Hansson et al., 2021) in the Pan-Arctic; (Habib et al., 2019) over the Asian desert; (Ali et al., 2020) in Pakistan; (Khan et al., 2021) over East China; (Wang et al., 2021) in Jiangsu Province of China; (Joshi et al., 2022) over the Central Himalayas; and (Xu et al., 2019) in the Yihe River in China, which show similar results to our findings but not exactly the same in magnitude. This result can be explained by the fact that the aerosol optical parameters AOD and AE are the columnar measures of the aerosol particles concentration and size distribution from the surface of the Earth to the atmosphere (Mohammad et al., 2022; Tian and Chen, 2010; Wu et al., 2012; Hansson

et al., 2021). Besides, the optical parameters AOD and AE are characterized by great complexity due to the different aerosol particles sources and the instant of the interactions among local, synoptic, and larger-scale circulations during the study periods and at the selected sites (Di Iorio et al., 2009; Feng et al., 2018; Bai et al., 2020).

4.3 Conclusions

The purpose of this study is to identify the dominant types and sizes of aerosol particles based on the temporal distribution variations of their optical parameters AOD and AE retrieved from the MODIS sensors over a period of 22 years (for Terra: January 2001 to December 2022, and for Aqua: July 2002 to December 2022). Those AOD and AE retrievals included the daily, monthly, seasonal, and yearly values at sixteen selected sites clustered in four regions with their corresponding averages. The main conclusions drawn from our work are as follows:

1. The minimum daily AOD (0.00 for both Terra, Aqua) and AE (0.67 for Terra, 0.87 for Aqua) were observed in the southeast cluster at the Kebri Dahar site, and the maximum AOD (1.02 for Terra, 0.97 for Aqua) and AE (1.18 for both Terra, Aqua) were in the northeast cluster at the Erta Ale site, both in Ethiopia.

2. The minimum monthly AOD (2.10 for Terra, 2.00 for Aqua) and AE (1.23 for both Terra, Aqua) were observed in the southeast cluster at the Kebri Dahar site, and the maximum AOD (0.85 for Terra, 0.81 for Aqua) and AE (1.17 for both Terra, Aqua) were in the northeast cluster at the Erta Ale site.

3. The minimum seasonal AOD (0.15 for Terra at Bega, 0.16 for Aqua at Belg) and AE (1.03 for both Terra at Bega, Aqua at Belg) were observed respectively in the southeast and northeast clusters at the Kebri Dahar and Kombolcha sites, and the maximum, in all sites in Kiremt season, AOD (0.86 for Terra, 0.84 for Aqua) and

AE (1.17 for both Terra, Aqua) were in the northeast cluster at the Erta Ale site, both belonging to Ethiopia.

4. The minimum yearly AOD (0.11 for Terra, 0.09 for Aqua) and AE (1.03 for Terra, 1.02 for Aqua) were observed in the southeast cluster at the Kebri Dahar site, and the maximum AOD (0.62 for Terra, 0.61 for Aqua) and AE (1.15 for both Terra, Aqua) were in the northeast cluster at the Erta Ale site. Hence, the minimum AOD and AE values were found at the Kebri Dahar site and the maximum at the Erta Ale site, respectively. In addition, the southeast cluster had the lowest AOD and AE values in both instruments, Terra and Aqua, while the northeast cluster had the highest.

The aerosol particle types have been classified by applying gaussian forms of the kernel density distribution techniques, and the Mann-Kendall rank trend test was applied over 16 sites in four classified clusters to check the annual variability of optical parameters of aerosol. The most dominant type of particle was maritime aerosol particles, with desert dust particles in second place. Aerosol particles were at their highest density in the northwest cluster at the Humera site during Bega and at their lowest levels mostly in the northeast cluster at the Juba site in the Kiremt season. The yearly total forward trend of aerosol particles was almost increasing, and the reverse was vice versa. The variations shown in the trend were lowest in the northwest cluster and highest in the northeast cluster.

Chapter 5

Long–Term Trend Analysis and Spatial Distribution of Aerosol Particles Over East Africa–Ethiopia Using MODIS Satellite Data

This chapter is to be cited as:

Alemu, A. A. and Raju, J. P.: Long–Term Trend Analysis and Spatial Distribution of Aerosol Particles Over East Africa–Ethiopia Using MODIS Satellite Data: Part 02, Journal of Heliyon, Elsevier, X, XXX–XXX, 2024.

5.1 Introduction

Among the most significant known global climate forcing factors, aerosols are microscopic solid-liquid mixtures of atmospheric particles with diameters ranging from 2 nm to 20 μm. They make up a tiny portion of the atmosphere (Khamala et al., 2022; Nourian et al., 2021). Primarily, the aerosol particles can be released from the Earth into the atmosphere through both natural and anthropogenic sources, which include biomass burning, incomplete combustion of fossil fuels, volcanic eruptions, wind-driven or traffic-related suspension of roads, soil and mineral dust, sea salt, sand, and biological materials (Chi et al., 2019; Gaffney et al., 2006b; Filioglou et al., 2020). In addition, some atmospheric

aerosol particles are also formed through the various physical and chemical processes in the atmosphere as their secondary sources (Behera, 2016; Li et al., 2015a; Huang et al., 2020). As a result, depending on their origins and further atmospheric processing, the aerosol particles types, compositions, and lifetimes vary in both temporally and spatially (Kafle and Coulter, 2013; Grythe, 2017). The aerosol particles optical properties, such as the aerosol optical depth AOD, which describes their concentration, and the Ångström exponent AE, which is related to the size distribution of aerosol particles, are used to observe the trend of distribution variation (Shafique et al., 2022; B AL-Taie et al., 2020; Kumar et al., 2015).

Therefore, this requires scientific observation to quantify the optical properties of the parameters. And hence, it is the right time to pay enough attention to air quality and the effects of climate change because it is a nightmare today. Such observation can be achieved using ground-based or satellite remote sensing technique that allows both spatial and temporal pattern and properties of aerosols to be assessed (Ngaina et al., 2014). According to a previous review of the literature, there is remarkably little research on atmospheric aerosol particles in the East African-Ethiopian region that makes use of satellite or ground-based data (Homa et al., 2017; Getachew, 2009; Eshet and Raju, 2022). There is no past literature survey on the long-term trends and spatial distributions using MODIS/Sunphotometer from countries like China, India, Africa, etc (Vaquero-Martínez and Antón, 2021). Therefore, in this study, we observed long-term trends of aerosol particles and their spatial distribution over East Africa-Ethiopia using the climatological database of AOD and AE from MODIS satellite instruments.

5.2 Results and Discussion

Using the formulas listed in our methodology subsection 3.6.1, we calculated the monthly AE raster averaged array values after extracting and gathering the spatial raster monthly

averaged AOD array values from January 1, 2001–December 31, 2022, using MODIS satellites. Next, we built the averaged seasonal and annual AOD and AE array values of the chosen study area regions. In this section, we discuss the seasonality and annual spatial distribution variation of aerosol particles and their corresponding long-term trends using the Mann-Kendall statistical rank test.

5.2.1 Spatial Distribution of Aerosol Concentration

Subsections 5.2.1 and 5.2.1 of the results and discussions section will present the seasonal and annual spatial distribution variations of the aerosol particles optical parameters AOD and AE over the study area regions.

Seasonal Distribution of Aerosol Concentration

This portion of the results and discussion is intended to address observations of the aerosol particles optical parameters AOD and AE spatial distribution and their seasonal fluctuations in the study area regions. Plotted for the selected study area regions, Figures 5.1(a–d) for both the Terra [left panels] and Aqua [right panels] instruments, with the AOD [above panels] and AE [lower panels], respectively, show the seasonal averaged spatial distribution variation of these parameters calculated from the study periods 2001–2022. The observed results indicate that the parameters are oriented towards the western part of the study area in general. This is consistent with the air pollution observations made in the study (Kalisa et al., 2023) over East Africa, where the parameters are mostly oriented towards the southwest of the study area regions, with $0.00 \leq \text{AOD} \leq 0.45$ and $0.95 \leq \text{AE} \leq 1.20$. Figure 5.1(a) shows the seasonality distribution variation, minimum AOD and AE values, and maximum values in the Kiremt season (Fig. 5.1(c)). The next season with the lowest AOD and AE values is the Belg season (Fig. 5.1(d)), while the next season with the highest values for the Kiremt season is the Tesday season (Fig. 5.1(b)) for both the Terra and Aqua instruments. While the results contradict the observations

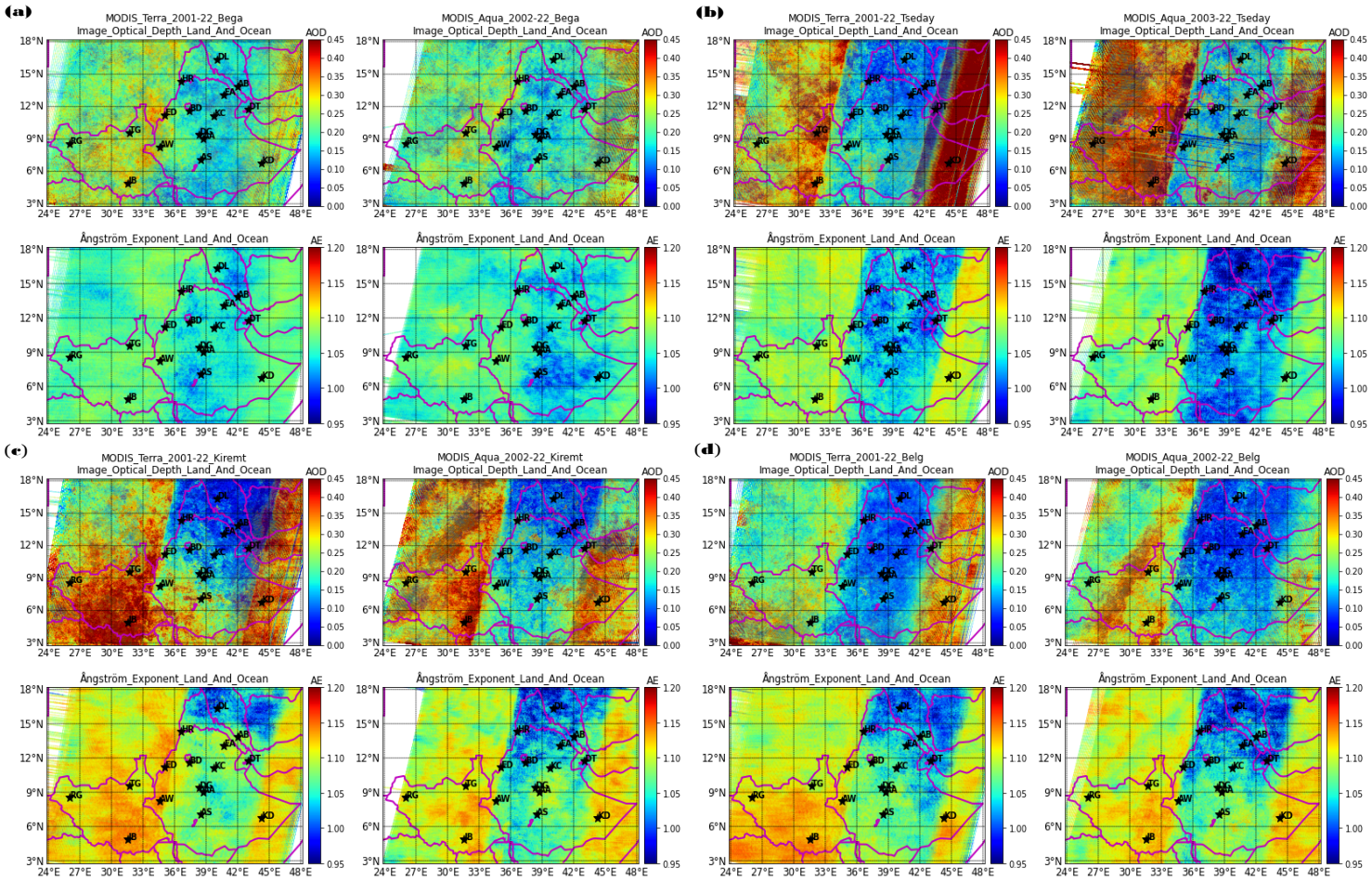

Figure 5.1: The aerosol optical parameters seasonal spatial variation.

of the studies at four selected sites (Addis Ababa, Debre Markos, and Debre Tabor in Ethiopia, and Djoubutti in Djibouti) (Homa et al., 2017; Eshet and Raju, 2022), they are similar to the findings of the studies from the Taklimakan desert in China (Li et al., 2021c) and the Nile River Basin in Ethiopia (Getachew et al., 2020). Contrary to the findings in (Kharol et al., 2011), higher values are observed from the Aqua instrument and lower values from the Terra instrument in the case of the instruments.

Although there are contradictory findings to our results, the studies conducted by various scholars we have discussed above and those in (Kalisa et al., 2023; Boiyo et al., 2018a; Torres-Delgado et al., 2021; Li et al., 2021c; Ngaina et al., 2014) about the seasonality of the aerosol particles optical parameters fluctuation, the different local activities, and the

long-range aerosol particles transport to the study area regions confirmed to be sufficient means of our observation aerosol sources. Therefore, we can generalize that the findings in our observations show that the aerosol particles optical parameter AOD and AE have seasonal minimums in the Bega season and maximums in the Kiremt season, and spatial minimums mostly in 33–42°E and maximums in the southwest of the study area regions, respectively.

Annual Distribution of Aerosol Concentration

This subsection provides an overview of the interannual fluctuations within each of the 22 years, as well as the total annual average spatial distribution variations of the aerosol

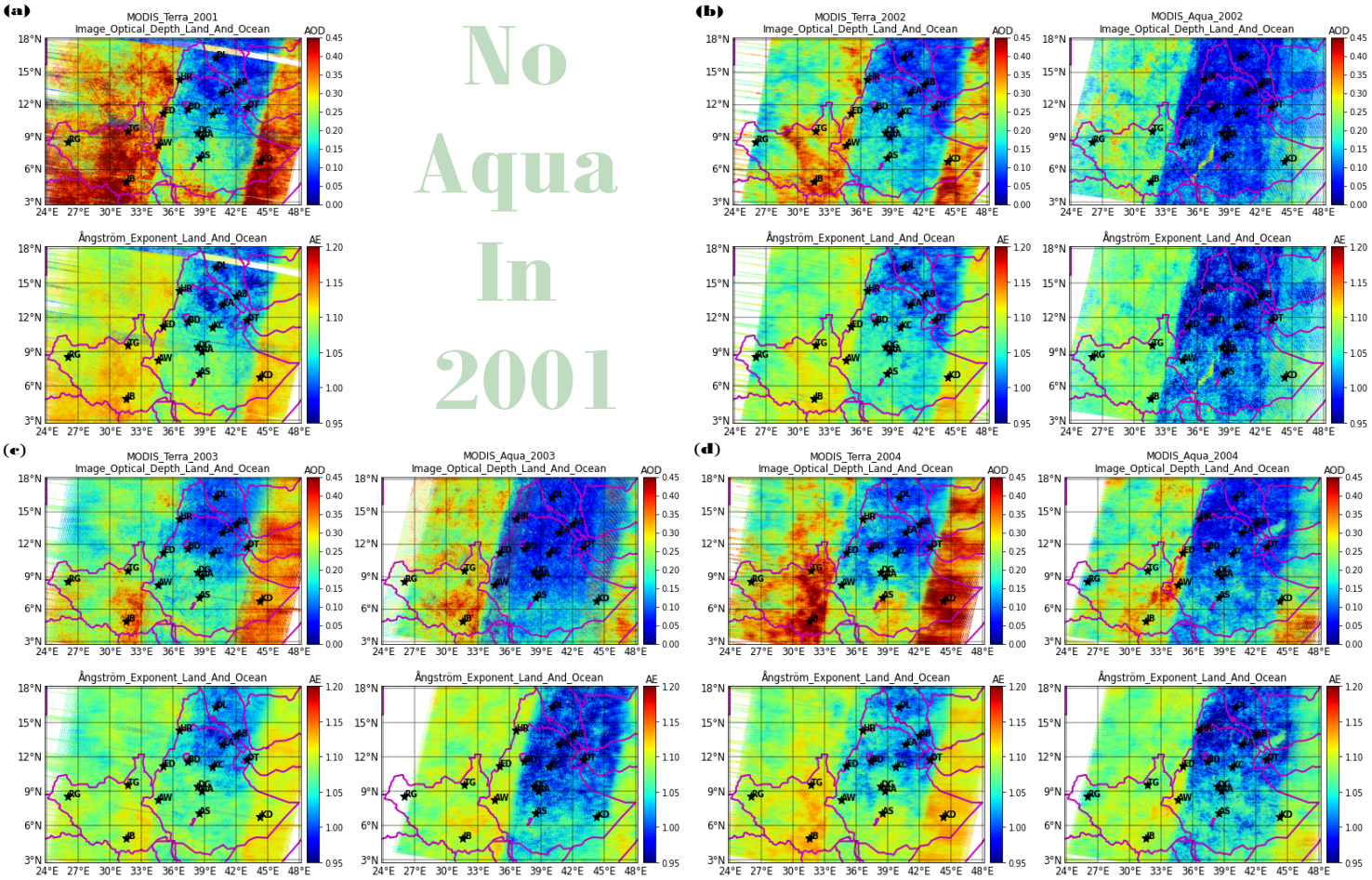

Figure 5.2: The aerosol optical parameters annual spatial variation [2001-2004].

particles optical parameters AOD and AE over the study area regions for the study periods of 2001–2022. Figures 5.2(a–d) for the years 2001–2004, Figures 5.3(a–d) for the years 2005–2008, Figures 5.4(a–d) for the years 2009–2012, Figures 5.5(a–d) for the study years 2013–2016, Figures 5.6(a–d) for the years 2017–2020, Figures 5.7(a–b) for the years of 2021–2022 and Figures 5.7(c) for their overall averages years of 2001–2022, respectively, show the results for both of the Terra [left panels] and Aqua [right panels] instruments with the AOD [above panels] and AE [lower panels] observations of the optical parameters we observed in this study work.

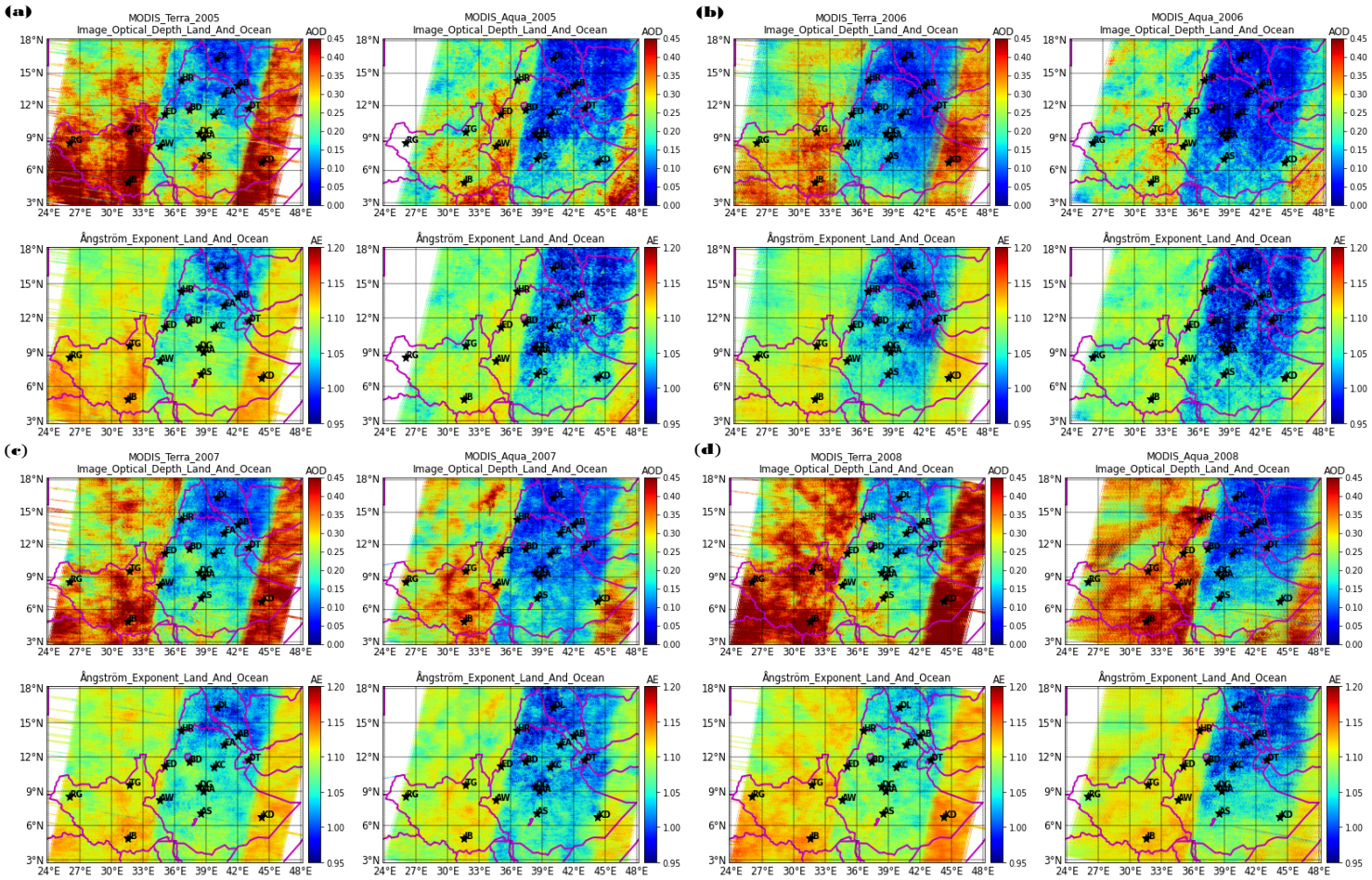

Figure 5.3: The aerosol optical parameters annual spatial variation [2005-2008].

As shown in the above figures, the results clearly show that the optical parameters are oriented towards the southwest and western regions in general. We can also observe the

interannual variability with frequent minimum and maximum values of AOD and AE optical parameters. The optical parameters also had minimums in the years 2001 (Fig. 5.2(a)), 2002–2003 (Fig. 5.2(b–c)), 2008 (Fig. 5.3(d)), and 2015 (Fig. 5.5(c)). The

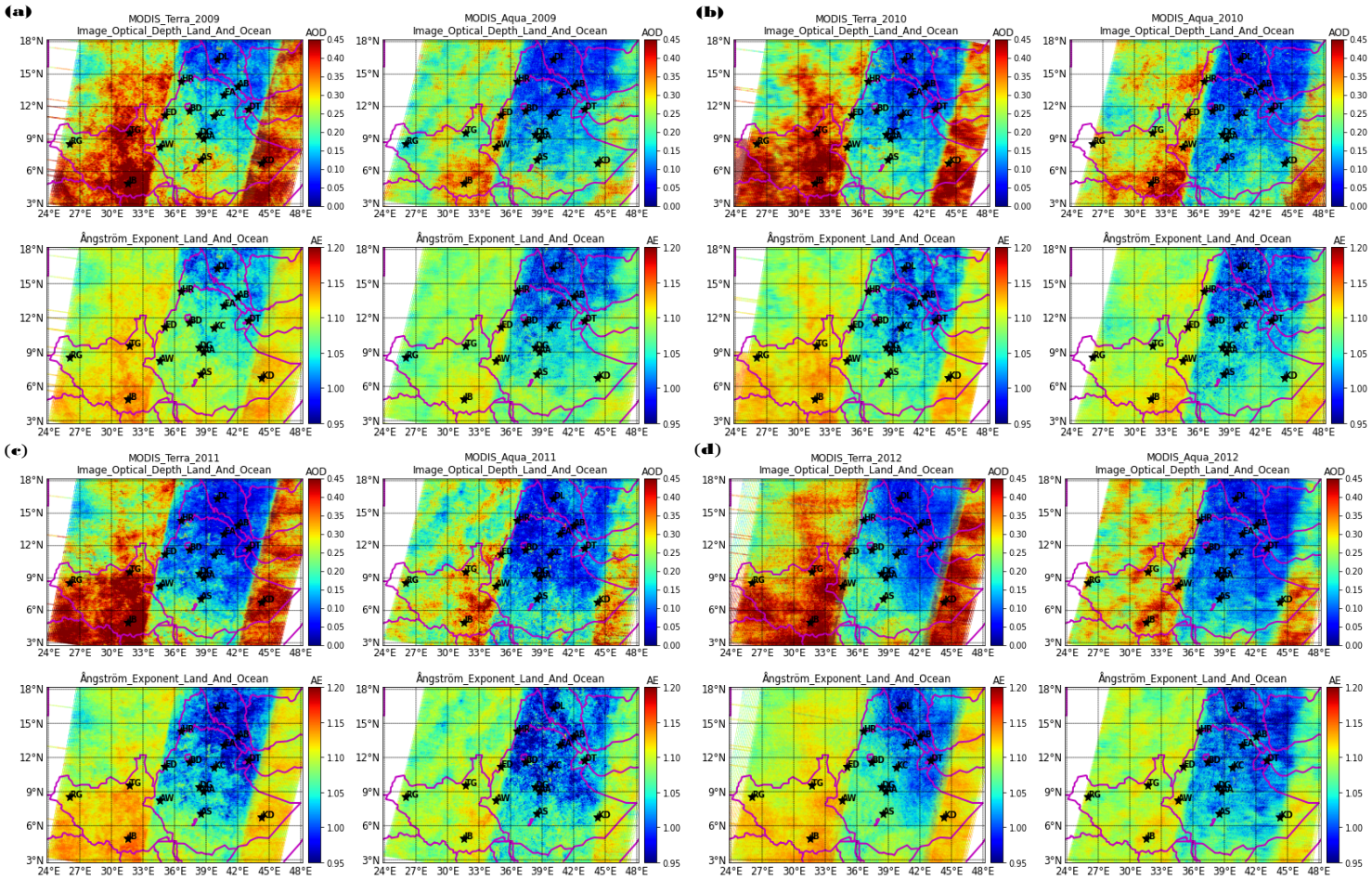

Figure 5.4: The aerosol optical parameters annual spatial variation [2009-2012].

results on the aerosol particles optical parameters and interannual temporal variations in the upper Blue Nile basin show the minimums are in the year 2004 and the maximums are in the year 2011. However, there is no exact or nearly similar research to compare our observation with others (Getachew et al., 2020). While the instrumental variation values show the opposite with the seasonal and interannual data, the overall findings of the total average spatial distribution variation shown in Figure 5.7(c)) and its regional minimums and maximums agree with the observations we see in the individual 22 years. Stated

differently, the Aqua instrument exhibits relatively higher optical parameter values than the Terra instrument.

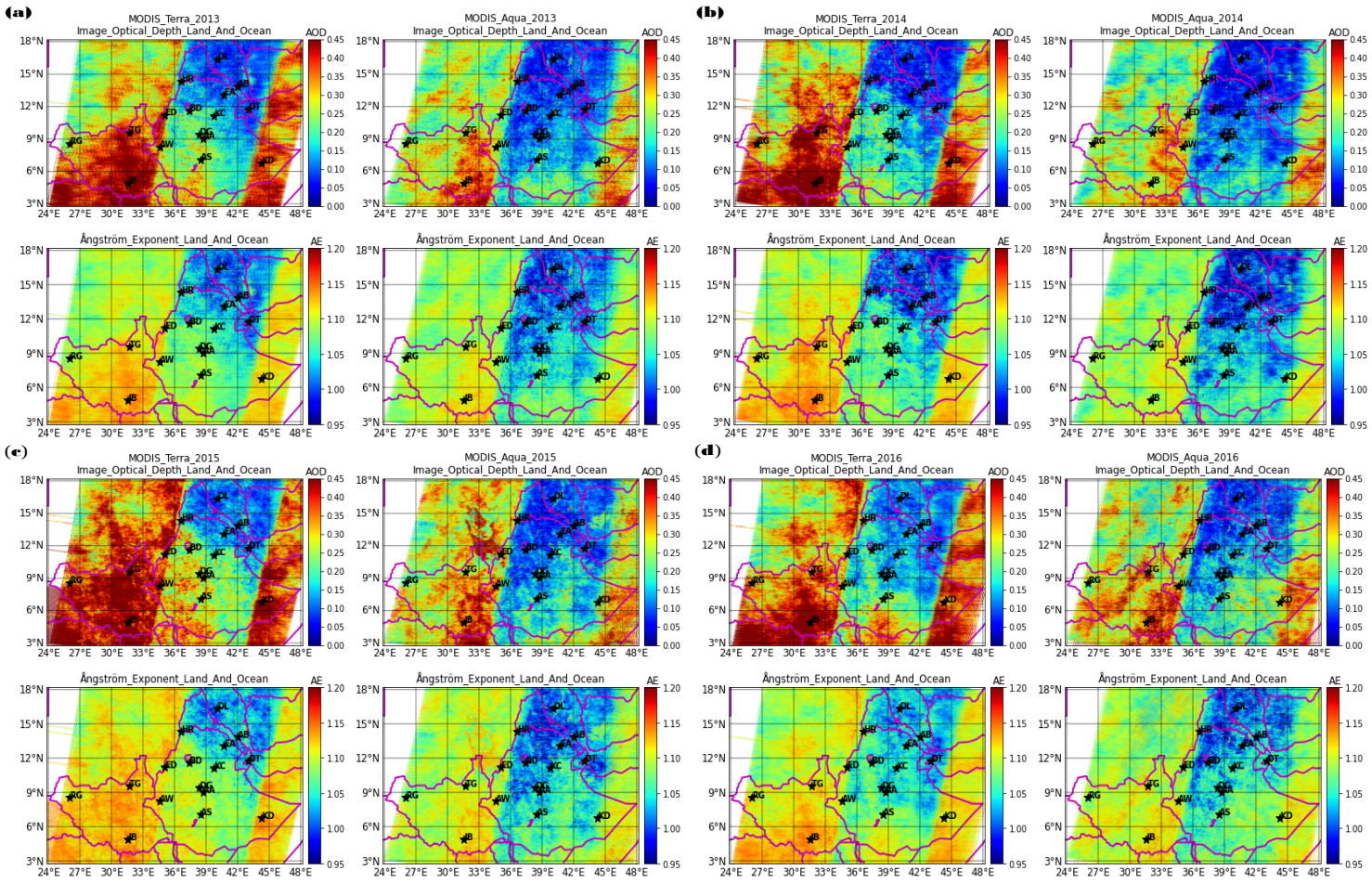

Figure 5.5: The aerosol optical parameters annual spatial variation [2013-2016].

5.2.2 Spatial Trend Analysis of Aerosol Concentration

In the following subsections 5.2.2 and 5.2.2 of the results and discussions section, the seasonal and annual spatial distribution trend variations of the aerosol particles optical parameters AOD and AE over the study area regions are presented.

Seasonal Trend Analysis of Aerosol Concentration

The seasonal spatial trend tests for the aerosol particle optical parameters over the study area regions are described in this subsection. We hvae used the Sen's slope method, which is explained in methodology section 3.6.3, to apply the Mann-Kendall rank forward statistical trend tests to the spatially distributed seasonal AOD and AE values. The results of these techniques are shown in Figures 3(a)–(d) for both the Terra [left panels] and Aqua [right panels] instruments, with the parameters that range being -15.0≤AOD≤15.0 [above panels] and 0.95≤AE≤1.40 [lower panels], respectively.

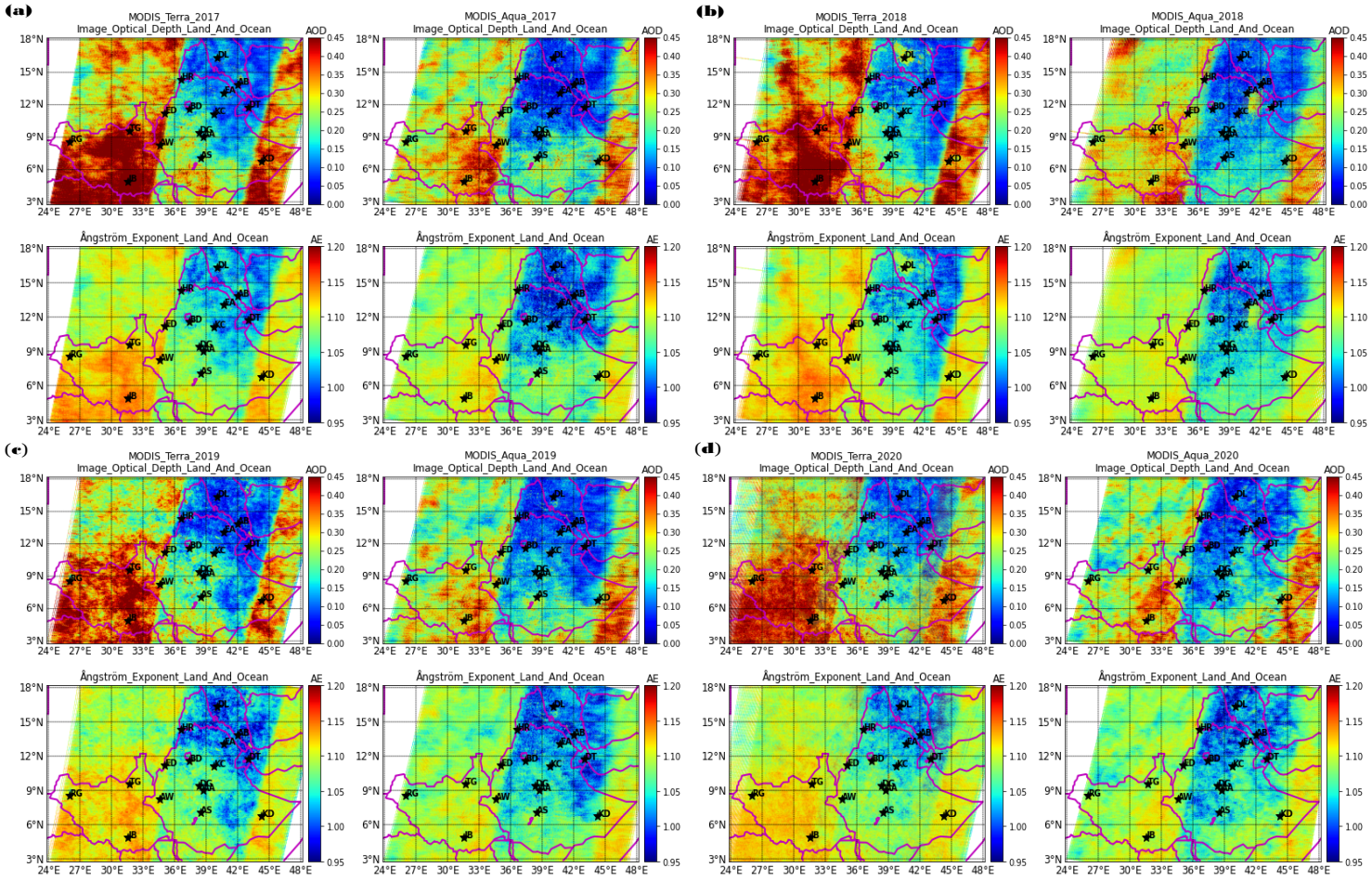

Figure 5.6: The aerosol optical parameters annual spatial variation [2017-2020].

Across the research work regions, the forward spatial trends generally exhibit complex distribution variations and are positive, with minimums in the Belg season (Fig. 5.8(d))

and maximums in the Kiremt season (Fig. 5.8(c)). With the exception of the Bega and Tseday seasons (Fig. 5.8(a-b) right panels), whose minimums are in the southeast and maximums are nearly throughout the remaining regions of the study area for the Terra instrument, they are high in the southern regions and low in the northern regions. Furthermore, for the Aqua instrument, the trend is comparatively stronger in the Bega and Tseday seasons, and for the Terra instrument, it is stronger in the Kiremt and Belg seasons. Since the AOD and AE distributions have distinct sources and instantaneous interactions with local, synoptic and larger-scale circulations in the study periods and regions, the observed complexity of trends may be caused by these factors, as discussed in (Di Iorio et al., 2009; Feng et al., 2018; Bai et al., 2020).

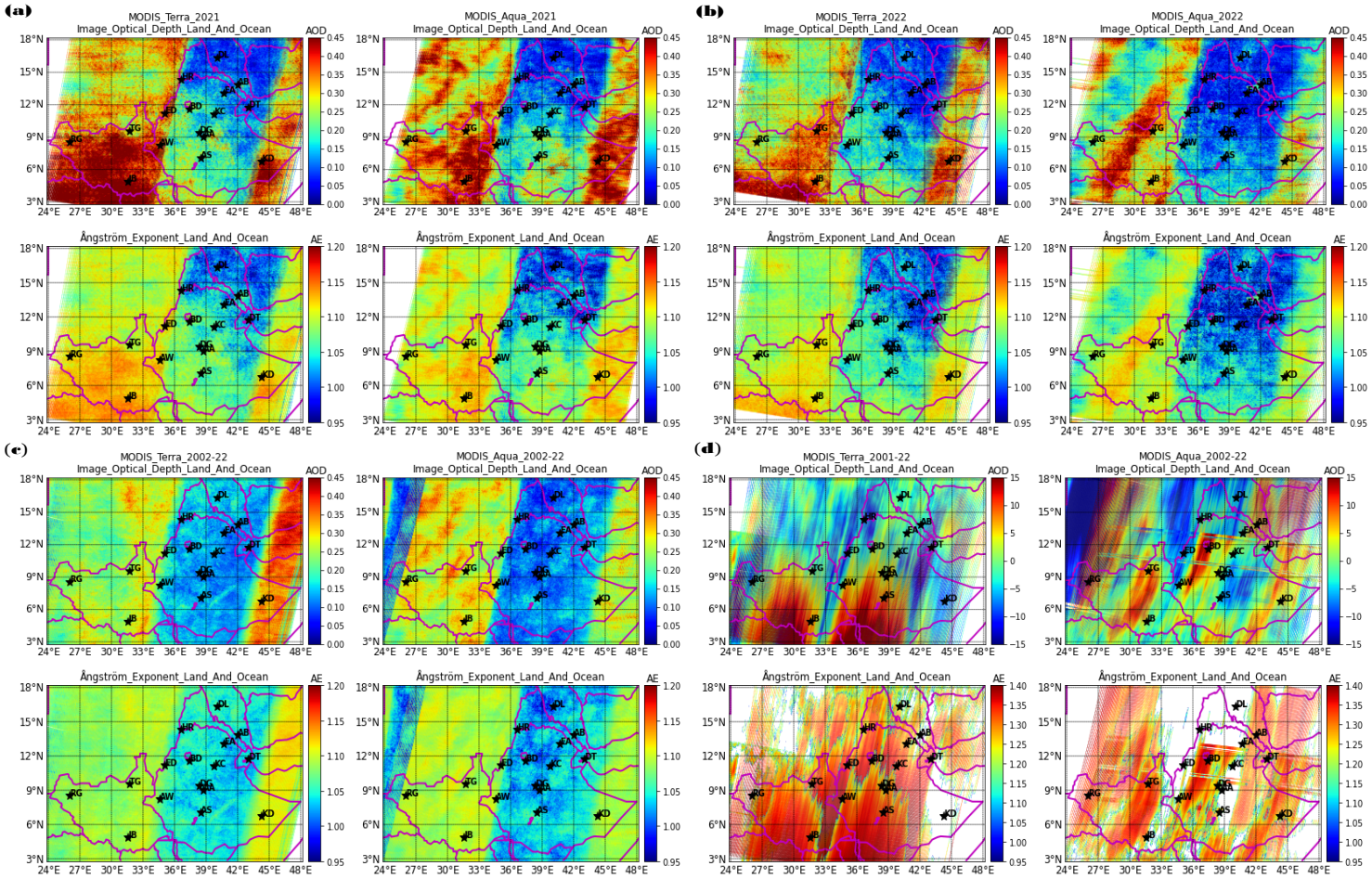

Figure 5.7: The aerosol optical parameters yearly spatial variation.

The study area regions' tropical atmospheric conditions, which include increased biomass burning, in conjunction with the prevailing meteorological conditions, may be the cause of the observed positive trends. Conversely, decreased biomass burning and altered land-use patterns may be the cause of the declining trend in these areas (Boiyo et al., 2018b, 2019).

Annual Trend Analysis of Aerosol Concentration

The annual statistical trend tests for the optical parameters of aerosol particles over the study areas are described in this subsection. Figures 5.8(d) show the 22-year total averaged annual Mann-Kendall statistical trends with the AOD [upper panels] and AE

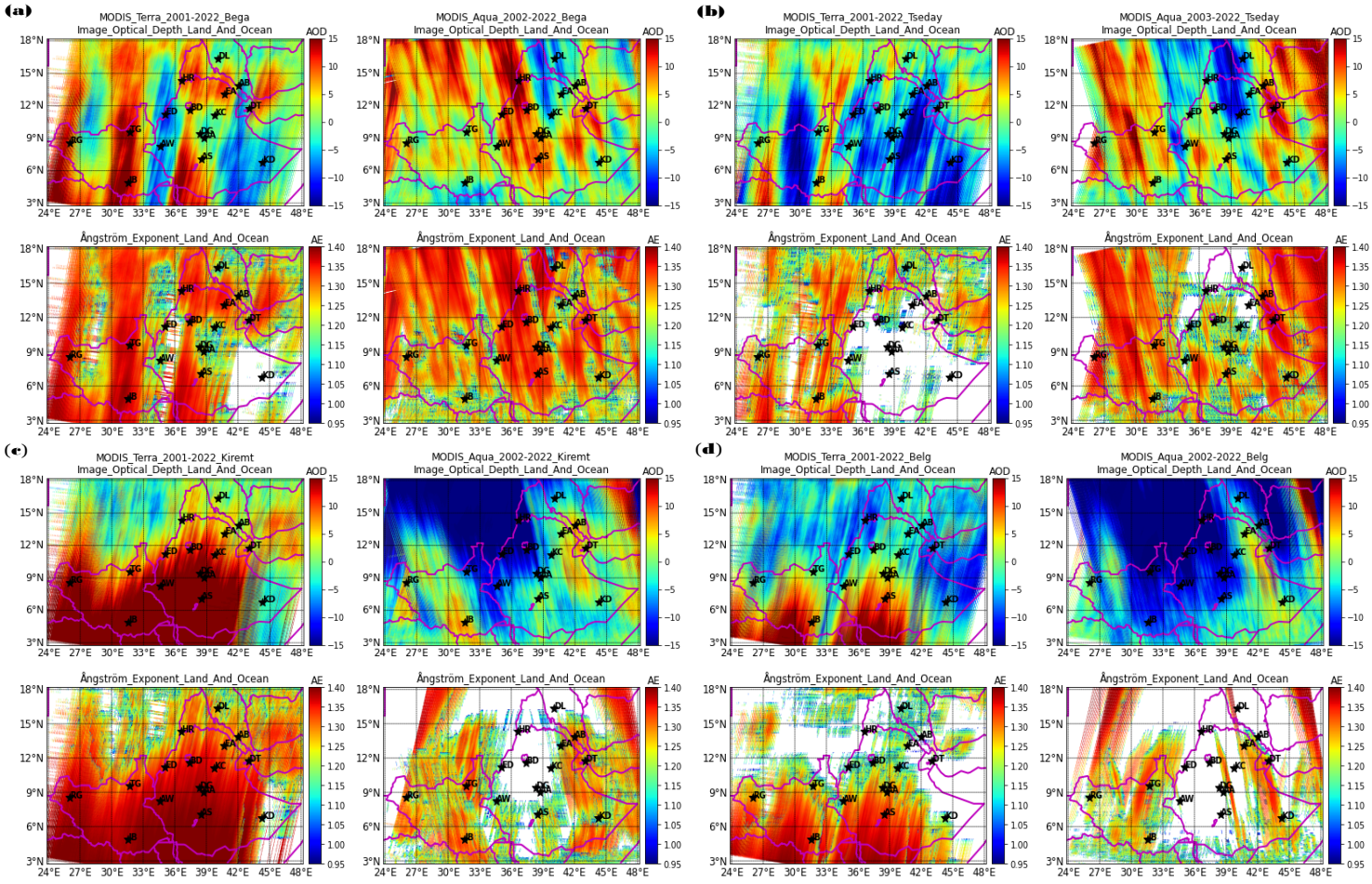

Figure 5.8: The Mann-Kendall rank forward statistic seasonal trends test.

[lower panels] for both the Terra [left panels] and Aqua[right panels]. From those figures,

we observe that there is a slightly increasing forward trend variation distribution towards the southern part of the study area regions. The total averaged annual spatial variation has minimum trends in the north and maximum trends in the south. Relatively, the trend is more for the Terra satellite than the Aqua, with almost no AE trend in the southeast region. Here, the statistical trend tests confirm the significance of the positively increasing aerosol particles concentration and size during the study period. This discrepancy can be explained by the fact that the optical parameters AOD and AE are the columnar measures of the aerosol particle concentration and size distribution from the surface of the Earth to the atmosphere (Mohammad et al., 2022; Tian and Chen, 2010; Wu et al., 2012; Hansson et al., 2021; Makokha et al., 2017b).

Our findings are in agreement with previously conducted temporal trend distribution variations, albeit with differences in magnitude. For instance, Hansson et al., 2021; Habib et al., 2019; Ali et al., 2020; Khan et al., 2021; Wang et al., 2021; Joshi et al., 2022; and Xu et al., 2019; over the Asian desert; Pan-Arctic; Jiangsu Province of China; and Hanson et al., 2021; exhibit results that are similar to ours, albeit not precisely the same in magnitude.

5.3 Conclusions

The aim of this research is to examine the spatial distribution fluctuations and long-term trends of aerosol particles using the optical parameters AOD and AE that were obtained from the active MODIS sensors over a 22-year period (January 2001 to December 2022 for Terra and July 2002 to December 2022 for Aqua). The seasonal, interannual, and total annual average spatial distributions, as well as statistical trend tests for value variation in the selected study area regions and periods, were included in those AOD and AE optical parameter retrievals. The conclusions are drawn as follows:

1. The optical parameters AOD and AE generally exhibit minimum distribution values during the Bega and Belg seasons and maximums during the Kiremt and Tseday seasons in the seasonal spatial distribution.

2. The optical parameters AOD and AE demonstrate the lowest distribution values in the years 2002–2003, with maximums in 2001, 2008, and 2015 in interannual spatial distribution fluctuations.

3. In general, we can state that the optical parameters are oriented primarily southwest and more westward, respectively, with maximums in the southwest of the study area regions and minimums in the 33–42°E region.

4. In the overall averaged annual distributions, more values are observed in the Aqua than in the Terra. However, for the seasonal and interannual spatial distributions, higher AOD and AE values are observed in the spatial distribution variations from the Terra and less from the Aqua.

5. The significance of the positively increasing aerosol particles concentrations and the sizes during the study periods is confirmed by the Mann-Kendall rank forward trend tests.

The optical parameters spatial distribution variations show minimum values during the seasons and places where the particles scavenge and maximum values during the seasons and places where the aerosol particles become more concentrated due to local activities and long-scale transportation to the study area regions. Furthermore, the spatial trends show positive increases and negative decreases in the study area regions and the seasons attributed to changes in climatic conditions and anthropogenic activities. Based on these findings, we can conclude that the aerosols optical parameters are widely variable as a result of the variability in seasonality, meteorological conditions, and emission sources.

Chapter 6

Effects of Aerosol Particles on Precipitation and Cloud Parameters Over East Africa-Ethiopia Using MODIS Satellite Data

The Chapter is to be cited as:

Alemu, A. A. and Raju, J. P.: Effects of Aerosol Particles on Precipitation and Cloud Parameters Over East Africa-Ethiopia Using MODIS Satellite Data: Part 01, Journal of Quantitative Spectroscopy & Radiative Transfer JQSRT, Elsevier, 17(1), 029–056, 2024.

6.1 Introduction

Our atmosphere is an ever-changing system that keeps the Earth inhabitable by absorbing shortwave radiation and re-emitting long-wave radiation. The atmosphere contains gases, aerosol particles, and collections of liquid and solid hygrometers that make up clouds. Atmospheric aerosols are small mixtures of both solid particles and liquid droplets of particulate matter suspended in the atmosphere (Kafle and Coulter, 2013; Grythe, 2017). Their size ranges from a few tens of nanometers to several tens of micrometers. Which is to say, they are in between the width of the smallest viruses and the diameter of human hair, barely visible to the human eye, with lifetimes ranging from hours to years. These

compositions, sizes, and lifetimes of the aerosol particles affect how far they can travel around the world, their interactions with precipitation, clouds, and radiation budgets, and their total potential effects on climate and human health (Duffney et al., 2023; Mushtaq et al., 2022; Okuda, 2013).

The aerosol particles-cloud parameters-precipitation interactions attract more attention, so regional as well as global scientific observations are needed to qualify and confirm the situations. From a previous literature review, we found that there are few studies on atmospheric aerosol particles optical properties in East Africa–Ethiopia using ground or satellite data (Homa et al., 2017; Getachew, 2009; Eshet and Raju, 2022). However, to date, no one has reported the effects of aerosol particles on cloud parameters, precipitation, and the radiation budget using satellite data from the Moderate Resolution Imaging Spectroradiometer MODIS, Tropical Rainfall Measuring Mission TRMM, and Clouds and the Earth‘s Radiant Energy System CERES.

Hence, in this study, we used the climatological database of the aerosol particles optical properties, namely the aerosol optical depth AOD and Ångström Exponent AET (Tomasi and Lupi, 2017; B AL-Taie et al., 2020; Kumar et al., 2015), and the cloud parameters such as atmospheric water vapor AWV, mean cloud fraction CFM, cloud top pressure CTP, and cloud top temperature CTT (Sporre, 2016; Barthlott and Hoose, 2018) from MODIS, the precipitation PPT (Barnsley, 1999; Liu et al., 2023) from TRMM, and the out going long-wave radiation OLR flux (Myhre et al., 2013; Lippmann, 2000) from CERES satellite instruments, to identify the interactions over East Africa-Ethiopia.

6.2 Results and Discussion

After extracting the HDF datasets and collecting their spatial raster AOD, AWV, CFM, CTP, and CTT array values from MODIS, PPT array values from TRMM, and OLR array values from CERES during January 2001–December 2022, the AET values were

calculated from the AOD values using the formula described in the methodology section 3.6.1. And then monthly, seasonal and yearly temporal averages were obtained for selected sites clustered into four regions, i.e., southwest, southeast, northwest, and northeast of the study area. In addition, we also discuss the PCA-explained variance and fire-map trajectory model analysis in this section.

6.2.1 Spatial Variation of Aerosol Influence

In this section, respectively from right to left, Bega, Tseday, Kiremt, Belg, and Annual, we presented the seasonal as well as the total annual average spatial distribution variations for the study periods 2001–2022. The spatial distribution fluctuations of the parameters

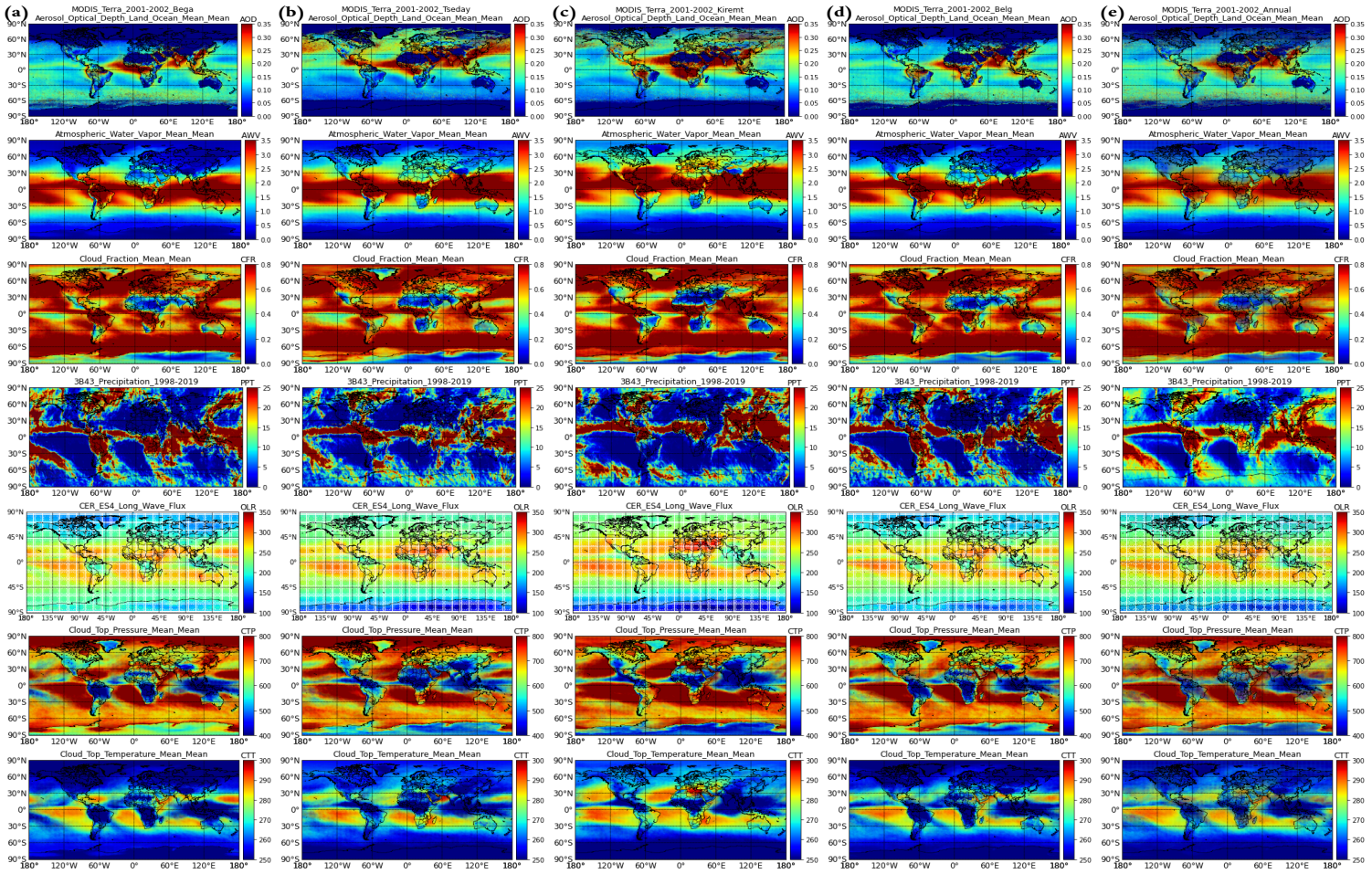

Figure 6.1: The aerosol optical parameters spatial distribution [Terra].

we observed in these research findings are shown using Figures 6.1 and 6.2 for the Terra and Aqua satellite data, respectively. Our observations include the research findings that contain: for the aerosol particles optical parameters $0.00 \leq AOD \leq 0.35$ (1^{st} upper panels); for the cloud parameters $0.00 \leq AWV \leq 3.50$ (2^{nd} panels), $0.00 \leq CFM \leq 0.80$ (3^{rd} panels), $400.00 \leq CTP \leq 800.00$ (6^{th} panels), and $2500.00 \leq CTT \leq 300.00$ (lower panels); for the precipitation values $0.00 \leq PPT \leq 25.00$ (only in Terra 4^{th} panels); and for the outgoing long-wave radiation flux $100.00 \leq OLR \leq 350.00$ (5^{th} panels) over the globe we take the study area {3–18^0 N, 24–48^0 E} regions with in it.

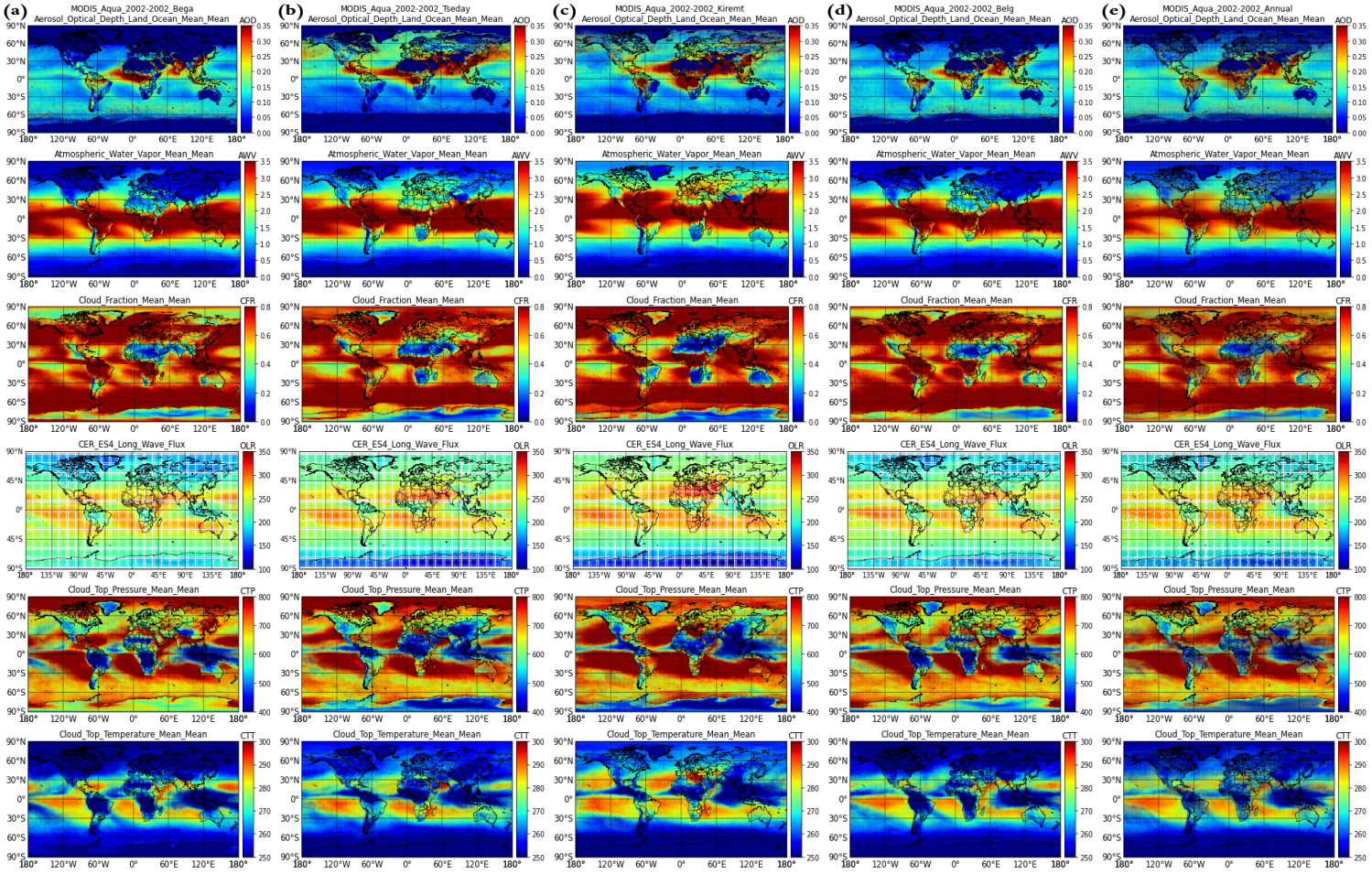

Figure 6.2: The aerosol optical parameters spatial distribution [Aqua].

From both the seasonality and total annual results, we can observe that the parameters are generally oriented towards the western part of the study area regions, mostly in the

southwest of the study area regions. The seasonality distribution variation shows that the minimum values are found in the Bega season (1st column panels) and the maximum values are in the Kiremt season (3rd column panels). The Belg season (4th column panels) is the next to have minimum values, while the next maximum values for the Kiremt season are in the Tesday season (2nd column panels) for both the Terra and Aqua instruments. The results are similar to the findings of the studies from the Taklimakan desert in China (Li et al., 2021c) and the Nile River Basin in Ethiopia (Getachew et al., 2020) while they contradict the observations of the studies at four selected sites: Addis Ababa, Debre Markos, and Debre Tabor in Ethiopia, and Djibouti in Djibouti (Homa et al., 2017; Eshet and Raju, 2022). In the case of the instruments, greater values are observed from the Aqua instrument and less from the Terra instrument, which contradicts the observations in (Kharol et al., 2011).

So, we can generalize that the findings in our observations show that the parameters have seasonal minimums in the Bega season and maximums in the Kiremt season, and spatial minimums mostly in 33–42°E and maximums in the southwest of the study area regions, respectively. And the parameters are higher on the Terra instrument relative to the Aqua instrument. Even if there are also contradictory findings to our results, the studies undergone by different scholars we discussed above and those in (Kalisa et al., 2023; Boiyo et al., 2018a; Torres-Delgado et al., 2021; Li et al., 2021c; Ngaina et al., 2014) about the seasonality of the parameters fluctuation, the different local activities, and the long–range aerosol particles transport to the study area regions confirmed our observation.

6.2.2 Monthly Variation of Aerosol Influence

This section of the study depicts the results of the total average monthly temporal value fluctuations for the aerosol particles, cloud parameters, precipitation, and the outgoing long-wave radiation flux we described before. The temporal monthly mean values of the

parameters are constructed for each site in the four clustered regions. The results of our observations for the parameters values variations are illustrated in Figures 6.3 and 6.4 for the Terra and Aqua satellite data, respectively. The increase and decrease fluctuations for the parameters AWV, CFM and PPT are with AOD, while for OLR, CTP and CTT they are vice-versa!

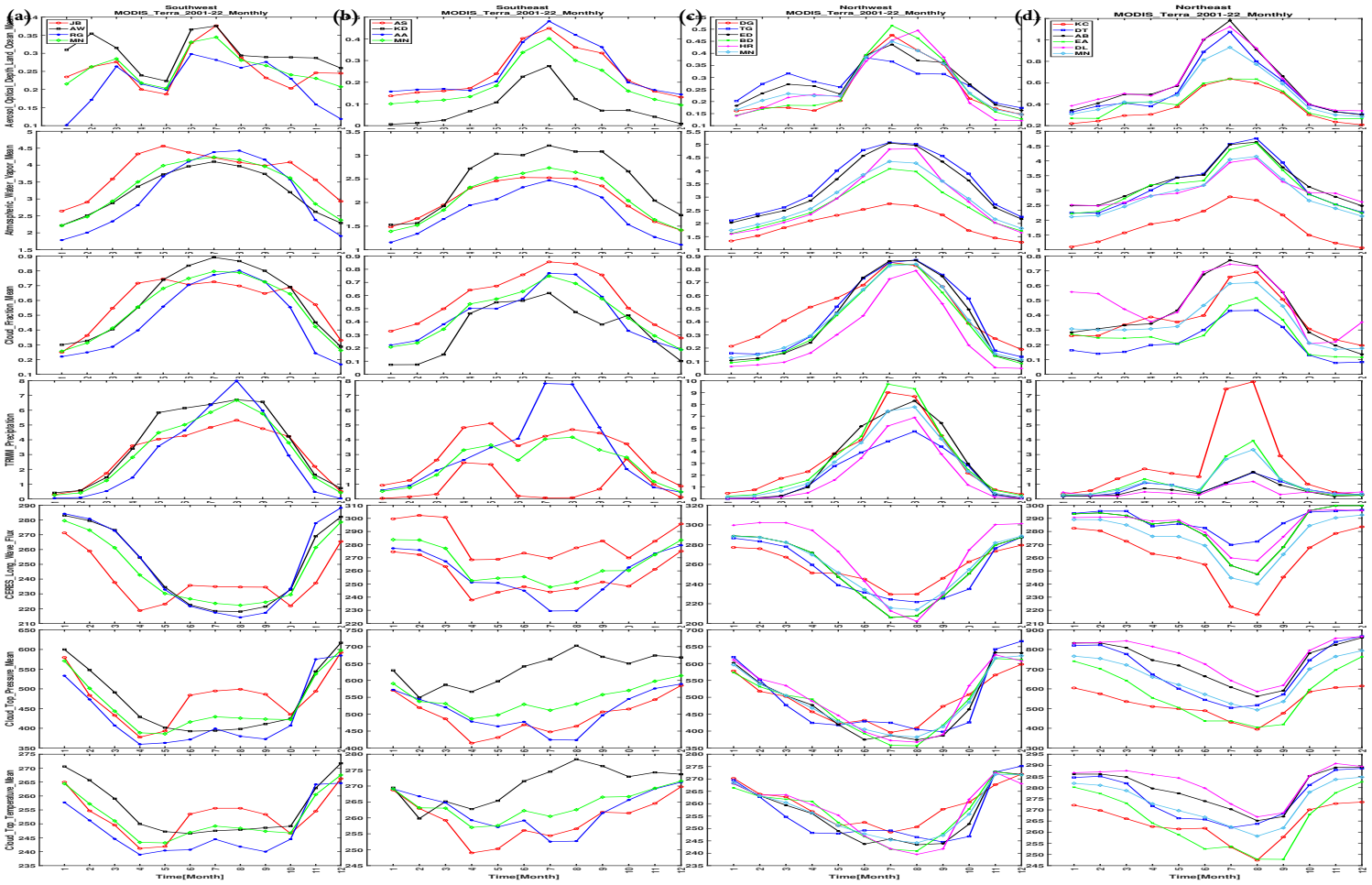

Figure 6.3: The aerosol optical parameters monthly variation [Terra].

In the southwest cluster (1st column panels), the minimum values for the parameters are observed in South Sudan at the Raga site, while the maximum values are observed in Ethiopia at the Agnuak site for AOD, CFM, CTP, and CTT; in South Sudan at the Juba site for AWV; and at the Raga site for PPT and OLR. For the southeast cluster (2nd column panels), the minimum values are observed in Ethiopia at the Kebri Dahar

site AOD, CFM, and PPT. The other minimas in Ethiopia are at the Addis Ababa site for AWV, OLR, CTP, and CTT. And the maximum values are observed in Ethiopia at the Addis Ababa site for AOD and PPT, and still in Ethiopia at the Kebri Dahar site for AWV, OLR, CTP, and CTT. Another maximum value is observed in Eritrea at the Aseb site for CFM. Here, the results we observed and discussed in the southern clustered regions are from both the Terra and Aqua satellite instruments.

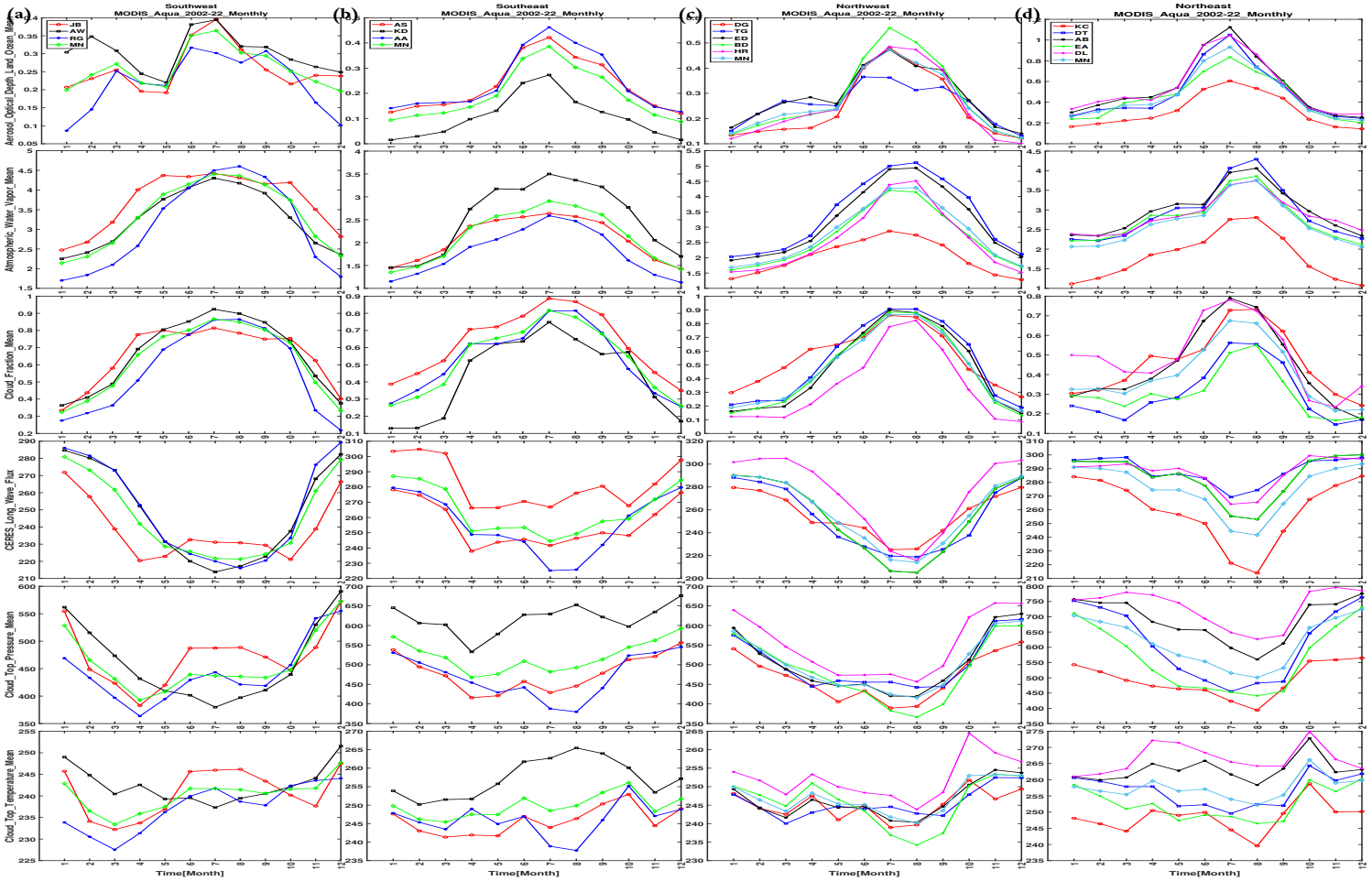

Figure 6.4: The aerosol optical parameters monthly variation [Aqua].

In the northwest cluster (3rd column panels), the minimum values for the parameters are observed in Ethiopian at the Humera site for AOD, CFM, PPT, OLR, and CTT. The other minima in Ethiopia are at the Dangote sites for AWV and at the Bahir Dar site for CPT. And the maximum values for the parameters are observed in Ethiopia at the Bahir

Dar site for AOD and PPT and at the Humera sites for OLR. The other maxima values for the parameters are observed in South Sudat at the Tonga site for AWV, CFM,CPT, and CTT. When we moved to the northeast cluster (4^{th} column panels), the minimum values for the parameters were observed in Ethiopia at the Kombolcha site for AOD, AWV, OLR, CTP, and CTT. The other minimum values for the parameters were observed in Djibouti at the Djibouti site for CFM and in Eritrea at the Dahlak site for PPT. And the maximum values for the parameters are observed in Eritrea at the Aseb site for AOD and CFM and at the Dahlak site for CPT and CTT. The other maximum values for the parameters are observed in Djibouti at the Djibouti site for AWV and OLR, and also in Ethiopia at the Kombolcha site for PPT. Here, the results we observed and discussed in the northern clustered regions are from both the Terra and Aqua satellite instruments, with some exceptions. Minimum values for the parameters are observed for OLR at the Bahir Dar and the Ethiopian Renascence Dam sites, and maximum values for CTP and CTT at the Tonga site in the Aqua satellite.

In general, for both of the Terra and Aqua instruments: the minimum values are found at the Kebri Dahar site for AOD, at the Kombolcha site for AWV, at the Humera site for both CFM and PPT, they all in January and December, while their maximum values are AOD at the Aseb siet, AWV at the Tonga site, CFM at the Agnuak sie, and PPT at the Bahir Dar site, they all in July; the minimum values were found for OLR at the Humera site and CTP at the Bahir Dar site both in August and CTT at the Raga site in March and April, while the maximum OLR value is at the Kebri Dahar site in February; the maximum CTP value is at the Dahlak site in January and December; the maximum CTT value is at the Dahlak site in November. Exceptionally, the minimum values for the OLR are at the Bahir Dar and Ethiopian Renascence Dam sites in July and August for the Terra and Aqua instruments, respectively.

6.2.3 Seasonal Variation of Aerosol Influence

The seasonal variations of the parameters at the selected sites clustered into four areas are addressed in this section. The evolution of these parameters estimated from the study periods of 2001–2022 are shown respectively in Figures 6.5 and 6.6 for the Terra and Aqua satellite data together with their corresponding total average means. The minimum values for the parameters AOD, AWV, CFM, and PPT are found in the Bega season, and their maximum values are found in the Kiremt season, while the minimum values for the parameters OLR, CTP and CTT are found in the Kiremt season, and their maximum values are found in the Bega season, which are in vice-versa in all of the clusters and both of the instruments.

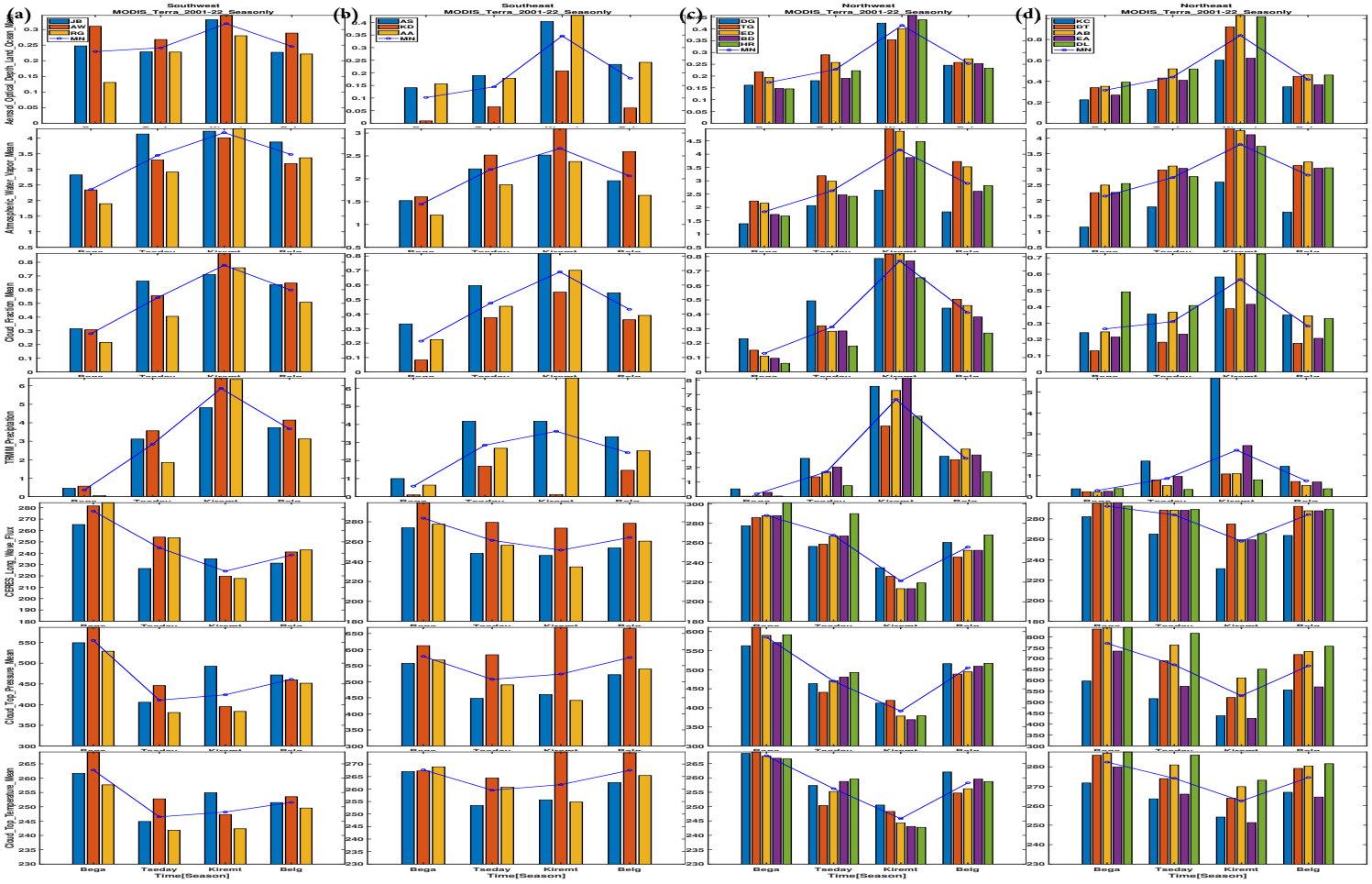

Figure 6.5: The aerosol optical parameters seasonal variation [Terra].

In the southwest cluster (1st column panels), the minimum values for the parameters are observed in South Sudan at the Raga site, while the maximum values are observed in Ethiopia at the Agnuak site for AOD, CFM, PPT, CTP, and CTT; in South Sudan at the Raga site for the parameters AWV and OLR. For the southeast cluster (2nd column

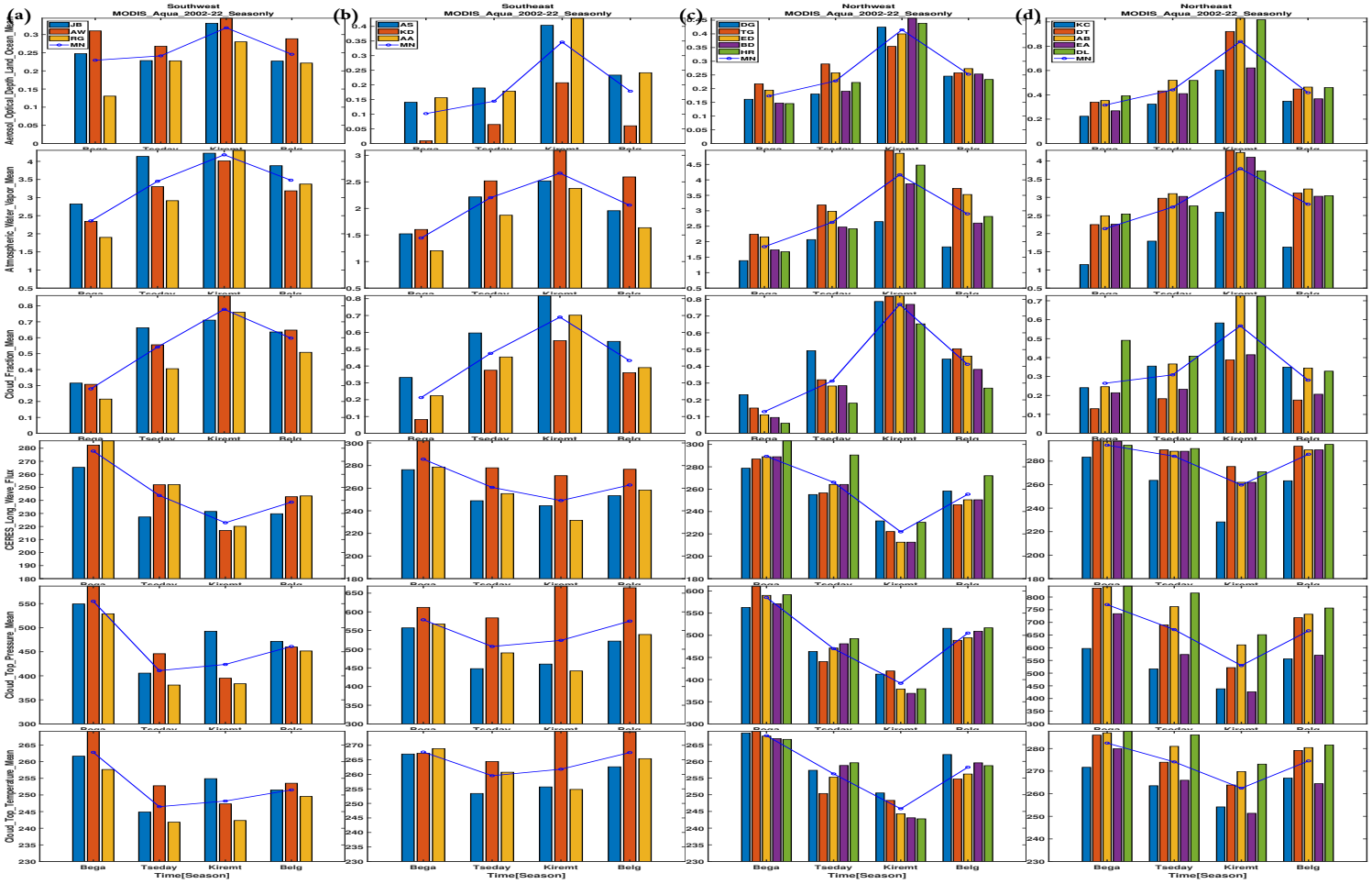

Figure 6.6: The aerosol optical parameters seasonal variation [Aqua].

panels), the minimum values are observed in Ethiopia at the Kebri Dahar site AOD, CFM, and PPT. The other minimas in Ethiopia are at the Addis Ababa site for AWV and OLR, and in Eritrea they are at the Aseb site for CTP and CTT. And the maximum values are observed in Ethiopia at the Addis Ababa site for AOD and PPT, and still in Ethiopia at the Kebri Dahar site for AWV, OLR, CTP, and CTT. Another maximum value is observed in Eritrea at the Aseb site for CFM. Here, the results we observed and

discussed in the southern clustered regions are from both the Terra and Aqua satellite instruments.

In the northwest cluster (3rd column panels), the minimum values for the parameters are observed in Ethiopia at the Humera site for AOD and CFM and at the Ethiopia Renascence Dam site for CTT. The other minima in Ethiopia are at the Dangote sites for AWV and at the Bahir Dar site for OLR and CPT. And the maximum values for the parameters are observed in Ethiopia at the Bahir Dar site for AOD and PPT and at the Humera sites for OLR and CTT. The other maxima values for the parameters are observed in South Sudan at the Tonga site for AWV, CFM, and CPT. When we moved to the northeast cluster (4th column panels), the minimum values for the parameters were observed in Ethiopia at the Kombolcha site for AOD and AWV and at the Erta Ale site for CTP and CTT. The other minimum values for the parameters were observed in Djibouti at the Djibouti site for CFM and in Eritrea at the Aseb site for PPT and OLR. And the maximum values for the parameters are observed in Eritrea at the Aseb site for AOD and CTP and at the Dahlak site for CFM and CTT. The other maximum values for the parameters are observed in Djibouti at the Djibouti site for AWV. Still, other values are also observed in Ethiopia at the Kombolcha site for PPT and at the Erta Ale site for OLR. Here, the results we observed and discussed in the northern clustered regions are from both the Terra and Aqua satellite instruments, with some exceptions. Minimum values for the parameters are observed for OLR, CTP and CTT at the Kombolcha and the Ethiopian Renascence Dam sites, and maximum values for CTP and CTT at the Tonga site in the Aqua satellite.

In general, for both of the Terra and Aqua instruments: the minimum values are found at the Kebri Dahar site for ADD, at the Kombolcha site for AWV, at the Humera site for both CFM and PPT, they are all in Bega, while the maximum values are for AOD at the Aseb siet, AWV at the Tonga site, CFM at the Agnuak sie, and PPT at the Bahir Dar site, they are all in Kiremt. And also, the minimum values were found for OLR at the

Bahir Dar and Ethiopian Renascence Dam sites, CTP at the Bahir Dar site and CTT at the Humera site, they are all in Kiremt, while the maximum values are for OLR at the Humera site, CTP and CTT at the Dahlak site they are all in Bega. Therefore, almost all of the results in the figures indicate extreme values at similar locales, like those of the observations in Figures 6.5 and 6.6, with a few noted exceptions.

Those results are similar to the findings and the reasons in the study (Liu et al., 2021) from eastern China. The seasonal results for the parameters were similar to those of the observations made in Austria (Yang et al., 2021), Algeria (Khan et al., 2021), eastern China (Liu et al., 2021), and Hong Kong (Yu et al., 2022), despite the fact that there had been no prior studies on the sites in the clustered regions. The discrepancies we discovered were in the minimums with different data periods and site selections. Furthermore, in the study conducted by (Yu et al., 2022) the minimums were primarily at Bega and the maximums at Kiremt.

6.2.4 Yearly Variation of Aerosol Influence

In this section, we summarize the total yearly variations of the parameters for all the selected sites belonging to the four clustered regions. Respectively from top to bottom, the first column panels in the error bar in Figures 6.7 and 6.8 indicate the yearly variations for parameters AOD, AWV, CFM, PPT, OLR, CTP, and CTT from the Terra and Aqua satellites corresponding to the selected sites in the southwest cluster, and the average of all the sites is also superimposed on all plots. Similarly, the other 2^{nd}, 3^{rd} and 4^{th} column panels in the figures produce yearly variations of the parameters for the remaining three clustered regions. The majority of the sites, both in the western and eastern cluster zones, clearly demonstrate interannual variability with frequent minimum and maximum values for parameters, as repeated in the aforementioned figures.

The average of the clustered regions shows the minima at the southeast cluster in 2022 for all AOD, AWV and CFM; in 2010 for PPT and OLR and in 1999 and for OLR with

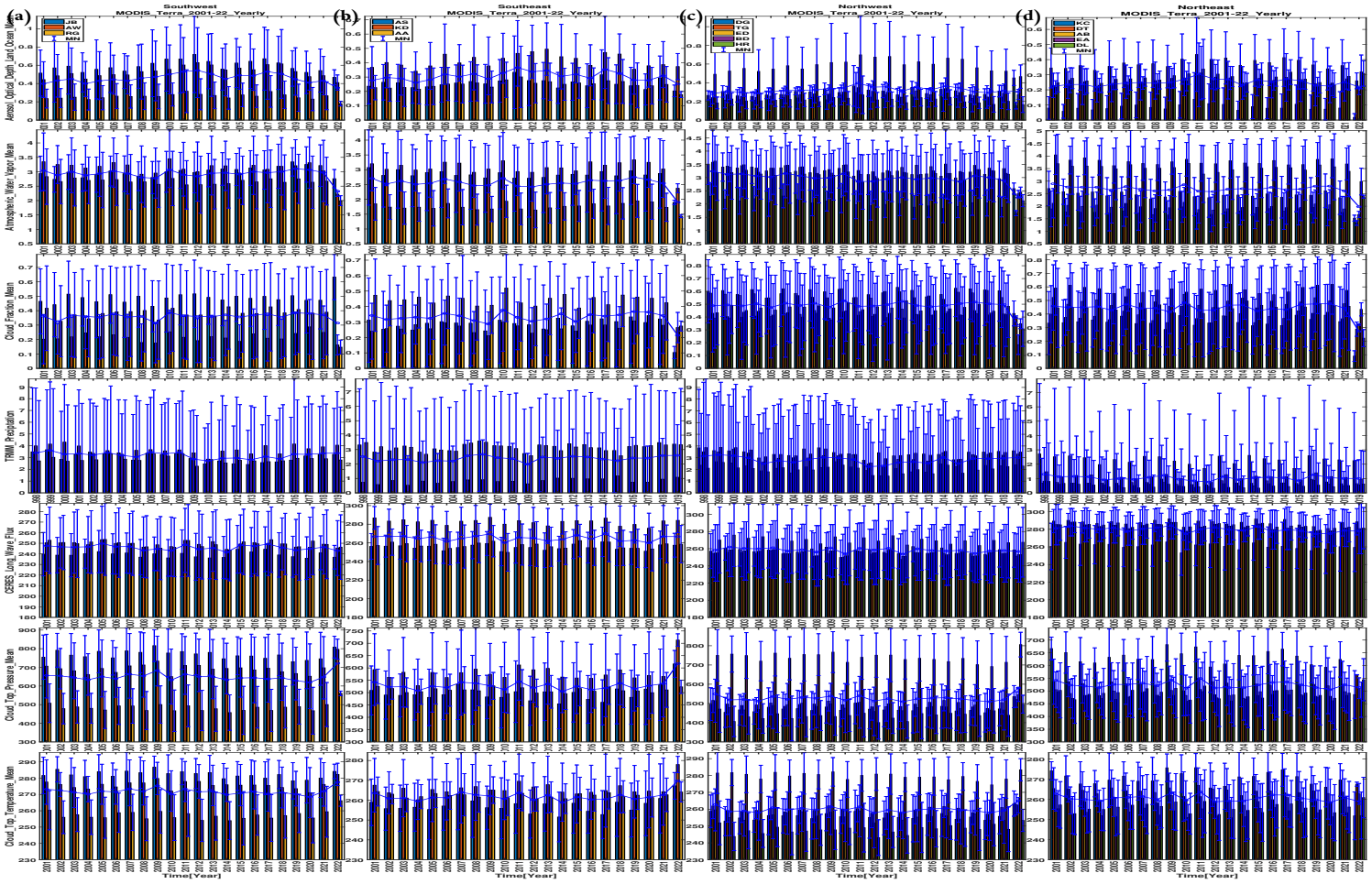

Figure 6.7: The aerosol optical parameters yearly variation [Terra].

their maxima at the northeast cluster in 2010 for AOD, AWV and CFM; in 2009 for PPT; and in 2011 and 2022 for CTP and CTT from both instruments. Accordingly, the AOD, AWV, CFM, PPT, CTP and CTT minimum values are 0.22, 1.90, 0.21, 1.15, 253.86, 504.53 and 257.73 for Terra and 0.18, 1.91, 0.27, 252.14, 533.43 and 262.94 for Aqua, and the maxima are 0.35, 2.33, 0.33, 2.26, 271.23, 619.08 and 268.49 for Terra and 0.35, 2.35, 0.41, 272.22, 640.07 and 272.58 for Aqua, respectively. Here, the parameter PPT is illustrated only in Figures 6.7 and the values for all of the parameters we observed in the Aqua satellite are mostly greater than those of the Terra satellite. The values for the parameters were higher in the southern clusters, specifically in the southwest clusters, than in the northern clusters.

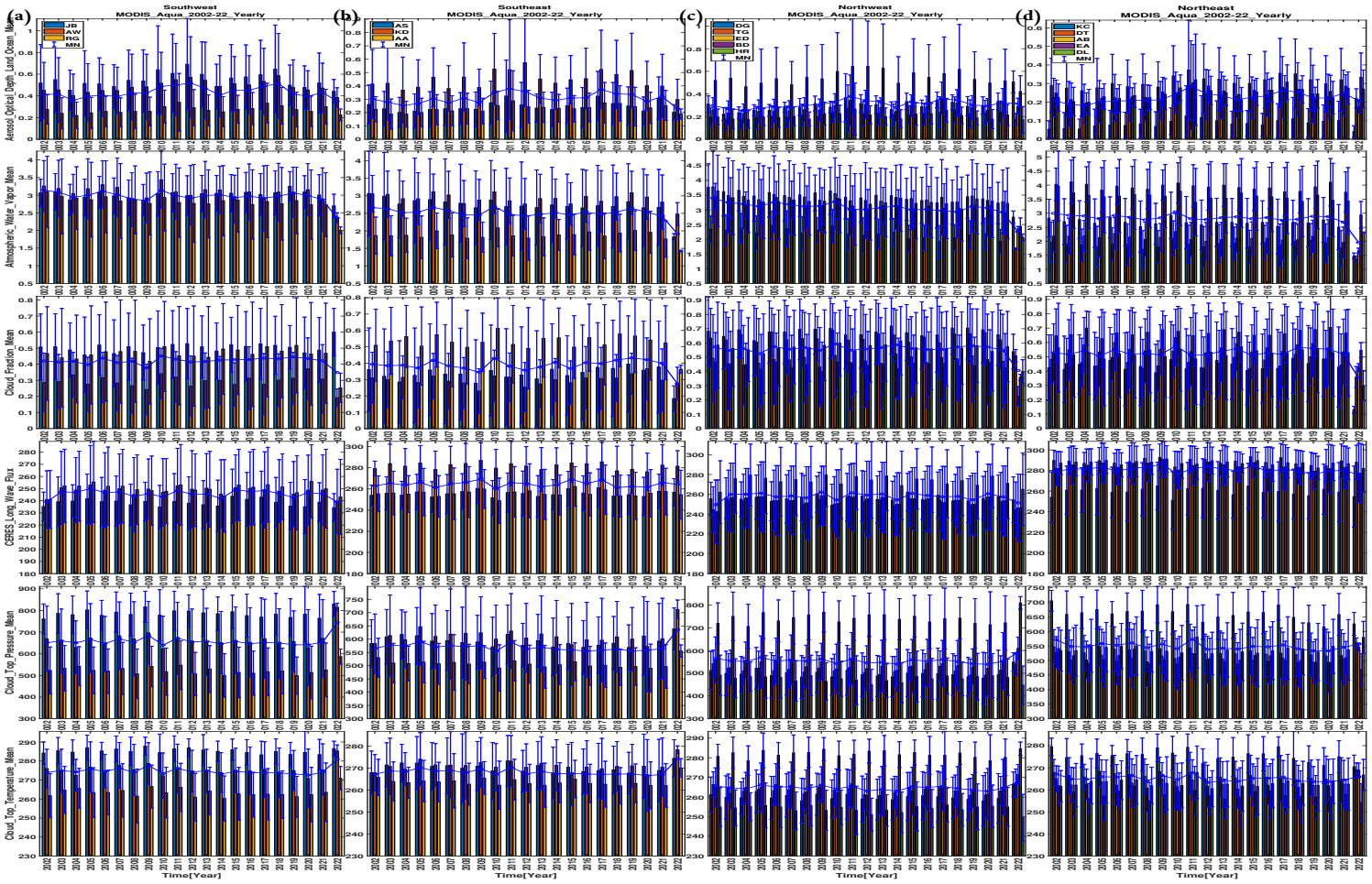

Figure 6.8: The aerosol optical parameters yearly variation [Aqua].

6.2.5 The Explained Variance of Aerosol Contribution

In this study section, the PCA analysis was used to evaluate the contribution of selected satellite-derived aerosol particles, cloud parameters, outgoing long-wave radiation flux, and precipitation dataset parameters at 16 selected sites clustered into four regions over East Africa-Ethiopia. Table 6.1 presents results for the optimum number of the principal component retained based on aerosols, clouds, outgoing long-wave radiation flux, and precipitation datasets. The results in Figures 6.9 present a detailed analysis to investigate the variability explained by the number of significant PCs retained for aerosol particles, clouds, outgoing long-wave radiation flux, and precipitation parameters. The identified PCs were found to be significant at 95% confidence level based on Monte Carlo

Table 6.1: The explained variance based on AOD in precipitation and cloud parameters.

Clusters		Southwest			Southeast			Northwest					Northeast				
Sites		JB	AW	RG	AS	KD	AA	DG	TG	ED	BD	HR	KC	DT	AB	AE	DL
	AOD	76.73933	20.23363	3.02705	94.17940	4.27753	1.54307	82.73777	12.01738	3.65045	1.07927	0.51513	90.25404	5.36274	1.96848	1.58128	0.83347
	AET	64.70823	31.88831	3.40346	97.30233	2.42940	0.26827	80.86167	13.72519	3.81542	1.10606	0.49165	87.50381	7.19404	3.09355	1.55495	0.65365
	AWV	89.26286	7.55244	3.18471	84.03200	11.84184	4.12616	95.52147	2.51904	1.27996	0.51779	0.16175	81.70954	14.57567	1.68779	1.46560	0.56140
	CRF	86.71811	9.05469	4.22720	94.73250	4.42521	0.84229	92.96030	3.58475	2.39505	0.61189	0.44802	55.56792	28.39492	7.78548	7.11895	1.13273
	PPT	62.10693	23.50944	14.38362	64.88465	25.39582	9.71953	67.39023	16.98714	9.15673	4.15465	2.31126	77.47822	11.64260	5.92301	3.51182	1.44435
	OLR	88.72757	9.83584	1.43659	85.63301	12.22916	2.13783	94.79371	2.81389	1.77993	0.61246	0.00000	94.90689	2.34225	2.11515	0.63571	0.00000
	CPT	70.23797	16.88900	12.87303	86.87264	11.84006	1.28731	78.36714	13.47516	3.35201	2.68929	2.11639	80.50630	11.44524	4.67903	1.95688	1.41255
TERRA	CTT	67.55355	17.80640	14.64005	86.29808	12.29272	1.40920	73.79662	15.64307	4.61335	3.53874	2.40822	71.61495	18.02711	5.84235	2.59034	1.92526
	AOD	84.70071	12.61905	2.68024	95.42342	3.54012	1.03645	88.94035	7.16094	2.69740	0.87293	0.32838	88.94690	6.16285	2.86151	1.26048	0.76825
	AET	76.99748	19.53934	3.46318	95.73084	3.89758	0.37157	86.89722	8.89579	3.13974	0.73780	0.32946	88.46001	6.26736	3.53449	0.92067	0.81748
	AWV	92.53369	4.17327	3.29303	88.65611	9.43300	1.91089	96.57223	1.52195	1.26090	0.46834	0.17658	87.97118	7.29076	2.57206	1.33557	0.83042
	CRF	89.88591	7.41667	2.69742	94.08575	4.79364	1.12061	90.48992	5.15982	2.78661	1.40036	0.16330	68.81907	15.17137	8.18359	6.20453	1.62144
	OLR	91.09479	7.34459	1.56061	87.59003	10.87574	1.53423	95.82135	2.14056	1.60456	0.43352	0.00000	94.27929	3.06419	1.99185	0.66467	0.00000
	CPT	45.95326	36.69971	17.34703	69.41749	27.82834	2.75418	81.21971	9.98676	4.37016	2.71255	1.71082	85.13126	7.14464	3.90295	2.27019	1.55096
AQUA	CTT	47.81010	37.12246	15.06745	59.73888	36.95421	3.30691	80.83209	9.53087	5.93915	2.18724	1.51065	76.63567	9.26518	8.37120	4.53936	1.18859

testing (Ngaina, 2015). Notably, the OLR and AWV parameters, both at the Humera and Dahlak sites, had the lowest optimum significant PCs, which was attributed to the course resolution of the datasets from both of the instruments. The number of significant

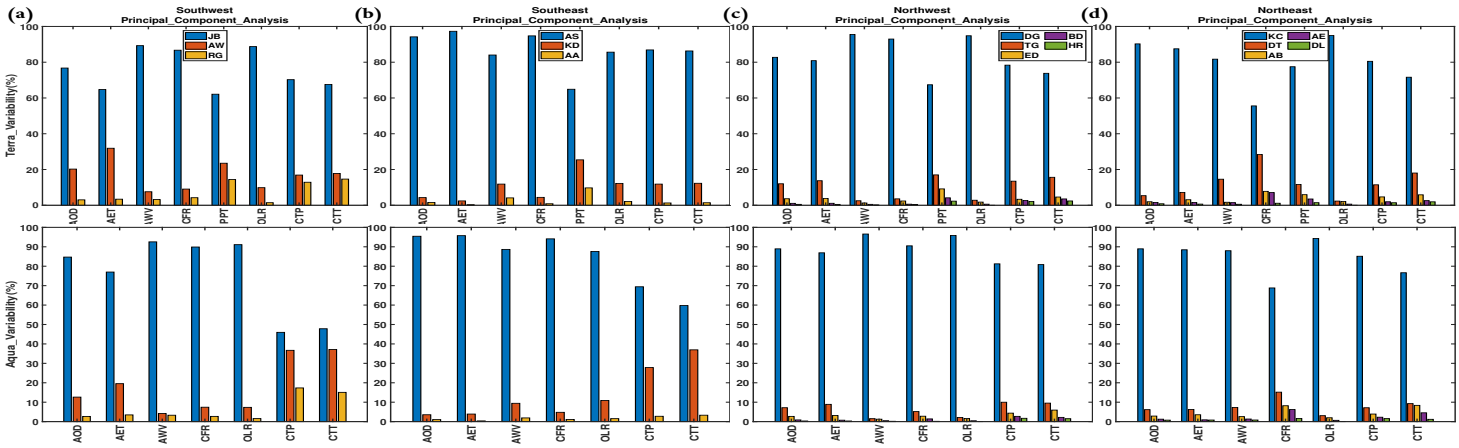

Figure 6.9: The explained variance based on AOD in precipitation and cloud parameters.

PCs retained based on AET at the Awassa site and AWV at the Dangote site was highest compared to the other parameters. The differences in retained PCs point to the different atmospheric dynamics responsible for the behaviour of climate during the various seasons of the year and the spatial coherence arising from both interannual and intraseasonal variability. Further, the use of seasonal and annual total average provides information

on interannual variability only. However, the studies in (Ininda, 1994; Gitau et al., 2013) showed that results from the monthly analysis were better during prolonged rainfall due to high variability. The findings in (Indeje et al., 2000) classified the entire East Africa region into eight and nine near homogeneous zones based on the annual and seasonal observed rainfall, respectively.

6.2.6 The Fire-Map Trajectory

In this research, the backward fire-map trajectory analysis was done using the HYSPLIT model at the Agnuak site from the southwest cluster, at the Kebri Dahar and Addis Ababa sites from the southeast cluster, at the Humera site from the northwest cluster, and at the Aseb site from the northeast cluster. We have utilized a five-day backward trajectory analysis to identify the sources of atmospheric aerosol particles at 500–5000 metres above ground-level MAGL. For the selected five location sites: the 2^{nd} row panels for the Agnuak site in 2002, the 3^{rd} row panels for the Kebri Dahar site in 2011, the 4^{th} row panels for the Addis Ababa site in 2015, the 5^{th} row panels for the Humera site in 2011, and the 6^{th} row panels for the Aseb site in 2012, with a high factor loading based on TRMM 3B43 satellite-derived rainfall estimates were utilized. The 1^{st} row panels in the Figures are to illustrate the fire map trajectories for the sources from the biomass burnings BBs. The HYSPLIT trajectories were computed for the start, June 01 and 16 (the 1^{st} and 2^{nd} column panels); mid, July 01 and 16 (the 3^{rd} and 4^{th} column panels); and end, August 01, 16 and 31 (the 5^{th}, 6^{th} and 7^{th} column panels), of the Kiremt season, as shown in Figures 6.10.

At the beginning of the season, the backward trajectories identified the continental source regions as the Arabian deserts and the Indian subcontinents. The selected continental stations included Agnuak, Kebri Dehar, Addis Ababa, and Humera. The locations of the maritime source regions were in the sub-western Indian Ocean, with the selected sink station at the Aseb site. In the middle of the season, the source regions for the study

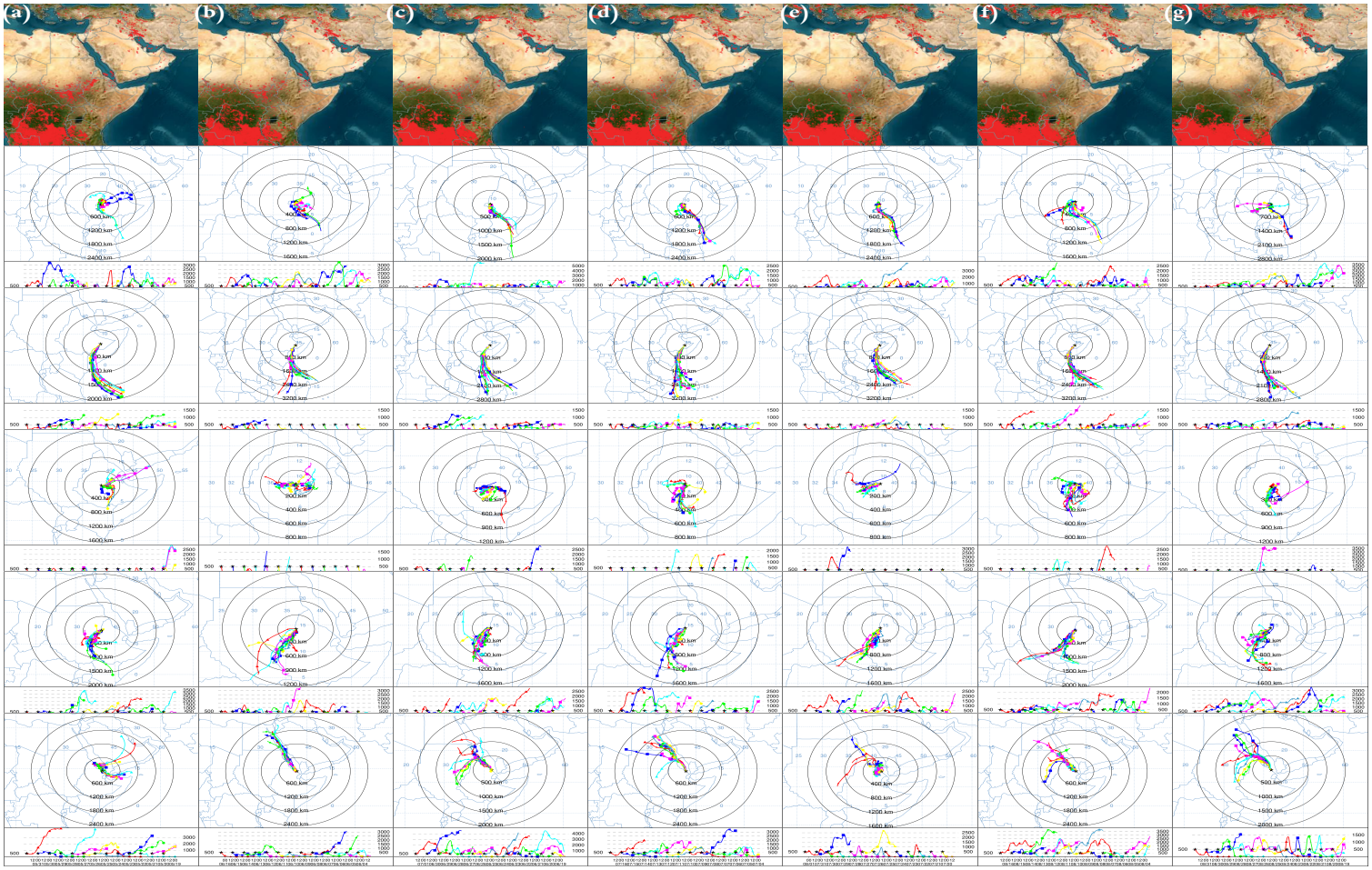

Figure 6.10: Fire maps-HYSPLIT backward trajectories during start, mid and end of kiremt.

area sites were in the southwest Indian Ocean, Kenya, Madagascar, Uganda, Sudan, and Egypt. At the end of the season, all the source regions for all stations at all levels were located in the Arebian Deserts, the southwest Indian Ocean, Central Africa, Kenya, Madagascar, Uganda, Sudan, and Egypt. Here, the study area regions by themselves were also the source regions at the beginning, middle, and end of the season at all levels. And we observed that there were active fires in all the source regions during the beginning, middle, and end of the season on the fire map projected as in the 1st row panels of Figures. Generally, at different levels, the transported aerosol particles in the atmosphere show varied source regions. The atmospheric aerosol particles undergo vertical mixing inland in East Africa-Ethiopia. Further, several high mountains > 2000m are situated near

the Great Rift Valley area in East Africa-Ethiopia. They include Mount Kilimanjaro, Mount Kenya, and Mount Rwenzori. These mountains block the eastward transport of the Sahel smoke as well as dust from the Bodele Depression (Washington and Todd, 2005; Fiedler et al., 2014). Therefore, these mixed aerosols accounted for increased rainfall over locations with high factor loadings based on TRMM 3B43 rainfall (Yang et al., 2013).

6.3 Conclusions

The purpose of this study is to investigate effects of aerosol particles on precipitation and cloud parameters based on the spatiotemporal distribution variations retrieved from the MODIS, TRMM 3B43, and CERES sensors over a period of 22 years (for Terra: January 2001 to December 2022, and for Aqua: July 2002 to December 2022). Those parameter retrievals included the spatial, monthly, seasonal, and yearly values at sixteen selected sites clustered in four regions with their corresponding averages. The main conclusions drawn from our work are as follows:

1. The seasonality total spatial averaged values for the aerosol particles optical depth parameters are $0.00 \leq AOD \leq 0.35$; for cloud parameters, they are $0.00 \leq AWV \leq 3.50$, $0.00 \leq CFM \leq 0.80$, $400.00 \leq CTP \leq 800.00$, and $2500.00 \leq CTT \leq 300.00$; values for the precipitation, they are $0.00 \leq PPT \leq 25.00$; and for the outgoing long-wave radiation flux, they are $100.00 \leq OLR \leq 350.00$, with their minimums occurring in the Bega season and their maximums occurring in the Kiremt season. Across the globe, we consider the study area $\{3–18^0$ N, $24–48^0$ E$\}$ regions within it.

2. The minimum monthly values are found at the Kebri Dahar site for ADD, at the Kombolcha site for AWV, at the Humera site for both CFM and PPT, they all in January and December, while their maximum values are AOD at the Aseb siet, AWV at the Tonga site, CFM at the Agnuak sie, and PPT at the Bahir Dar site, they all in July; the minimum values were found for OLR at the Humera site and

CTP at the Bahir Dar site both in August and CTT at the Raga site in March and April, while the maximum OLR value is at the Kebri Dahar site in February; the maximum CTP value is at the Dahlak site in January and December; the maximum CTT value is at the Dahlak site in November. Exceptionally, the minimum values for the OLR are at the Bahir Dar and Ethiopian Renascence Dam sites in July and August for the Terra and Aqua instruments, respectively.

3. The minimum values are found at the Kebri Dahar site for ADD, at the Kombolcha site for AWV, and at the Humera site for both CFM and PPT; they are all in Bega, while the maximum values are for AOD at the Aseb siet, AWV at the Tonga site, CFM at the Agnuak sie, and PPT at the Bahir Dar site; they are all in Kiremt. And also, the minimum values were found for OLR at the Bahir Dar and Ethiopian Renascence Dam sites, CTP at the Bahir Dar site, and CTT at the Humera site; they are all in Kiremt, while the maximum values are for OLR at the Humera site, CTP, and CTT at the Dahlak site; they are all in Bega.

4. The total annual average variation shows the minima at the southeast cluster in 2022 for all AOD, AWV and CFM; in 2010 for PPT and OLR and in 1999 and for OLR with their maxima at the northeast cluster in 2010 for AOD, AWV and CFM; in 2009 for PPT; and in 2011 and 2022 for CTP and CTT from both instruments. Accordingly, the AOD, AWV, CFM, PPT, CTP and CTT minimum values are 0.22, 1.90, 0.21, 1.15, 253.86, 504.53 and 257.73 for Terra and 0.18, 1.91, 0.27, 252.14, 533.43 and 262.94 for Aqua, and the maxima are 0.35, 2.33, 0.33, 2.26, 271.23, 619.08 and 268.49 for Terra and 0.35, 2.35, 0.41, 272.22, 640.07 and 272.58 for Aqua, respectively.

5. The OLR and AWV parameters, both at the Humera and Dahlak sites, had the lowest optimum significant PCs, whereas the PCs retained based on AET at the Awassa site and AWV at the Dangote site were the highest compared to the other

parameters. The differences in retained PCs point to the different atmospheric dynamics responsible for the behaviour of climate during the various seasons of the year and the spatial coherence arising from both interannual and intraseasonal variability. And our observation using the HYSPLIT model and fire map confirms that transported aerosol particles in the atmosphere show varied source regions, mostly the Arebian desert and the southwest Indean ocean, at different levels.

Chapter 7

Correlation of Aerosol Particles with Clouds and Radiation Budget Over East Africa-Ethiopia Using MODIS Satellite Data

The chapter is to be cited as:

Alemu, A. A. and Raju, J. P.: Correlation of Aerosol Particles with Clouds and Radiation Budget Over East Africa-Ethiopia Using MODIS Satellite Data: Part 02, Journal of Quantitative Spectroscopy & Radiative Transfer JQSRT, Elsevier, X, XXX–XXX, 2024.

7.1 Introduction

Our planet Earth consists of the atmosphere, hydrosphere, cryosphere, land surface and biosphere. It is a complex system of interacting physical, chemical and the biological processes that provides a natural laboratory whose experiments have been running since the beginning of time. The gaseous part above the Earth's surface includes traces of other gaseous, liquid and solid substances. Its weather, radiation balance, formation of clouds and precipitation, atmospheric flow, reservoir of natural and anthropogenic trace gases, transport of heat, water vapour, tracers, dust and aerosols (Shrestha and Singh, 2014; Kafle and Coulter, 2013; Grythe, 2017).

Studies indicated that aerosol particles positively constellated with cloud parameters and radiation budget. There is also clear and rapidly growing evidence that atmospheric aerosol particles have profound impacts on the thermodynamics and radiative energy budgets of the Earth. The aerosol particles affect the atmosphere: directly by altering the properties of the radiation energy budget through scattering and absorbing the solar radiation; indirectly by affecting the cloud micro-physical properties; and semi-directly through the absorbed radiation energy by aerosol particles, which is able to increase the temperature of the surrounding air, resulting in the evaporation of cloud droplets and ice particles (Myhre et al., 2013; Kafle and Coulter, 2013) (Myhre et al., 2013; Li et al., 2021b; Kaufman et al., 2000b; Marchand et al., 2010).

The aerosol particles-cloud parameters-precipitation interactions attract more attention, so regional as well as global scientific observations are needed to qualify and confirm the situations. From a previous literature reviews, we have found that there are few studies on atmospheric aerosol particles optical properties in East Africa–Ethiopia using ground or satellite data (Homa et al., 2017; Getachew, 2009; Eshet and Raju, 2022). However, to date, no one has reported the correlation of aerosol particles with cloud parameters, precipitation and radiation budget using satellite data from the Moderate Resolution Imaging Spectroradiometer MODIS, Tropical Rainfall Measuring Mission TRMM, and Clouds and the Earth‘s Radiant Energy System CERES.

Hence, in this study, we used the climatological database of the aerosol particles optical properties, namely the aerosol optical depth AOD and Ångström Exponent AET (Tomasi and Lupi, 2017; B AL-Taie et al., 2020; Kumar et al., 2015), and the cloud parameters such as atmospheric water vapor AWV, the mean cloud fraction CFM, cloud top pressure CTP, and cloud top temperature CTT (Sporre, 2016; Barthlott and Hoose, 2018) from MODIS, the precipitation PPT (Barthlott and Hoose, 2018; Li et al., 2017) from TRMM, and the out going long-wave radiation OLR flux (Myhre et al., 2013; Lippmann, 2000) from CERES satellite instruments, to identify the interactions over East Africa-Ethiopia.

7.2 Results and Discussion

After extracting the HDF datasets and collecting their spatial raster AOD, AWV, CFM, CTP, and CTT array values from MODIS, PPT array values from TRMM 3B43, and OLR array values from CERES during January 2001–December 2022, the AET values were calculated from the AOD values using the formula described in the methodology Section 3.6.1. We also perform the AOD combined temporal correlation variation with all parameters and the spatial correlation with the parameters from MODIS Satellite. This section presents the results with their corresponding appropriate discussions for 16 selected sites clustered into four regions, i.e., southwest, southeast, northwest, and northeast of the study area. In addition, we discuss the multiple linear regression analysis and TOA-surface radiative forcing in this section.

7.2.1 Optical Parameters Spatial Correlation

In this section, respectively from right to left Bega, Tseday, Kiremt, Belg and Annual, we presented the seasonal as well as the total annual average spatial correlation distribution variations for the study periods 2001–2022. The distribution fluctuations for the spatial correlation of the parameters we observed in these research findings are shown using Figures 7.1 and 7.2, for the Terra and Aqua satellite data, respectively. Our observations show that a slight variation ranges between -1.0 and 1.0. They include the research findings that contain a correlation of AOD with: the Ångström Exponent COA, 1^{st} upper panels, the atmospheric water vapor COW, 2^{nd} panels, the cloud fraction COF, 3^{rd} panels, the cloud top pressure COP, 6^{th} panels, and the cloud top temperature COT (lower panels) over the globe we take the study area $\{3–18^0$ N, $24–48^0$ E$\}$ regions with in it.

From both the seasonality and total annual results, we can observe that the correlations of the parameters are generally oriented towards the western part of the study area regions, mostly in the southwest of the study area regions. The seasonality distribution variation

shows that the minimum values are found in the Bega season, 1st column panels, and the maximum values are in the Kiremt season, 3rd column panels. The Belg season, 4th column panels, is the next to have minimum values, while the next maximum values for the Kiremt season are in the Tesday season, 2nd column panels, for both of the Terra and Aqua instruments. The results are similar to the findings of the studies from the Taklimakan desert in China (Li et al., 2021c) and the Nile River Basin in Ethiopia (Getachew et al.,

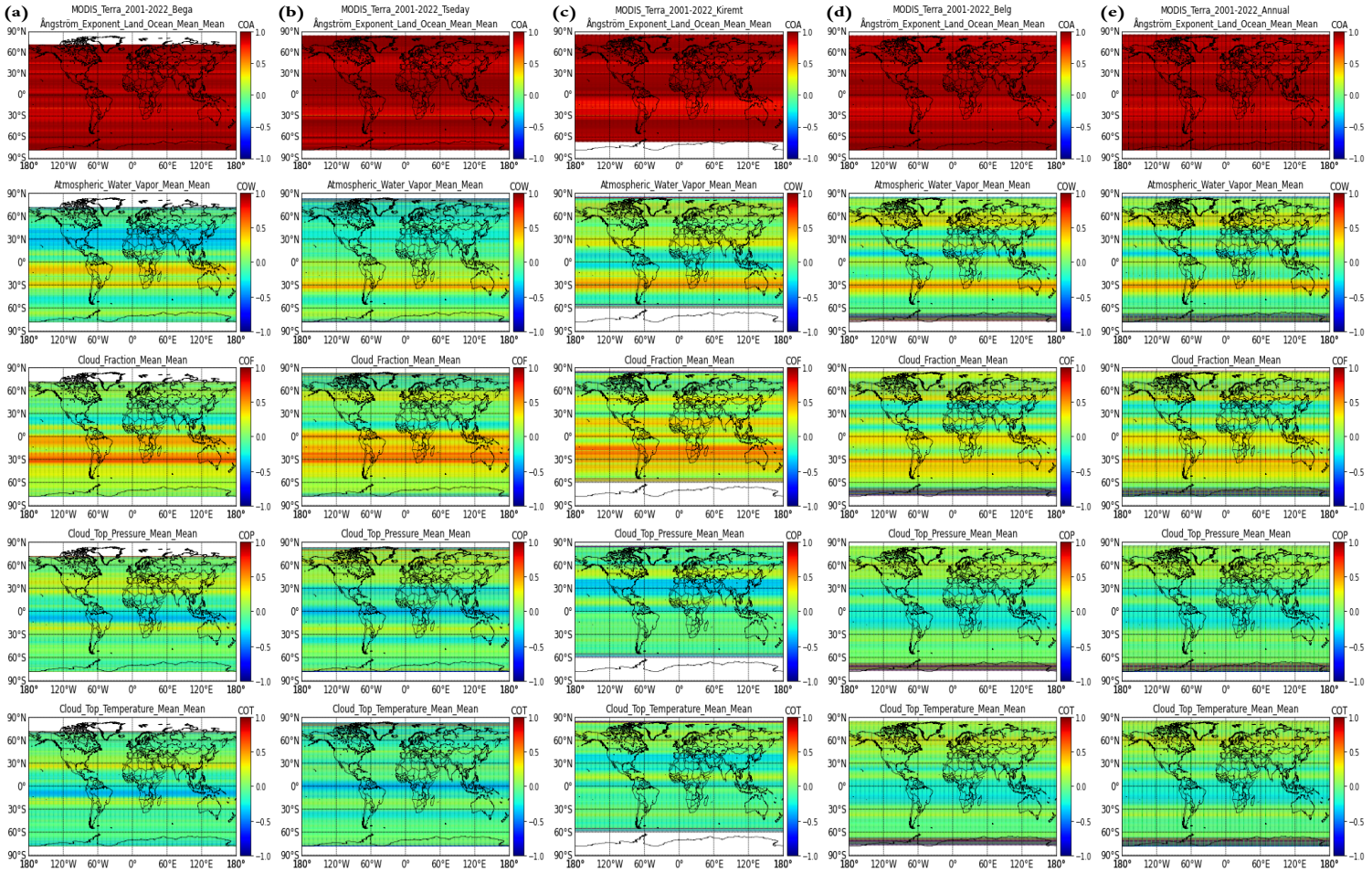

Figure 7.1: The aerosol optical parameters spatially correlated distribution [Terra].

2020) while they contradict the observations of the studies at four selected sites: Addis Ababa, Debre Markos, and Debre Tabor in Ethiopia, and Djibouti in Djibouti (Homa et al., 2017; Eshet and Raju, 2022). In the case of the instruments, greater values are observed from the Aqua instrument and less from the Terra instrument, which contradicts the observations in (Kharol et al., 2011).

So, we can generalize, that the findings in our observations show that the correlations of the parameters have the seasonal minimums in the Bega season and the maximums in the Kiremt season, and the spatial correlations have the minimums mostly in 33–42°E and the maximums in the southwest of the study area regions, respectively. And the correlations of the parameters are higher on the Terra instrument relative to the Aqua instrument. Even

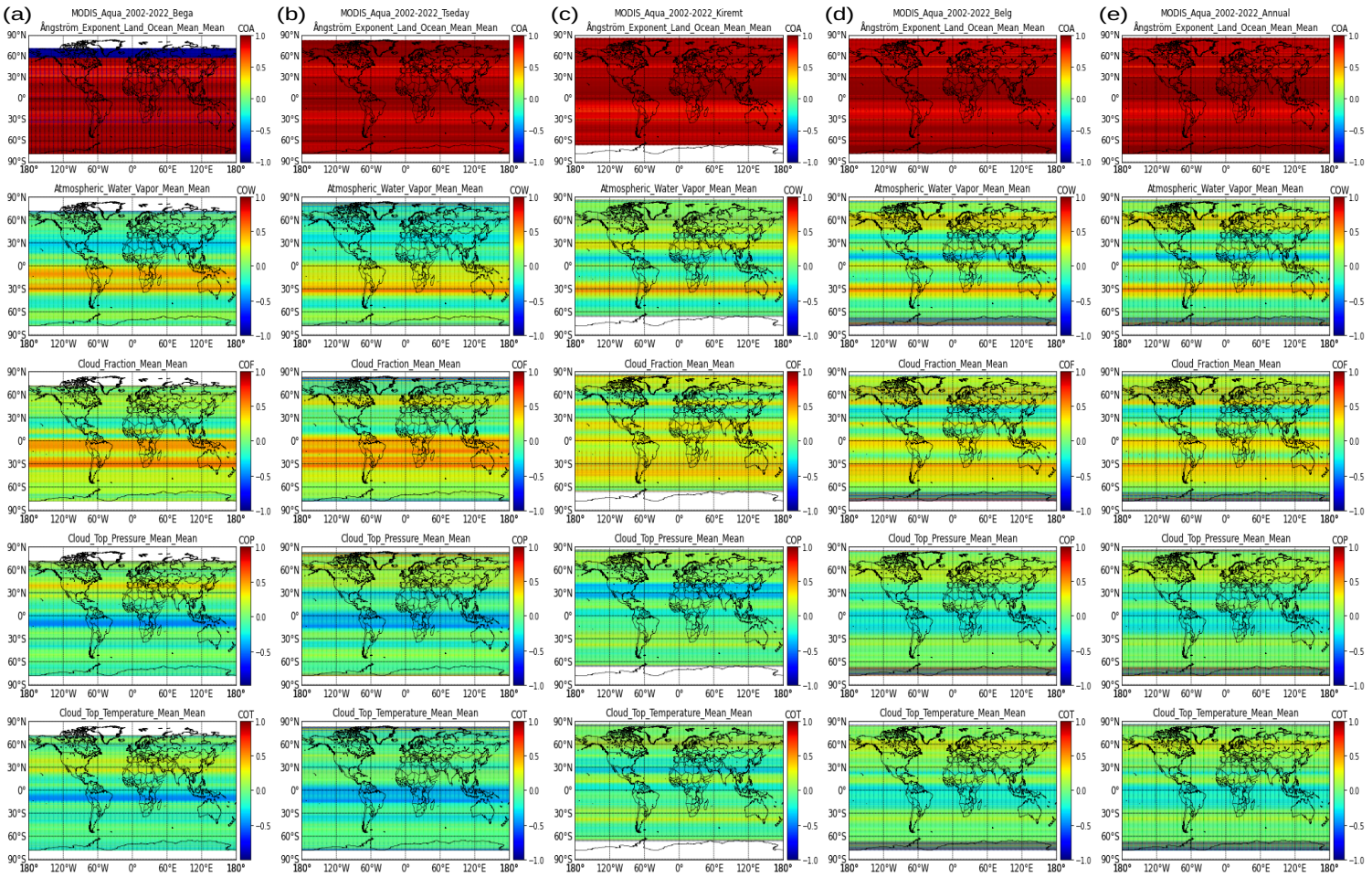

Figure 7.2: The aerosol optical parameters spatially correlated distribution [Aqua].

if there are also contradictory findings to our results, the studies undergone by different scholars we discussed above and those in (Kalisa et al., 2023; Boiyo et al., 2018a) about the seasonality of the correlations of the parameters fluctuation, the different local activities, and the long-range aerosol particles transport to the study area regions confirmed our observation (Torres-Delgado et al., 2021; Li et al., 2021c; Ngaina et al., 2014).

7.2.2 Optical Parameters Temporal Correlation

This section describes the results of the total monthly average temporal value fluctuations for the aerosol particles, cloud parameters, precipitation, and outgoing long-wave radiation flux we discussed earlier. The temporal combined monthly mean values of the parameters are constructed for each site in the four clustered regions. The results of our observations

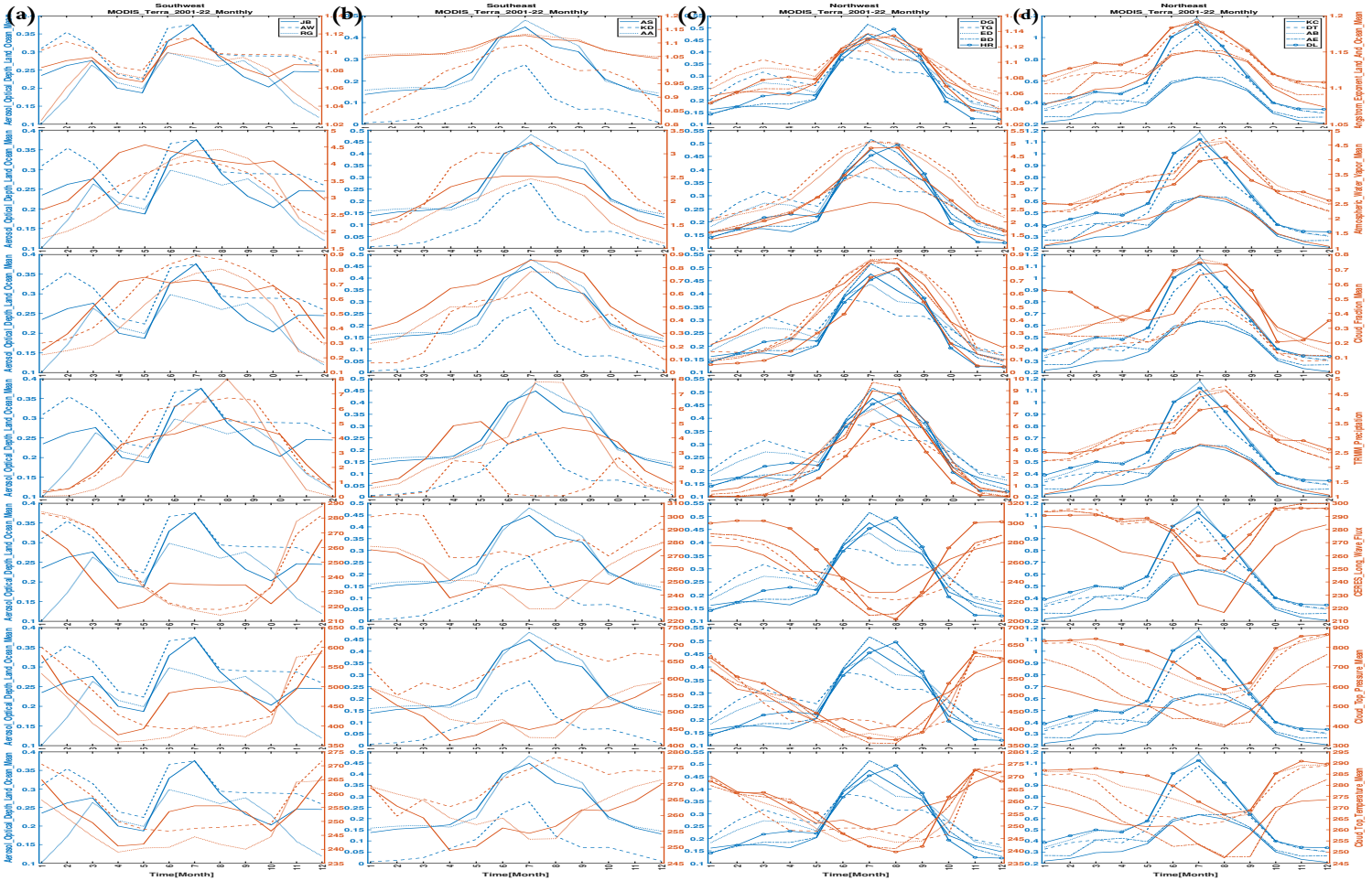

Figure 7.3: The aerosol optical parameters combined monthly variation [Terra].

for the parameters combined with AOD values are illustrated in Figures 7.3 and 7.4 for the Terra and Aqua satellite data, respectively. Here, in Figures 7.3 and 7.4, the increase and decrease fluctuations for the parameters AET, AWV, CFM and PPT are gently positively associated with AOD, while for OLR, CTP and CTT they are vice-versa!

In the southwest cluster, 1st column panels, the minimum values for the parameters are

observed in South Sudan at the Raga site, while the maximum values are observed in Ethiopia at the Agnuak site for AOD, AET, CFM, CTP, and CTT; in South Sudan at the Juba site for AWV; and at the Raga site for PPT and OLR. For the southeast cluster, 2nd column panels, the minimum values are observed in Ethiopia at the Kebri Dahar site for AOD, AET, CFM, and PPT. The other minimas in Ethiopia are at the Addis Ababa site for AWV, OLR, CTP, and CTT. And the maximum values are observed in Ethiopia at the Addis Ababa site for AOD, AET, and PPT, and still in Ethiopia at the Kebri Dahar site for AWV, OLR, CTP, and CTT. Another maximum value is observed in Eritrea at the Aseb site for CFM. Here, the results we observed and discussed in the southern clustered regions are from both the Terra and Aqua satellite instruments.

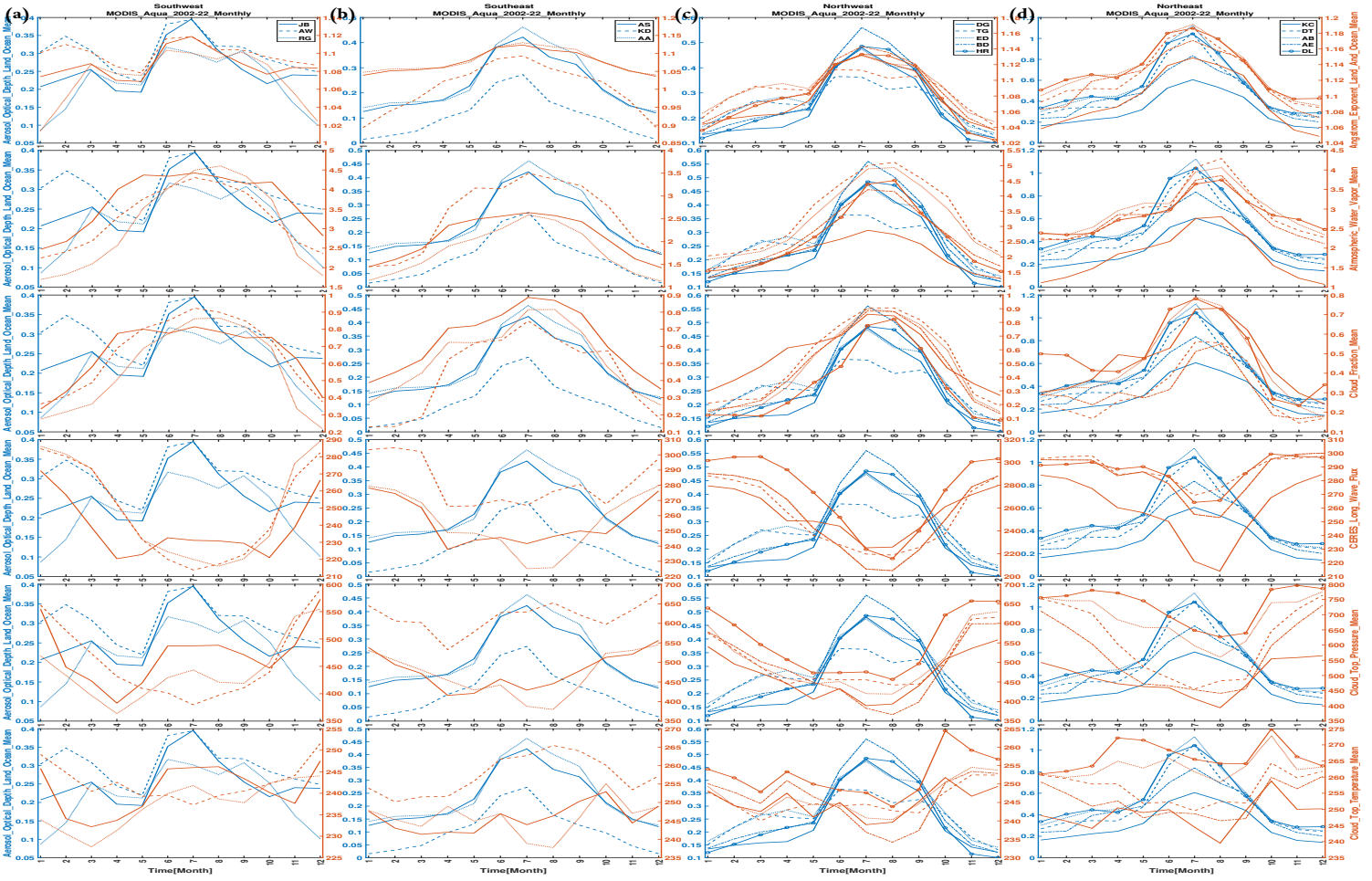

Figure 7.4: The aerosol optical parameters combined monthly variation [Aqua].

In the northwest cluster, 3rd column panels, minimum values for the parameters are observed in the Ethiopian at the Humera site for AOD, AET, CFM, PPT, OLR, and CTT. The other minima in Ethiopia are at the Dangote sites for AWV and at the Bahir Dar site for CPT. And the maximum values for the parameters are observed in Ethiopia at the Bahir Dar site for AOD, AET, and PPT and at the Humera sites for OLR. The other maxima values for the parameters are observed in South Sudat at the Tonga site for AWV, CFM,CTP, and CTT. When we moved to the northeast cluster, 4th column panels, the minimum values for the parameters were observed in Ethiopia at the Kombolcha site for AOD, AET, AWV, OLR, CTP, and CTT. The other minimum values for the parameters were observed in Djibouti at the Djibouti site for CFM and in Eritrea at the Dahlak site for PPT. And the maximum values for the parameters are observed in Eritrea at the Aseb site for AOD, AET and CFM and at the Dahlak site for CTP and CTT. The other maximum values for the parameters are observed in Djibouti at the Djibouti site for AWV and OLR, and also in Ethiopia at the Kombolcha site for PPT. Here, the results we observed and discussed in the northern clustered regions are from both the Terra and Aqua satellite instruments, with some exceptions. Minimum values for the parameters are observed for OLR at the Bahir Dar and the Ethiopian Renascence Dam sites, and maximum values for CTP and CTT at the Tonga site in the Aqua satellite.

In general, for both of the Terra and Aqua instruments: the minimum values are found at the Kebri Dahar site for both AOD and AET, at the Kombolcha site for AWV, at the Humera site for both CFM and PPT, they all in January and December, while their maximum values are AOD and AET at the Aseb siet, AWV at the Tonga site, CFM at the Agnuak sie, and PPT at the Bahir Dar site, they all in July; the minimum values were found for OLR at the Humera site and CTP at the Bahir Dar site both in August and CTT at the Raga site in March and April, while the maximum OLR value is at the Kebri Dahar site in February; the maximum CTP value is at the Dahlak site in January and December; the maximum CTT value is at the Dahlak site in November. Exceptionally,

the minimum values for the OLR are at the Bahir Dar and Ethiopian Renascence Dam sites in July and August for the Terra and Aqua instruments, respectively.

7.2.3 Aerosols Radiative Forcing

To understand aerosol particles loading on regional radiation flux distribution, we have carried out numerical aerosol particles radiative forcing calculations. The total monthly, seasonal and yearly temporal averages of the top of the atmosphere TOA with their corresponding surface radiative forcing values were obtained using the formula in Section 3.6.7 from the above-mentioned parameters. In the upcoming subsections 7.2.3, 7.2.3 and 7.2.3, we present these results with their appropriate brief discussions.

Monthly Variation of Radiative Forcing

In this subsection, the Figures in 7.5a-7.5d are to illustrate the results for the aerosol particles, surface in 1st and 3rd row panels as well as atmospheric in 2nd and 4th row panels, radiative forcing. The monthly mean values are constructed based on the F_{Surf} from AOD and F_{TOA} from OLR parameters for each site of the four clustered regions, and the results are illustrated in the Figures. In the southwest cluster (Fig. 7.5a), the minimum values are observed in South Sudan, at the Juba site for F_{Surf} and at the Raga site for F_{TOA}, while the maximum values are observed still in South Sudan, both at the Raga site from Terra and Aqua instruments. For the southeast cluster (Fig. 7.5b), the minimum values are observed in Ethiopia, at the Kebri Dahar site for F_{Surf} and at the Awassa site for F_{TOA}, and the maximum values are observed still in Ethiopia, at the Awassa site for F_{Surf} and at the Addis Ababa site for F_{TOA}, from Terra and Aqua instruments.

For the northwest cluster, Fig. 7.5c, minimum F_{Surf} and F_{TOA} values are observed in Ethiopia, both at the Bahir Dar site, while maximum values are observed at the Humera site for F_{Surf} in Ethiopia and at the Tonga site in South Sudan for F_{TOA}, from Terra

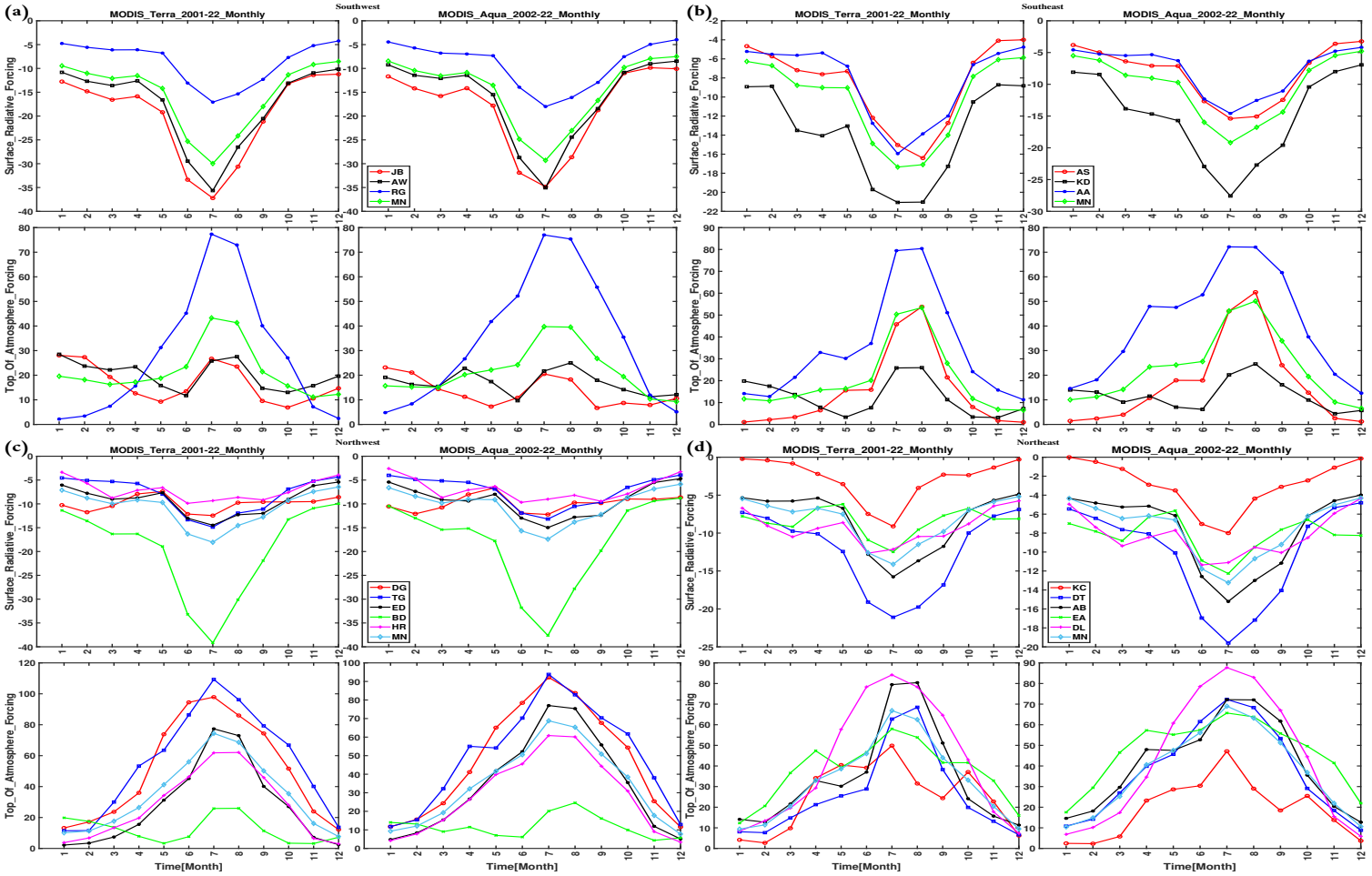

Figure 7.5: The atmospheric and surface radiative forcing monthly variation.

and Aqua instruments. And when we move to the northeast cluster, Fig. 7.5d, their minimums are in Djibouti at the Djibouti site for F_{Surf} and in Ethiopia at Kombolcha the site for F_{TOA}, while their maximum values are in Ethiopia at the Kombolcha site for F_{Surf} and in Eritrea at the Dahlak site for F_{TOA}, from Terra and Aqua instruments.

To generalize, the minimum values observed are in the northwest cluster for F_{Surf} and in the southeast cluster for F_{TOA}, while the maximum values for F_{Surf} are in the northeast and for F_{TOA} in the northwest cluster from both instruments. For the Terra satellite, the minimum values of F_{Surf} and F_{TOA} were found to be -39.17 Wm^{-2} and 1.01 Wm^{-2} in July and December, while the maximum values were to be -0.22 Wm^{-2} and 109.30 Wm^{-2} in January and July. Moreover, the Aqua satellite also shows similar results, with the

minimum F_{Surf} and F_{TOA} values observed during July and December with -36.56 Wm^{-2} and 1.17 Wm^{-2}, respectively, while the maximum values in October and August at the two clusters (Fig. 7.5(b, d)) are -0.64 Wm^{-2} and 93.80 Wm^{-2}. From the Figures, we can observe that the minimum values are at the Bahir Dar site for F_{Surf} and at the Awassa site for F_{TOA}, both in Ethiopia, while the maximum values are in Ethiopia at the Kombolcha site for F_{Surf} and for F_{TOA} at the Tonga site in South Sudan.

Seasonal Variation of Radiative Forcing

The seasonal variations of the radiative forcing parameters F_{Surf} and F_{TOA} at the selected sites clustered into four areas are addressed in this section. The evolutions of these parameters estimated from the study periods of 2001–2022 are shown in Figures 7.6 for the Terra and Aqua satellite data together with their corresponding total average means. In addition, Tables 7.1 and 7.2 also illustrate the seasonal observation of the radiative forcing parameters. Respectively, the minimum values for the parameters F_{Surf} and F_{TOA} are found in the Kiremt and Bega seasons, and their maximum values are found in the Bega and Kiremt seasons, which are in the vice-versa in all of the clusters and both of the instruments.

In the southwest cluster, minimum values for the parameters are observed in South Sudan at the Juba site for F_{Surf} and at the Raga site for F_{TOA}, while the maximum values are observed in South Sudan at the Raga site. For the southeast cluster, the minimum values are observed in Ethiopia at the Kebri Dahar site for F_{Surf} and at the Awassa site for F_{TOA}, and the maximum values are observed in Ethiopia at the Awassa site for F_{Surf} and at the Addis Ababa site for F_{TOA}. Here, the results we observed and discussed in the southern clustered regions are from both the Terra and Aqua satellite instruments.

In the northwest cluster, minimum values for the parameters are observed in Ethiopia at the Bahir Dar site for F_{Surf} and at the Ethiopia Renascence Dam site for F_{TOA}, and the maximum values for the parameters are observed in Ethiopia at the Humera site for

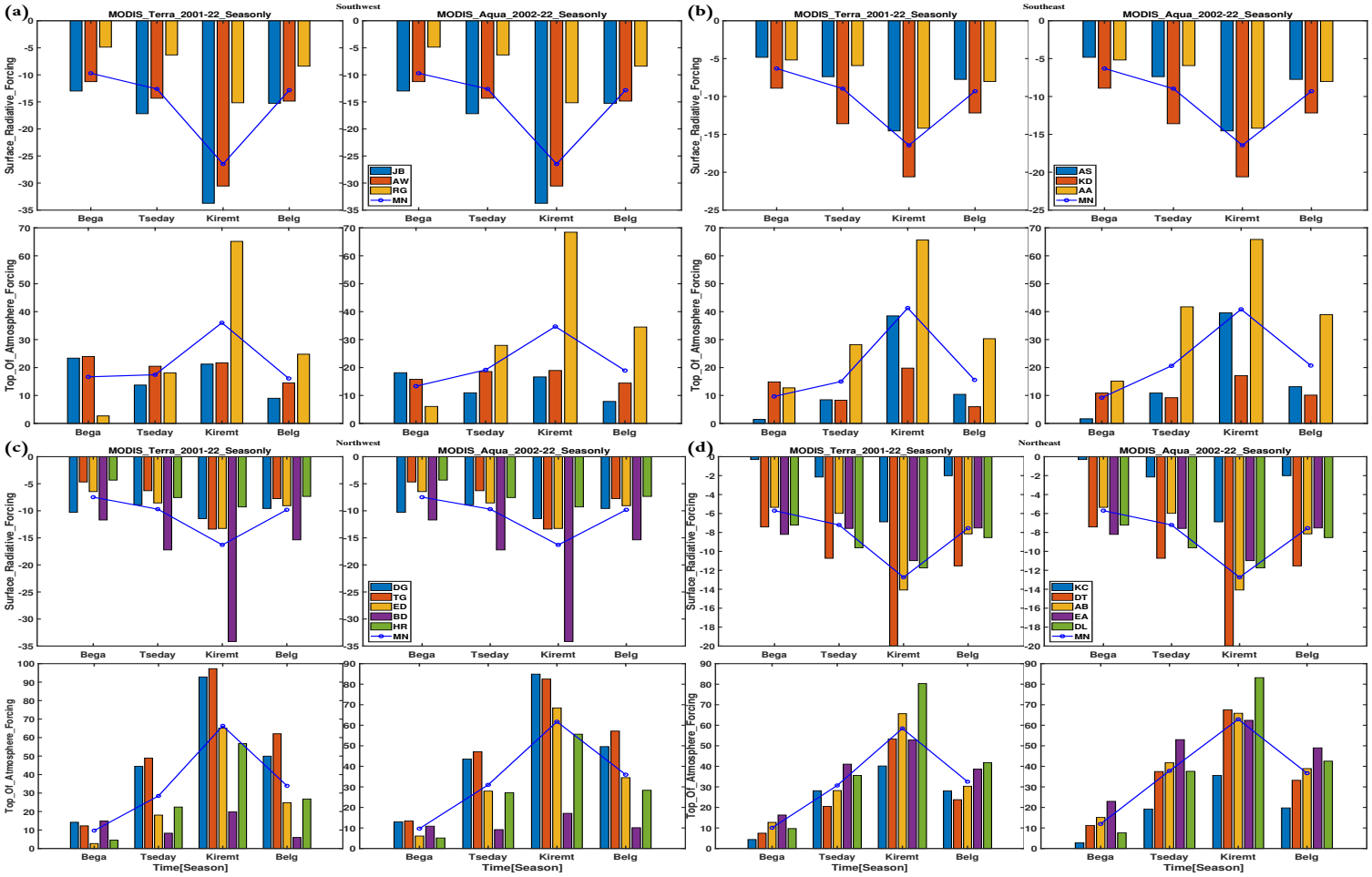

Figure 7.6: The atmospheric and surface radiative forcing seasonal variation.

F_{Surf} and in South Sudan at the Tonga site for F_{TOA}. When we moved to the northeast cluster, the minimum values for the parameters were observed in Djibouti at the Djibouti site for F_{Surf} and in Ethiopia at the Kombolcha site for F_{TOA}, and the maximum values for the parameters were observed in Ethiopia at the Kombolcha site for F_{Surf} in Eritrea and at the Dahlak site for F_{TOA}. Here, the results we have observed and discussed in the northern clustered regions are from both the Terra and Aqua instruments, with the exception that the maximum values of F_{TOA} are observed in Ethiopia at the Dangote site. In general, for both Terra and Aqua instruments, the minimum values found at the Bahir Dar site for F_{Surf} are -34.16 Wm^{-2} and -32.41 Wm^{-2} in the northwest cluster, at the Awassa site for F_{TOA} are -4.88 Wm^{-2} and -4.72 Wm^{-2} in the southwest cluster, while the

maximum values found at the Komolcha site for F_{Surf} are -0.30 Wm^{-2} and -0.22 Wm^{-2} in the northeast cluster, and for F_{TOA} are around 97.27 Wm^{-2} at the Tonga site and 92.78 Wm^{-2} at the Dangote site in the northwest cluster. And the two Tables 3 and 4 are for atmospheric forcing F_{Atm} and its heat rate T_{Rate} calculated using Terra and Aqua instruments. The minimum values found at the Kombolcha site for F_{Atm} are -4.73 Wm^{-2} and 3.26 Wm^{-2}; for T_{Rate} are 0.0002 K/s and 0.0001 K/s; they are all in the southwest cluster, while the maximum values found at the Tonga site for F_{Atm} are 110.65 Wm^{-2} and 96.13 Wm^{-2}; and for T_{Rate} are around 0.0036 K/s and 0.0031 K/s; all are in the northwest cluster.

Table 7.1: The mean atmospheric and surface radiative forcing pattern [Terra].

Sites		JB	AS	KD	AW	RG	AA	DG	TG	KC	ED	DT	BD	AB	AE	HR	DL	SW	SE	NW	NE
Bega	AF	23.15568	1.41174	14.69848	23.97576	2.64318	12.73333	14.28712	12.24470	4.42121	2.64318	7.33750	14.69848	12.73333	16.42727	4.49848	9.78068	16.59154	9.61452	9.67439	10.14000
	SF	-12.98739	-4.82904	-8.90658	-11.25702	-4.88179	-5.18049	-10.28153	-4.66734	-0.30460	-6.45349	-7.42012	-11.69769	-5.34913	-8.20712	-4.32519	-7.21522	-9.70873	-6.30537	-7.48505	-5.69924
	AT	36.14307	6.24078	23.60507	35.23278	7.52498	17.91382	24.56865	16.91204	4.72582	9.09667	14.75762	26.39617	18.08247	24.63440	8.82368	16.99590	26.30027	15.91989	17.15944	15.83924
	AR	0.00117	0.00020	0.00077	0.00114	0.00024	0.00058	0.00080	0.00055	0.00015	0.00030	0.00048	0.00086	0.00059	0.00080	0.00029	0.00055	0.00085	0.00052	0.00056	0.00051
Tseday	AF	13.72121	8.45758	8.27121	20.46212	18.07121	28.20909	44.48182	48.92879	28.12879	18.07121	20.50758	8.27121	28.20909	41.06061	22.43485	35.55303	17.41818	14.97929	28.43758	30.69182
	SF	-17.18036	-7.38210	-13.59306	-14.32550	-6.31810	-5.92374	-8.88297	-6.28691	-2.14666	-8.54611	-10.72925	-17.23108	-5.98428	-7.57302	-7.55063	-9.61910	-12.60799	-8.96630	-9.69954	-7.21046
	AT	30.90157	15.83968	21.86427	34.78762	24.38931	34.13283	53.36479	55.21569	30.27545	26.61732	31.23682	25.50230	34.19337	48.63363	29.98547	45.17213	30.02617	23.94559	38.13711	37.90228
	AR	0.00100	0.00051	0.00071	0.00113	0.00079	0.00111	0.00173	0.00179	0.00098	0.00086	0.00101	0.00083	0.00111	0.00158	0.00097	0.00147	0.00098	0.00078	0.00124	0.00123
Kiremt	AF	21.22576	38.47727	19.80151	21.67727	65.16061	65.62727	92.78333	97.27273	40.16061	65.16061	53.35000	19.80151	65.62727	52.82576	56.74697	80.28636	36.02121	41.30202	66.35303	58.45000
	SF	-33.73628	-14.54405	-20.60127	-30.54413	-15.16106	-14.19050	-11.44491	-13.38030	-6.88048	-13.26017	-19.98690	-34.15932	-14.07675	-10.98041	-9.28316	-11.74704	-26.48049	-16.44527	-16.30557	-12.73432
	AT	54.96204	53.02132	40.40278	52.22140	80.32167	79.81778	104.22825	110.65302	47.04108	78.42078	73.33690	53.96084	79.70403	63.80617	66.03013	92.03340	62.50170	57.74729	82.65860	71.18432
	AR	0.00178	0.00172	0.00131	0.00170	0.00261	0.00259	0.00338	0.00359	0.00153	0.00255	0.00238	0.00175	0.00259	0.00207	0.00214	0.00299	0.00203	0.00188	0.00268	0.00231
Belg	AF	8.99697	10.40000	5.96818	14.48939	24.77576	30.31061	49.95606	62.06061	28.06667	24.77576	23.77121	5.96818	30.31061	38.68636	26.78333	41.81515	16.08737	15.55960	33.90879	32.53000
	SF	-15.25620	-7.73995	-12.17285	-14.85048	-8.39881	-8.01339	-9.56743	-7.74162	-2.00247	-9.05740	-11.53194	-15.36782	-8.14831	-7.52669	-7.34497	-8.54390	-12.83516	-9.30873	-9.81585	-7.55066
	AT	24.25317	18.13995	18.14103	29.33988	33.17456	38.32399	59.52349	69.80222	30.06913	33.83316	35.30315	21.33600	38.45891	46.21305	34.12830	50.35905	28.92254	24.86833	43.72463	40.08066
	AR	0.00079	0.00059	0.00059	0.00095	0.00108	0.00124	0.00193	0.00227	0.00098	0.00110	0.00115	0.00069	0.00125	0.00150	0.00111	0.00164	0.00094	0.00081	0.00142	0.00130

Those minimums for F_{Surf}, F_{Atm}, T_{Rate}, and the maximums for F_{TOA} are during the Bega season, while those minimums for F_{TOA}, maximums for F_{Surf}, F_{Atm}, and T_{Rate} are during the Kiremt season. Therefore, almost all of the results indicate extreme values at similar locales, like those of the observations in Figures 7.5, with a few noted exceptions. The results are similar to the findings and the reasons in the study (Liu et al., 2021) from eastern China. The seasonal results for the parameters were similar to those of the observations made in Austria (Yang et al., 2021), Algeria (Khan et al., 2021), eastern

China (Liu et al., 2021), and Hong Kong (Yu et al., 2022), despite the fact that there had been no prior studies on the sites in the clustered regions. The discrepancies we discovered were in the minimums with different data periods and site selections. Furthermore, in the study conducted by (Yu et al., 2022) the minimums were primarily at Bega and the maximums at the Kiremt seasons.

Table 7.2: The mean atmospheric and surface radiative forcing pattern [Aqua].

Sites		JB	AS	KD	AW	RG	AA	DG	TG	KC	ED	DT	BD	AB	AE	HR	DL	SW	SE	NW	NE
Bega	AF	18.30952	1.70952	11.44286	16.27460	6.06825	15.73175	12.98571	14.06349	3.04762	6.06825	11.51429	11.44286	15.73175	23.32540	5.12540	7.63810	13.55079	9.62804	9.93714	12.25143
	SF	-11.90889	-4.00077	-7.70810	-9.71521	-4.71818	-4.70498	-10.45702	-4.27969	-0.21723	-5.78479	-5.58341	-10.71906	-4.41376	-7.70609	-3.46934	-5.49113	-8.78076	-5.47129	-6.94198	-4.68232
	AT	30.21841	5.71030	19.15096	25.98981	10.78644	20.43673	23.44274	18.34318	3.26485	11.85304	17.09770	22.16192	20.14550	31.03148	8.59473	13.12922	22.33155	15.09933	16.87912	16.93375
	AR	0.00098	0.00019	0.00062	0.00084	0.00035	0.00066	0.00076	0.00060	0.00011	0.00038	0.00056	0.00072	0.00065	0.00101	0.00028	0.00043	0.00073	0.00049	0.00055	0.00055
Tseday	AF	10.96000	10.86167	9.19500	18.55833	27.93667	41.72500	43.53167	47.12500	19.21833	27.93667	37.47333	9.19500	41.72500	53.00000	27.16000	37.57833	19.15167	20.59389	30.98967	37.79900
	SF	-15.98806	-6.90777	-14.70560	-13.08689	-7.06127	-5.74008	-8.84596	-5.87609	-2.52002	-8.93310	-8.58990	-16.18343	-5.55332	-7.24664	-7.48014	-8.65557	-12.04541	-9.11781	-9.46374	-6.51309
	AT	26.94806	17.76943	23.90060	31.64522	34.99794	47.46508	52.37763	53.00109	21.73836	36.86977	46.06323	25.37843	47.27832	60.24664	34.64014	46.23390	31.19707	29.71170	40.45341	44.31209
	AR	0.00088	0.00058	0.00078	0.00103	0.00114	0.00154	0.00170	0.00172	0.00071	0.00120	0.00150	0.00082	0.00154	0.00196	0.00112	0.00150	0.00101	0.00096	0.00131	0.00144
Kiremt	AF	16.54444	39.42857	17.04127	18.85476	68.24444	65.68810	84.83571	82.41905	35.50635	68.24444	67.20397	17.04127	65.68810	62.24524	55.60794	83.12222	34.54788	40.71931	61.62968	62.75317
	SF	-31.79153	-14.37704	-24.41206	-29.39749	-16.01486	-13.14576	-11.29856	-11.87908	-6.46762	-13.58314	-17.91042	-32.41897	-13.59654	-10.87627	-8.95797	-10.65410	-25.73463	-17.31162	-15.62754	-11.90099
	AT	48.33598	53.80561	41.45333	48.25225	84.25931	78.83385	96.13427	94.29813	41.97396	81.82758	85.11438	49.46024	79.28463	73.12151	64.56591	93.77632	60.28251	58.03093	77.25723	74.65416
	AR	0.00157	0.00175	0.00135	0.00157	0.00274	0.00256	0.00312	0.00306	0.00136	0.00266	0.00276	0.00161	0.00257	0.00237	0.00210	0.00305	0.00196	0.00188	0.00251	0.00242
Belg	AF	7.35635	12.75079	9.87063	14.02381	34.40635	38.61191	49.62698	57.32540	19.71270	34.40635	33.06905	9.87063	38.61191	49.34762	28.33095	42.41746	18.59550	20.41111	35.91206	36.63175
	SF	-13.21147	-7.56710	-12.66958	-12.77111	-8.47623	-7.39614	-9.28202	-7.02963	-2.22285	-8.84136	-8.89064	-13.54952	-7.32019	-7.47655	-7.59316	-8.15845	-11.48627	-9.21094	-9.25914	-6.81374
	AT	20.56782	20.31789	22.54022	26.79491	42.88258	46.00804	58.90900	64.35503	21.93555	43.24771	41.95969	23.42015	45.93210	56.82417	35.92412	50.57591	30.08177	29.62205	45.17120	43.44548
	AR	0.00067	0.00066	0.00073	0.00087	0.00139	0.00149	0.00191	0.00209	0.00071	0.00140	0.00136	0.00076	0.00149	0.00185	0.00117	0.00164	0.00098	0.00096	0.00147	0.00141

Yearly Variation of Radiative Forcing

In this section, we summarize the total yearly variations of the aerosol particles radiative forcing parameters F_{Surf} and F_{Atm} for all the selected sites belonging to the four clustered regions. The first panel in the error bar Figures 7.7a indicates the yearly variations for the parameters F_{Surf} from the Terra and Aqua satellites, and the second panel represents the same with the F_{Atm} parameters corresponding to the selected sites in the southwest cluster, and the average of all the sites is also superimposed on all plots. Similarly, Figures 7.7b-7.7d produce yearly variations of the F_{Surf} and F_{Atm} parameters for the remaining three clustered regions. The majority of the sites, both in the western and eastern cluster zones, clearly demonstrate interannual variability with frequent minimum and maximum values for parameters, as repeated in the aforementioned figures.

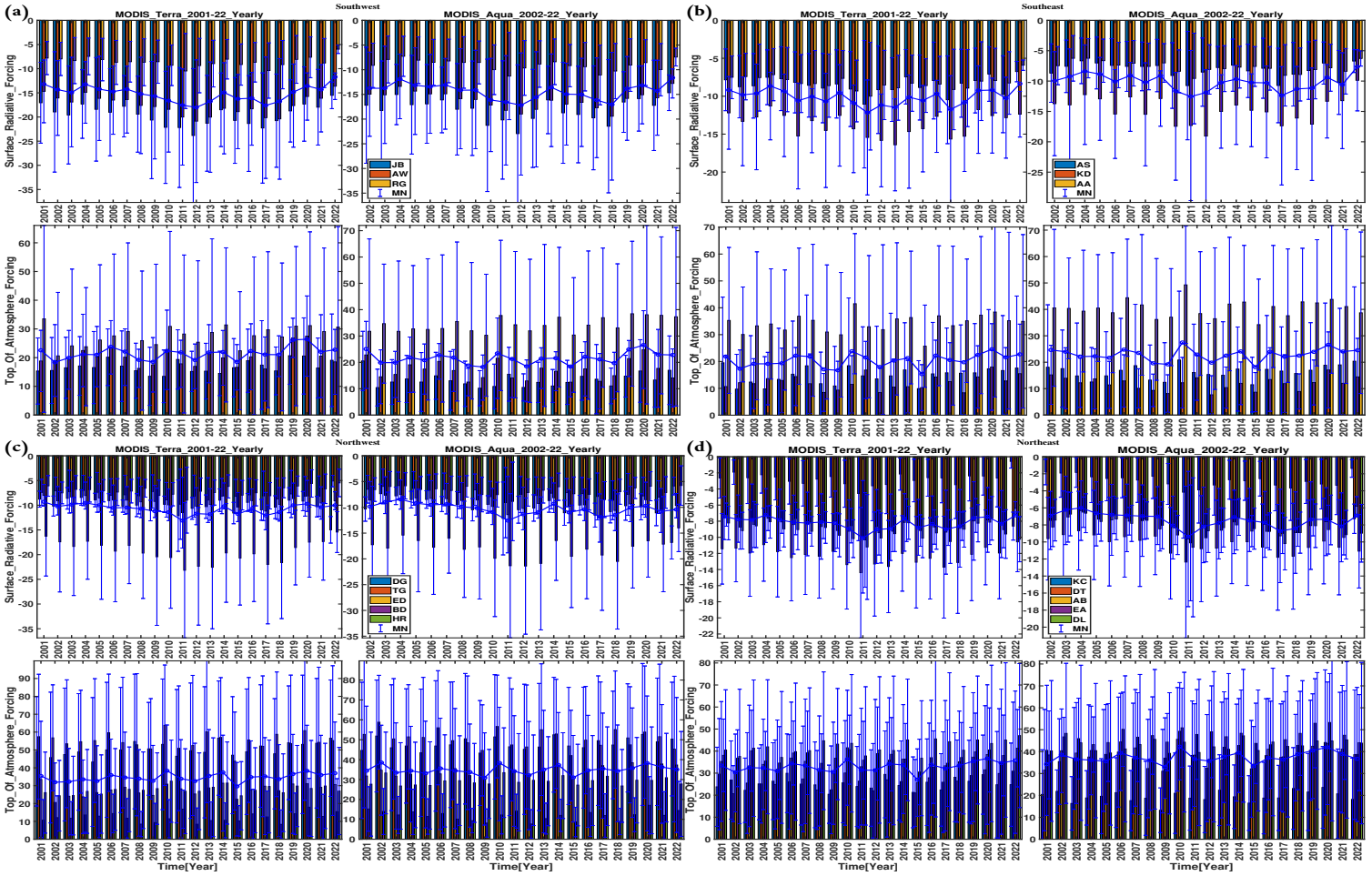

Figure 7.7: The atmospheric and surface radiative forcing yearly variation.

The average of the clustered regions shows minima in 2012 at the southwest cluster for all F_{Surf} and at the southeast cluster for F_{TOA}, with their maxima at the northwest cluster in 2022 for F_{Surf} and in 2010 for F_{TOA} from both instruments. Accordingly, the minimum values are -23.83 Wm^{-2} and 8.37 Wm^{-2} for Terra and -22.95 Wm^{-2} and 7.68 Wm^{-2} for Aqua, and the maxima are -0.58 Wm^{-2} and 63.80 Wm^{-2} for Terra and -1.37 Wm^{-2} and 58.83 Wm^{-2} for Aqua, respectively. Here, the values for all of the parameters we observed in the Terra satellite are mostly greater than those of the Aqua satellite. The values for the parameters were higher in the southern clusters, specifically in the southwest clusters, than in the northern clusters.

7.2.4 Optical Parameters Multiple Linear Regression

The performance of selected satellite-derived aerosol particles optical properties, cloud parametrs, outgoing long-wave radiation flux, and precipitation dataset was evaluated over East Africa-Ethiopia. In this study, the multiple linear regression analysis we discussed in Section 3.6.6 was carried out for each season based on variables with higher factor loading for the Terra and Aqua instruments. Here, the regression equations, respectively, for the Terra and Aqua instruments are expressed as:

$$\begin{aligned} \text{AOD} &= \beta_0 + \beta_1\text{AET} + \beta_2\text{AWV} + \beta_3\text{CFM} + \beta_4\text{PPT} + \beta_5\text{OLR} + \beta_6\text{CTP} + \beta_7\text{CTT}, \\ \text{AOD} &= \beta_0 + \beta_1\text{AET} + \beta_2\text{AWV} + \beta_3\text{CFM} + \beta_4\text{OLR} + \beta_5\text{CTP} + \beta_6\text{CTT}. \end{aligned} \tag{7.2.1}$$

Tables 7.3 and 7.4 present the results for the 16 chosen sites clustered into four regions, we have calculated using equation 7.2.1 for the Terra and Aqua instruments, respectively. In these tables, the mean cloud fraction CFM was less dominant, while the Ångström exponent AET was the most dominant variable with values $0.02733<\beta_1<15.17547$ in the regression equation. The study area regions showed the best performance values with $0.93941<\text{R}<0.99958$ for all the seasons.

The performance with $0.97064<\text{R}<0.99928$ and the dominance AET $0.04351<\beta_1<5.17874$ values are observed relatively minimally in Ethiopia at the Kombelcha site from both Terra and Aqua satellites in the Bega season. Their maximum values are observed in Djibouti at the Djibouti site for the performance and in South Sudan at the Juba site for the dominance variables from both instruments. For the Tseday season, the minimum with $0.99001<\text{R}<0.99958$ and AET $0.80674<\beta_1<7.86178$ values are still observed at the Kombolcha site, and the maximum values are observed at the Awassa site of Ethiopia for the performance and at the Juba site of South Sudan for the dominance of both instruments.

The performance $0.98531<\text{R}<0.99865$ and dominant AET $3.11914<\beta_1<15.17547$ values are observed relatively minimally in Ethiopia at the Kombolcha site from the Terra

Table 7.3: The regression results evaluated over the study cites and their clusters [Terra].

Sites		JB	AS	KD	AW	RG	AA	DG	TG	KC	ED	DT	BD	AB	AE	HR	DL	SW	SE	NW	NE
Bega	R	0.99739	0.99861	0.98888	0.99869	0.99840	0.99822	0.99726	0.99751	0.97064	0.99752	0.99928	0.99920	0.99895	0.99825	0.99082	0.99669	0.98472	0.98537	0.99202	0.93681
	R^2	0.99479	0.99722	0.97789	0.99737	0.99679	0.99644	0.99454	0.99502	0.94146	0.99505	0.99856	0.99840	0.99789	0.99651	0.98171	0.99338	0.96968	0.97094	0.98410	0.87705
	B0	-4.82599	-1.95297	-2.90073	-4.49740	-1.81107	-2.17464	-4.53412	-2.14866	0.48206	-2.56203	-3.21710	-4.63629	-2.28891	-3.34429	-1.18192	-2.82471	-5.38677	-2.35195	-3.19372	0.00704
	B1	5.17874	2.13126	3.64916	4.59315	1.99977	2.16140	4.32406	1.99736	0.04351	2.71170	3.14421	4.79506	2.21971	3.34668	1.63372	2.83708	4.24339	2.77642	2.62163	0.39332
	B2	-0.00457	-0.00160	-0.00863	-0.00002	-0.00319	-0.00224	-0.00779	0.00107	0.00943	-0.00568	0.00188	-0.00430	-0.00482	-0.00426	0.00751	-0.01237	0.01899	-0.01077	-0.05370	-0.14756
	B3	0.03020	0.02821	-0.02922	0.00786	-0.02198	-0.01901	0.04255	-0.01927	-0.09768	0.02403	-0.00154	0.00941	-0.00215	0.01522	-0.08669	0.00994	0.01889	-0.01151	0.30959	0.20340
	B4	0.00397	-0.01120	0.00570	0.00261	0.00462	0.00040	-0.00401	-0.00059	0.00569	0.01227	0.00045	0.00906	-0.00019	0.00337	-0.01559	-0.00443	-0.01086	0.00989	0.00048	0.02865
	B5	0.00060	0.00005	-0.00110	0.00003	-0.00048	-0.00046	0.00036	-0.00024	-0.00146	-0.00009	-0.00005	0.00022	-0.00022	-0.00001	-0.00078	-0.00035	0.00194	-0.00042	0.00110	-0.00307
	B6	0.00031	0.00011	0.00032	0.00013	-0.00001	-0.00013	-0.00011	-0.00018	0.00008	0.00006	-0.00003	0.00012	-0.00013	0.00006	0.00006	-0.00008	-0.00033	0.00022	0.00004	-0.00028
	B7	-0.00352	-0.00080	-0.00248	-0.00129	0.00003	0.00096	0.00020	0.00139	-0.00049	-0.00053	0.00029	-0.00172	0.00093	-0.00024	-0.00075	0.00061	0.00244	-0.00151	0.00112	0.00379
Tseday	R	0.99773	0.99714	0.99672	0.99958	0.99787	0.99782	0.99627	0.99749	0.99001	0.99888	0.99869	0.99811	0.99755	0.99130	0.99429	0.99863	0.98135	0.97654	0.98866	0.97207
	R^2	0.99546	0.99428	0.99345	0.99915	0.99573	0.99564	0.99256	0.99498	0.98011	0.99777	0.99739	0.99622	0.99511	0.98267	0.98861	0.99725	0.96305	0.95363	0.97744	0.94491
	B0	-8.36636	-2.93890	-7.65915	-6.83716	-2.60691	-2.59110	-3.39576	-2.49167	-1.14608	-3.60382	-4.69321	-7.35885	-2.56467	-3.95886	-3.26336	-3.89486	-5.56207	-3.53378	-3.61129	-2.15004
	B1	7.86178	3.01838	5.66388	6.26897	2.66821	2.50793	3.93878	2.62192	0.80674	3.76093	4.60947	7.12309	2.46779	3.11478	3.35868	4.18626	5.39390	4.07821	3.95822	2.12924
	B2	-0.01314	0.01488	-0.00507	-0.00996	0.00014	0.00317	0.00057	-0.00473	0.00227	0.00191	0.00212	-0.00641	-0.00308	-0.02622	0.01304	-0.00483	-0.01427	-0.02270	-0.02514	-0.00746
	B3	-0.05548	0.00349	0.26575	0.01624	0.01474	0.00365	-0.12629	0.04294	0.00297	-0.02831	-0.01570	0.01829	0.00651	-0.03606	0.00568	-0.05010	0.06933	0.09573	-0.06722	-0.27648
	B4	-0.01155	0.00457	0.01698	-0.00168	0.00175	0.00162	0.00328	0.00126	0.00484	0.00211	-0.00108	-0.00718	0.00143	-0.00254	0.00025	0.00326	0.00545	0.00213	0.01328	0.00291
	B5	0.00039	0.00020	0.00237	0.00000	0.00003	0.00014	-0.00205	-0.00013	0.00002	-0.00041	-0.00009	0.00008	0.00001	-0.00125	0.00028	-0.00072	0.00039	-0.00085	-0.00149	-0.00157
	B6	-0.00010	0.00006	-0.00061	-0.00016	0.00005	-0.00007	0.00030	0.00013	-0.00028	0.00008	0.00005	0.00008	-0.00009	-0.00061	0.00020	0.00015	0.00001	0.00028	-0.00001	-0.00053
	B7	-0.00009	-0.00085	0.00501	0.00130	-0.00036	0.00035	-0.00074	-0.00065	0.00210	-0.00063	-0.00027	-0.00104	0.00062	0.00611	-0.00134	-0.00103	-0.00053	-0.00196	0.00018	0.00348
Kiremt	R	0.99845	0.99346	0.99543	0.99764	0.99622	0.99614	0.99595	0.99628	0.98531	0.99530	0.99726	0.99865	0.99608	0.99383	0.99291	0.99299	0.99370	0.99449	0.99676	0.99391
	R^2	0.99690	0.98697	0.99088	0.99529	0.99245	0.99230	0.99191	0.99257	0.97083	0.99063	0.99452	0.99729	0.99218	0.98770	0.98586	0.98603	0.98743	0.98901	0.99354	0.98785
	B0	-15.10030	-6.16242	-10.25660	-16.99038	-8.62347	-7.81357	-4.23128	-5.87472	-3.63881	-7.39898	-10.04492	-17.59893	-6.30670	-4.70830	-3.78248	-4.99753	-14.66634	-7.97946	-9.40950	-6.21606
	B1	14.99690	6.67762	8.94890	13.17372	7.41175	6.88324	6.03874	6.48529	3.11914	6.58915	9.07290	15.17547	6.57664	5.35444	4.96162	5.78352	12.05913	7.30048	7.65194	5.80691
	B2	0.00276	-0.05242	-0.02005	0.00912	-0.00389	0.00683	0.02919	0.02120	-0.00591	-0.01316	0.00314	0.00237	0.00400	-0.00366	-0.01235	0.00196	0.01582	-0.02160	0.00406	0.00717
	B3	0.03339	0.33679	0.17652	0.16623	0.00921	0.13045	-0.04651	-0.11712	-0.06242	0.00535	-0.01127	-0.01476	0.02595	0.02214	0.11732	-0.06394	-0.02018	0.09336	-0.01479	-0.23199
	B4	0.00305	0.00863	0.00028	-0.01173	0.00507	0.00460	-0.00187	0.00252	-0.00554	0.00606	0.00057	0.00398	0.00268	0.00270	0.00228	-0.00019	0.00979	0.00362	-0.00664	0.00440
	B5	0.00047	0.00101	0.00015	0.00178	0.00004	0.00120	-0.00043	-0.00076	0.00041	-0.00003	-0.00009	0.00025	-0.00006	0.00001	0.00138	-0.00071	0.00084	0.00031	-0.00061	-0.00136
	B6	0.00063	0.00132	-0.00042	-0.00122	-0.00049	0.00002	0.00171	0.00063	-0.00033	0.00005	-0.00015	-0.00065	0.00060	0.00059	0.00122	0.00057	-0.00082	0.00011	-0.00017	-0.00027
	B7	-0.00808	-0.00686	0.00295	0.00935	0.00353	0.00031	-0.01117	-0.00412	0.00242	0.00176	0.00124	0.00362	-0.00376	-0.00465	-0.00901	-0.00446	0.00603	0.00036	0.00610	0.00280
Belg	R	0.99894	0.99932	0.99638	0.99944	0.99873	0.99902	0.99919	0.99838	0.97341	0.99843	0.99940	0.99923	0.99891	0.99930	0.99864	0.99876	0.99467	0.99235	0.99830	0.96111
	R^2	0.99789	0.99865	0.99278	0.99889	0.99747	0.99804	0.99839	0.99676	0.94753	0.99685	0.99881	0.99846	0.99783	0.99860	0.99728	0.99752	0.98938	0.98475	0.99659	0.92373
	B0	-7.64466	-3.58295	-5.12974	-6.93391	-3.70672	-3.51675	-4.31117	-3.24165	-1.13543	-4.34295	-5.28954	-7.14063	-3.52572	-3.42722	-3.15108	-3.82668	-6.22918	-3.53954	-4.13948	-3.42043
	B1	6.47635	3.41814	5.38812	6.44610	3.68950	3.55209	4.15201	3.36009	0.79291	4.11812	5.08811	6.62179	3.58780	3.34811	3.18343	3.78525	5.54723	4.37965	4.16398	2.00159
	B2	-0.00390	0.00008	-0.01270	0.00389	-0.00058	0.00504	0.00054	0.00044	-0.00171	-0.00251	0.00369	0.00911	-0.00257	0.00119	0.00002	-0.00092	-0.00194	0.00603	-0.01121	-0.00548
	B3	0.04240	0.00363	0.02226	-0.00891	0.02284	0.01875	-0.00582	-0.01581	-0.00870	0.01560	0.00787	0.01826	0.00587	-0.00554	0.00204	0.00629	0.05354	-0.03938	0.03692	0.05230
	B4	-0.00206	-0.00063	-0.00637	-0.00080	0.00055	0.00008	0.00015	0.00053	-0.00127	0.00195	0.00000	-0.00177	0.00032	0.00019	0.00003	0.00029	0.00086	-0.00537	-0.00139	-0.00311
	B5	0.00051	0.00012	0.00045	0.00014	0.00015	0.00039	0.00001	-0.00012	-0.00070	0.00004	0.00029	0.00047	0.00003	-0.00005	0.00005	0.00001	0.00053	0.00036	-0.00003	0.00010
	B6	-0.00037	-0.00006	0.00027	-0.00004	0.00007	0.00010	-0.00004	0.00009	-0.00020	-0.00004	0.00003	0.00000	0.00007	-0.00001	0.00004	0.00003	-0.00022	0.00054	0.00005	-0.00077
	B7	0.00327	0.00045	-0.00282	0.00033	-0.00051	-0.00101	0.00025	-0.00064	0.00274	0.00046	-0.00042	-0.00016	-0.00064	0.00020	-0.00037	-0.00021	0.00154	-0.00514	-0.00050	0.00724

and Aqua satellites in the Kiremt season. Their maximum values are also observed in Ethiopia at the Bahir Dar site from both instruments. For the Belg, the minimum with 0.97341<R<0.99944 and AET 0.79291<β_1<6.62179 values are still observed at the Kombolcha site, and the maximum values are observed at the Awassa site of Ethiopia for the performance and at the Juba site of South Sudan for the dominance from both instruments. Here, the performance and dominance of our results are better than in other studies such as (Symeonidis, 2017; Ngaina, 2015), respectively, where they were undergone over Europe and East Africa for PM 2.5.

Table 7.4: The regression results evaluated over the study cites and their clusters [Aqua].

Sites		JB	AS	KD	AW	RG	AA	DG	TG	KC	ED	DT	BD	AB	AE	HR	DL	SW	SE	NW	NE
Bega	R	0.99845	0.99790	0.99432	0.99778	0.99714	0.99847	0.99266	0.99749	0.93941	0.99429	0.99900	0.99841	0.99878	0.99531	0.99490	0.99609	0.99110	0.99581	0.99149	0.96469
	R^2	0.99690	0.99581	0.98868	0.99557	0.99429	0.99693	0.98538	0.99500	0.88109	0.98861	0.99800	0.99682	0.99756	0.99064	0.98982	0.99220	0.98228	0.99163	0.98305	0.93063
	B0	-5.34259	-1.67718	-3.60456	-4.11376	-1.87003	-1.79909	-3.73065	-1.82121	-0.06997	-1.95835	-2.26812	-4.58216	-1.64927	-2.61401	-1.01113	-1.30254	-4.73196	-2.85550	-2.26374	-1.13829
	B1	4.98516	1.84179	3.09732	4.05357	2.03633	1.98948	4.22418	1.84714	0.02733	2.45520	2.37187	4.51833	1.84093	3.01423	1.48000	2.13159	3.56603	2.17247	2.34129	0.45532
	B2	0.01581	0.00283	0.00424	0.00118	0.00349	-0.02565	-0.02255	0.00131	0.00187	0.01131	-0.00607	0.00242	-0.01561	-0.00083	0.01002	0.00151	0.02418	-0.00797	-0.02872	-0.11799
	B3	-0.01354	0.03075	0.06199	-0.01046	0.06577	0.02325	0.06700	-0.04223	-0.01256	0.00043	0.00475	-0.00464	0.01903	-0.00896	-0.04920	-0.05916	0.00456	0.12876	0.26276	0.25464
	B4	0.00124	0.00009	0.00085	0.00019	0.00032	-0.00045	0.00073	-0.00029	-0.00014	-0.00050	-0.00008	0.00011	-0.00035	-0.00016	-0.00052	-0.00111	0.00256	0.00137	0.00146	-0.00081
	B5	-0.00002	0.00010	-0.00015	0.00000	0.00012	-0.00003	0.00012	-0.00017	-0.00014	0.00026	-0.00004	0.00005	0.00000	0.00024	0.00015	0.00027	-0.00044	-0.00016	0.00033	-0.00046
	B6	-0.00077	-0.00076	0.00115	-0.00035	-0.00111	0.00010	-0.00315	0.00083	0.00069	-0.00190	-0.00009	-0.00057	-0.00008	-0.00189	-0.00129	-0.00229	0.00232	0.00152	-0.00245	0.00546
Tseday	R	0.99753	0.99753	0.99168	0.99860	0.99836	0.99685	0.99675	0.99832	0.98578	0.99627	0.99870	0.99805	0.99719	0.99091	0.99614	0.99830	0.99578	0.98546	0.99132	0.98167
	R^2	0.99507	0.99507	0.98342	0.99719	0.99672	0.99371	0.99350	0.99664	0.97177	0.99255	0.99741	0.99611	0.99439	0.98190	0.99229	0.99661	0.99158	0.97114	0.98271	0.96368
	B0	-7.87869	-2.72318	-8.53618	-5.77910	-2.56453	-2.27902	-2.88333	-2.14561	-0.70641	-3.36053	-3.67454	-7.10334	-2.16669	-2.90725	-2.79396	-3.58520	-4.62322	-5.28573	-3.20552	-3.01507
	B1	7.27081	3.12531	5.99488	5.60832	3.06257	2.44113	3.66860	2.46264	0.89413	3.87065	3.67735	6.82893	2.32231	3.03430	3.40547	3.69811	4.95218	4.43743	3.95971	2.32607
	B2	-0.01505	0.00827	-0.00722	-0.00437	0.00138	-0.00789	-0.00084	-0.00246	0.01068	0.00323	0.00588	-0.00617	-0.00435	-0.04992	0.01393	0.00056	0.00296	0.04885	0.00609	-0.03452
	B3	-0.02039	-0.05512	0.09671	0.00101	0.04269	0.00670	-0.21137	0.02531	-0.03538	-0.01440	0.00837	-0.02337	-0.02900	-0.22860	-0.04698	-0.04224	-0.00993	0.23114	-0.15165	-0.06753
	B4	-0.00036	-0.00088	0.00096	0.00003	0.00003	-0.00026	-0.00193	-0.00039	-0.00012	-0.00033	0.00025	-0.00030	-0.00037	-0.00237	0.00003	-0.00048	0.00153	0.00238	-0.00049	-0.00113
	B5	-0.00013	0.00017	-0.00103	0.00002	0.00043	0.00009	0.00024	0.00025	0.00002	0.00039	0.00007	0.00007	0.00003	-0.00048	0.00045	0.00005	0.00022	0.00021	0.00025	-0.00073
	B6	0.00135	-0.00100	0.00950	-0.00039	-0.00288	-0.00040	-0.00127	-0.00126	-0.00038	-0.00271	-0.00070	-0.00028	-0.00006	0.00393	-0.00348	-0.00025	-0.00395	-0.00087	-0.00295	0.00585
Kiremt	R	0.99683	0.99281	0.99423	0.99669	0.99504	0.99391	0.99214	0.99479	0.98945	0.99304	0.99611	0.99749	0.99546	0.99273	0.98977	0.99399	0.99525	0.99565	0.99226	0.98998
	R^2	0.99367	0.98567	0.98850	0.99339	0.99010	0.98786	0.98435	0.98960	0.97902	0.98613	0.99224	0.99498	0.99095	0.98550	0.97964	0.98802	0.99053	0.99131	0.98458	0.98006
	B0	-14.45146	-6.54261	-9.90992	-13.81813	-8.17245	-6.32625	-5.45678	-6.11586	-0.92156	-6.58728	-6.57624	-16.10623	-7.01182	-4.37424	-4.34938	-3.85918	-12.88182	-7.42426	-7.87745	-5.06057
	B1	13.62305	6.90159	10.90797	12.65190	7.67963	6.26453	6.04307	6.09746	3.07604	6.61075	7.99529	14.72187	6.64147	5.49976	5.07697	5.52691	12.06861	8.10709	7.41057	5.59690
	B2	0.02169	-0.00894	0.00215	-0.01037	0.00385	-0.01669	0.03923	0.03141	-0.02420	0.00262	0.01650	0.00384	0.04207	-0.01025	-0.00936	-0.02074	0.09199	-0.01499	0.04449	0.02066
	B3	-0.00538	0.05921	-0.08090	0.33905	-0.03561	0.01382	0.01662	-0.21396	-0.13329	0.00092	-0.01122	-0.14617	-0.13910	0.01995	0.03800	0.13046	-0.68010	0.10328	-0.01651	-0.19029
	B4	0.00101	0.00145	0.00075	0.00118	0.00003	-0.00062	0.00102	-0.00058	-0.00179	0.00059	0.00046	0.00001	-0.00090	-0.00045	0.00058	0.00174	0.00005	0.00035	0.00052	-0.00047
	B5	0.00007	0.00068	0.00084	0.00077	0.00028	0.00040	0.00082	0.00011	0.00076	0.00042	0.00158	-0.00011	0.00024	0.00086	0.00087	0.00168	-0.00038	0.00107	0.00039	0.00048
	B6	-0.00377	-0.00561	-0.00991	-0.00372	-0.00058	-0.00110	-0.00654	-0.00043	-0.00729	-0.00291	-0.01109	-0.00052	0.00031	-0.00650	-0.00567	-0.01214	-0.00026	-0.00716	-0.00172	-0.00323
Belg	R	0.99770	0.99949	0.99631	0.99927	0.99868	0.99846	0.99827	0.99638	0.98533	0.99685	0.99902	0.99915	0.99802	0.99943	0.99811	0.99850	0.99792	0.98309	0.99821	0.97083
	R^2	0.99541	0.99897	0.99263	0.99853	0.99736	0.99693	0.99654	0.99277	0.97088	0.99371	0.99804	0.99830	0.99604	0.99885	0.99622	0.99700	0.99585	0.96648	0.99642	0.94251
	B0	-6.33808	-3.49903	-6.02668	-5.74312	-3.73582	-3.19301	-3.87011	-3.06604	-0.90965	-4.04028	-4.00923	-5.86336	-3.39928	-3.35704	-3.76168	-3.62088	-4.09813	-3.78074	-3.41053	-3.51564
	B1	5.79678	3.29637	5.65792	5.61530	3.75735	3.31458	3.97587	3.07842	0.84766	4.02052	3.98536	5.78415	3.30233	3.24009	3.46893	3.77003	4.86638	4.22298	4.10235	2.33306
	B2	-0.00526	-0.00049	-0.00061	0.00399	0.00348	0.00417	-0.00032	0.00421	0.02047	0.00548	0.00349	-0.00175	0.00536	0.00701	-0.00405	0.00594	-0.00331	0.03758	0.00732	0.01675
	B3	0.00680	0.00928	-0.04424	0.01093	0.01353	0.04013	0.00186	0.02075	-0.01174	-0.01185	0.02172	0.02258	0.01337	0.00298	-0.01488	0.01693	0.05853	-0.08807	-0.08348	0.11284
	B4	0.00002	0.00018	0.00008	0.00011	0.00022	0.00033	0.00042	-0.00010	-0.00017	0.00007	0.00046	0.00012	0.00036	0.00028	-0.00038	0.00049	0.00066	0.00090	0.00010	0.00178
	B5	-0.00017	-0.00009	-0.00020	0.00012	0.00010	0.00026	0.00011	0.00010	-0.00002	0.00005	0.00009	0.00010	0.00000	-0.00003	-0.00017	0.00020	0.00058	0.00025	0.00027	-0.00040
	B6	0.00136	0.00064	0.00076	-0.00097	-0.00085	-0.00155	-0.00138	-0.00030	0.00050	-0.00052	-0.00096	-0.00114	-0.00020	0.00002	0.00173	-0.00185	-0.00555	-0.00372	-0.00356	0.00336

7.3 Conclusions

The purpose of this research is to investigate the radiative forcing of aerosol particles and the correlation with precipitation and cloud parameters based on the spatiotemporal distribution variations. They are retrieved from the MODIS, TRMM 3B43, and CERES sensors over a period of 22 years (for Terra: January 2001 to December 2022, and for Aqua: July 2002 to December 2022). Those parameter retrievals included the spatial, temporal, monthly, seasonal and yearly values at sixteen selected sites clustered in four regions with their corresponding averages. The main conclusions drawn from our research work are as follows:

1. The seasonal total spatial correlations show slight variations ranging between -1.0 and 1.0. They have minimums in the Bega season and maximums in the Kiremt season; their minimums are mostly in 33–42°E and maximums in the southwest of the study area regions {3–18^0 N, 24–48^0 E}, across the globe we consider it.

2. Minimum values for temporal corelations are found at Kebri Dahar for AOD and AET, at Kombolcha for AWV, and at Humera for CFM and PPT, all in January and December. Their maximums are AOD and AET at Aseb, AWV at Tonga, CFM at Agnuak, and PPT at Bahir Dar, all in July. Minimum OLR values were found at Humera and CTP at Bahir Dar, both in August, and CTT at Raga in March and April. Their maximum OLR value is at Kebri Dahar in February; the maximum CTP value is at Dahlak in January and December; and the maximum CTT value is at Dahlak in November. The minimum values for the OLR are set at the Bahir Dar and Ethiopian Renascence Dam sites in July and August, respectively.

3. The minimum monthly radiative forcing values observed are in the northwest cluster for F_{Surf} and in the southeast cluster for F_{TOA}, while the maximum values for F_{Surf} are in the northeast and for F_{TOA} in the northwest cluster from both instruments. For Terra, the minimum values of F_{Surf} and F_{TOA} were found to be -39.17 and 1.01 Wm^{-2} in July and December, while the maximum values were to be -0.22 and 109.30 Wm^{-2} in January and July. Moreover, Aqua also shows similar results, with the minimum F_{Surf} and F_{TOA} values observed during July and December, -36.56 and 1.17 Wm^{-2}, while the maximum values in October and August at the two clusters are -0.64 and 93.80 Wm^{-2}. The minimum values are at Bahir Dar for F_{Surf} and at Awassa for F_{TOA}, both in Ethiopia, while the maximum values are in Ethiopia at Kombolcha for F_{Surf} and for F_{TOA} at Tonga in South Sudan.

4. The minimum seasonal radiative forcing values found at Bahir Dar for F_{Surf} are -34.16 and -32.41 Wm^{-2} in the northwest cluster, at Awassa for F_{TOA} are -4.88 and

-4.72 Wm^{-2} in the southwest cluster, while the maximum values found at Komolcha for F_{Surf} are -0.30 and -0.22 Wm^{-2} in the northeast cluster, and for F_{TOA} are around 97.27 Wm^{-2} at Tonga and 92.78 Wm^{-2} at Dangote in the northwest cluster. The minimum values found at Kombolcha for F_{Atm} are -4.73 and 3.26 Wm^{-2}; for T_{Rate} are 0.0002 K/s and 0.0001 K/s; they are all in the southwest cluster, while the maximum values found at Tonga site for F_{Atm} are 110.65 and 96.13 Wm^{-2}; and for T_{Rate} are around 0.0036 K/s and 0.0031 K/s; all are in the northwest cluster. The minimums for F_{Surf}, F_{Atm}, T_{Rate}, and the maximums for F_{TOA} are during the Bega season, while those minimums for F_{TOA}, maximums for F_{Surf}, F_{Atm}, and T_{Rate} are during the Kiremt season.

5. The total annual average radiative forcing shows the minimum values in 2012 at the southwest cluster for all F_{Surf} and at the southeast cluster for F_{TOA}. While their maximums are at the northwest cluster in 2022 for F_{Surf} and in 2010 for F_{TOA} from both Terra and Aqua instruments. The minimum values are -23.83 and 8.37 Wm^{-2} for Terra and -22.95 and 7.68 Wm^{-2} for Aqua, and the maxima are -0.58 and 63.80 Wm^{-2} for Terra and -1.37 and 58.83 Wm^{-2} for Aqua, respectively. The values for all of the parameters observed on the Terra satellite are mostly higher than those on the Aqua satellite. The parameter values were higher in the southern clusters, specifically the southwest clusters, than in the northern clusters.

6. The mean cloud fraction was less dominant, while the Ångström exponent was the most dominant, with $0.02733<\beta_1<15.17547$ in the regression analysis. The study area regions showed the best performance with $0.93941<R<0.99958$ for all the seasons. The minimum values observed in Bega at Kombolcha are from Aqua for both β_1 and R, while their maximums are from Terra in Kiremt at Bahir Dar for the dominance and in Tseday at Agnuak for the performance.

Chapter 8

SUMMARY AND CONCLUSIONS

This chapter contains summaries of the entire PhD research, main conclusions from the thesis study findings, and recommendations for future work.

8.1 Summary

Atmospheric aerosol particles are liquid-solid particulate matter PM that are suspended in the atmosphere with a diameter of 0.001–100 micrometers. Aerosol particles have a significant impact on the atmospheric energy balance, environment, air quality, climate dynamics, and human life. Therefore, effective monitoring of atmospheric aerosols can help to provide an important understanding of aerosol optical and physical characteristics, aerosol radiative forcings, and aerosol air pollution control.

The purpose of this PhD study is to determine the spatio-temporal distribution variability of aerosol particles and their effects on the radiation budget over East Africa-Ethiopia. The aerosol optical properties, cloud parametes, precipitation, and radiation budget that have not been studied yet were retrieved from daily-monthly MODIS, CERES, and TRMM satellite data over a period of 22 years, for Terra: January 2001 to December 2022, and for Aqua: July 2002 to December 2022. Those parameters included the daily, monthly, seasonal, and yearly AOD, AET, AWV, CFM, PPT, OLR, CPT, and CTT temporal values at sixteen selected sites clustered in four regions with their corresponding averages.

The study has used different data analysis techniques, which include the kernel density distribution estimator, the Mann-Kendall statistic trend test, the principal component analysis, the Fire-Map model, the HYSPLIT trajectory analysis, correlation analysis, and multiple linear regression analysis. Moreover, the aerosol radiative forcings, which are the surface radiative forcing, TOA surface radiative forcing, and net atmospheric forcing, were calculated. The next section will draw the main conclusions from our work.

8.2 Conclusions

The daily minimum temporal AOD and AE values were observed in the southeast cluster at the Kebri Dahar site, and the maximum AOD and AE values were in the northeast cluster at the Erta Ale site, both of which were observed in Ethiopia. The minimum monthly values are found at the Kebri Dahar site for AOD and AET, at the Kombolcha site for AWV, at the Humera site for both CFM and PPT, they all in January and December, while their maximum values are AOD at the Aseb siet, AWV at the Tonga site, CFM at the Agnuak sie, and PPT at the Bahir Dar site, they all in July; the minimum values were found for OLR at the Humera site and CTP at the Bahir Dar site both in August and CTT at the Raga site in March and April, while the maximum OLR value is at the Kebri Dahar site in February; the maximum CTP value is at the Dahlak site in January and December; the maximum CTT value is at the Dahlak site in November.

The aerosol particle types have been classified by applying gaussian forms of the kernel density distribution techniques, and the Mann-Kendall rank trend test was applied over 16 sites in four classified clusters to check the annual variability of optical parameters of aerosol. The most dominant type of particle was maritime aerosol particles, with desert dust particles in second place. Aerosol particles were at their highest density in the northwest cluster at the Humera site during Bega and at their lowest levels mostly in the northeast cluster at the Juba site in the Kiremt season. The yearly total forward trend

of aerosol particles was almost increasing, and the reverse was vice versa. The variations shown in the trend were lowest in the northwest cluster and highest in the northeast.

From the results of this dissertation, spatial distribution of the aerosol optical properties AOD and AET, the cloud parameters AWV, CFM, CTP, and CTT, the correlation values COA, COV, COF, COP, COT, precipitation PPT, and the radiation OLR flux exhibit minimum values during the Bega seasons and maximums during the Kiremt seasons. The parameters are more oriented toward the southwest. The aerosol optical properties AOD and AET demonstrate the lowest distribution values in the years 2002–2003, with maximums in 2001, 2008, and 2015 in interannual spatial distribution fluctuations.

The OLR and AWV parameters, both at the Humera and Dahlak sites, had the lowest optimum significant PCs, whereas the PCs retained based on AET at the Awassa site and AWV at the Dangote site were the highest compared to the other parameters. The differences in retained PCs point to the different atmospheric dynamics responsible for the behaviour of climate during the various seasons of the year and the spatial coherence arising from both interannual and intraseasonal variability. Further, our observation using the HYSPLIT model and fire map confirms that transported aerosol particles in the atmosphere show varied source regions, mostly the Arebian desert and the southwest Indean ocean, at different levels.

The lowest monthly radiative forcing values for F_{Surf} and F_{TOA} are in the northwest and southeast clusters, respectively, while the highest values from both sensors for F_{Surf} are in the northeast and for F_{TOA} in the northwest cluster. For the Terra satellite, the minimum values of F_{Surf} and F_{TOA} were found in July and December, while the maximum values were in January and July. Moreover, the Aqua satellite also shows similar results, with the minimum F_{Surf} and F_{TOA} values observed during July and December and the maximum values in October and August at the two clusters, respectively. The minimum values are at Bahir Dar for F_{Surf} and at Awassa for F_{TOA}, both in Ethiopia, while the maximum values are in Ethiopia at Kombolcha for F_{Surf} and for F_{TOA} at Tonga in South Sudan.

The minimum seasonal F_{Surf} values are found at Bahir Dar in the northwest cluster and for F_{TOA} at Awassa in the southwest cluster, while the maximum values found at Komolcha for F_{Surf} in the northeast cluster and for F_{TOA} at Tonga and at Dangote in the northwest cluster. The minimum F_{Atm} and T_{Rate} values found at Kombolcha in the southwest cluster, while the maximum values found at Tonga in the northwest cluster. The minimums for F_{Surf}, F_{Atm}, T_{Rate}, and the maximums for F_{TOA} are during the Bega season, while those minimums for F_{TOA}, maximums for F_{Surf}, F_{Atm}, and T_{Rate} are during the Kiremt season. In 2012 minim F_{Surf} and F_{TOA} are situated near the southeast cluster and southwest cluster from total annual average radiative forcing. Their maxima are located at the northwest cluster in 2022 and 2010, respectively. Most of the parameters exhibit a higher magnitude from the Terra satellite than those from the Aqua satellite. In comparison to the northern clusters, the values for the parameters were greater in the southern clusters, more precisely in the southwest clusters. In the regression analysis, the most dominant variable was the AET, while the CFM was less dominant.

8.3 Recommendations

When this doctoral dissertation data was analyzed, we discovered some limitations in the studies, which is why the authors recommend future studies to overcome these limitations.

1. Forest fires and volcano aerosol particles in East Africa-Ethiopia are higher due to their geographical location; their effects are so huge in the regions that are not well studied, measured, and reported. So, the authors recommended that research be done to analyze forest fire and volcanic aerosol particles loading in the East Africa-Ethiopia sectors.

2. Understanding the structure of the atmosphere is important because the vertical distribution variation of aerosol particles influences the radiative budget and surface

air quality. Therefore, the authors recommended future studies that describe the vertical distribution of atmospheric aerosol particles over East Africa-Ethiopia.

3. The topographic effects of the differential terrain illumination in the optical satellite imagery of rugged mountainous regions have serious consequences for qualitative and quantitative analysis for various applications. Henceforth, future works should focus on studying the effects of topography on the aerosol particles distribution using MODIS satellite and regional model simulations over East Africa-Ethiopia.

4. Aerosol particles are an integral part of Earth's climate system, and their effect on climate makes this field a relevant research problem. The artificial neural network ANN technique is an upcoming technique in different research fields that is used to predict the future. So, we want to recommend the investigation of artificial neural network performance in the retrieval of aerosol properties over East Africa-Ethiopia.

Generally, further research on aerosol particles and cloud parameters should include the impact of altitude, topographical, meteorological, hydrological, and agricultural factors on the ocean-atmosphere interaction with appropriate correction methods. The approach of developing regional climate models considering aerosol paricles indices for characterizing, monitoring, and prediction could show the way forward in developing monitoring and early climatic warning baselines for East Africa-Ethiopia.

References

Abdullah, S., Ismail, M., and Fong, S. Y.: Multiple linear regression (MLR) models for long term PM10 concentration forecasting during different monsoon seasons, Journal of Sustainability Science and Management, 12, 60–69, 2017.

Ackerman, A. S., Toon, O., Stevens, D., Heymsfield, A., Ramanathan, V., and Welton, E.: Reduction of tropical cloudiness by soot, Science, 288, 1042–1047, 2000.

Adesina, J. A.: Aerosol characteristics over different regions of southern Africa: using sunphotometer and satellite measurements., Ph.D. thesis, School of Chemistry and Physics, University of KwaZulu-Natal, Durban, 2015.

Aga, M. T.: Climate and Seasons in Ethiopia, Ethiopia's First and Largest Blog Network, `https://allaboutethio.com/tclimate.html`, [Online; accessed 19-July-2023], 2023.

Ahmad, I., Tang, D., Wang, T., Wang, M., and Wagan, B.: Precipitation trends over time using Mann-Kendall and spearman's rho tests in swat river basin, Pakistan, Advances in Meteorology, 2015, 2015.

Ahmad, M., Alam, K., Tariq, S., Anwar, S., Nasir, J., and Mansha, M.: Estimating fine particulate concentration using a combined approach of linear regression and artificial neural network, Atmospheric Environment, 219, 117 050, 2019.

Ali, G., Bao, Y., Ullah, W., Ullah, S., Guan, Q., Liu, X., Li, L., Lei, Y., Li, G., and Ma,

J.: Spatiotemporal trends of aerosols over urban regions in Pakistan and their possible links to meteorological parameters, Atmosphere, 11, 306, 2020.

Anderson, T., Charlson, R., Bellouin, N., Boucher, O., Chin, M., Christopher, S., Haywood, J., Kaufman, Y., Kinne, S., Ogren, J., et al.: An "A-Train" strategy for quantifying direct aerosol forcing of climate, Bull. Am. Met. Soc, 86, 1795–1809, 2005.

Anderson, T. L., Charlson, R. J., Schwartz, S. E., Knutti, R., Boucher, O., Rodhe, H., and Heintzenberg, J.: Climate forcing by aerosols–a hazy picture, Science, 300, 1103–1104, 2003.

Apollo, A. and Mbah, M. F.: Challenges and opportunities for climate change education (Cce) in East Africa: A critical review, Climate, 9, 93, 2021.

Arfin, T., Pillai, A. M., Mathew, N., Tirpude, A., Bang, R., and Mondal, P.: An overview of atmospheric aerosol and their effects on human health, Environmental Science and Pollution Research, 30, 125 347–125 369, 2023.

Augustine, J. A., Hodges, G. B., Dutton, E. G., Michalsky, J. J., and Cornwall, C. R.: An aerosol optical depth climatology for NOAA's national surface radiation budget network, Journal of Geophysical Research: Atmospheres, 113, 2008.

Ayanlade, A., Atai, G., and Jegede, M. O.: Spatial and seasonal variations in atmospheric aerosols over Nigeria: assessment of influence of intertropical discontinuity movement, Journal of Ocean and Climate, 9, 1759313118820 306, 2019.

B AL-Taie, K., Rajab, J. M., and Al-Salihi, A. M.: Climatology and classification of aerosols based on optical properties over selected stations in Iraq, in: AIP Conference Proceedings, vol. 2290, AIP Publishing, 2020.

Bai, H., Wang, M., Zhang, Z., and Liu, Y.: Synergetic Satellite Trend Analysis of Aerosol

and Warm Cloud Properties over Ocean and Its Implication for Aerosol-Cloud Interactions, Journal of Geophysical Research: Atmospheres, 125, e2019JD031 598, 2020.

Balsamo, G., Agusti-Parareda, A., Albergel, C., Arduini, G., Beljaars, A., Bidlot, J., Blyth, E., Bousserez, N., Boussetta, S., Brown, A., et al.: Satellite and *in situ* observations for advancing global Earth surface modelling: A Review, Remote Sensing, 10, 2038, 2018.

Balsamo, G., Agusti-Panareda, A., Albergel, C., Arduini, G., Beljaars, A., Bidlot, J., Blyth, E., Bousserez, N., Boussetta, S., Brown, A., et al.: Correction: Balsamo, G., et al. Satellite and *In Situ* Observations for Advancing Global Earth Surface Modelling: A Review. Remote Sensing 2018, 10, 2038, Remote Sensing, 11, 941, 2019.

Barnsley, M.: Digital remotely-sensed data and their characteristics, Geographical Information Systems, 1, 451–466, 1999.

Barthlott, C. and Hoose, C.: Aerosol effects on clouds and precipitation over central Europe in different weather regimes, Journal of the Atmospheric Sciences, 75, 4247–4264, 2018.

Behera, S.: Estimation of Aerosol Optical Depth using MODIS satellite data and its relation with particulate matter concentration in the mining regions, Ph.D. thesis, National Institute of Technology Rourkela, 2016.

Benkovitz, C. M., Berkowitz, C. M., Easter, R. C., Nemesure, S., Wagener, R., and Schwartz, S. E.: Sulfate over the North Atlantic and adjacent continental regions: Evaluation for October and November 1986 using a three-dimensonal model driven by observation-derived meteorology, Journal of Geophysical Research: Atmospheres, 99, 20 725–20 756, 1994.

Blanchard, D. C. and Woodcock, A. H.: The production, concentration, and vertical

distribution of the sea-salt aerosol, Annals of the New York Academy of Sciences, 338, 330–347, 1980.

Boiyo, R., Kumar, K. R., and Zhao, T.: Optical, microphysical and radiative properties of aerosols over a tropical rural site in Kenya, East Africa: source identification, modification and aerosol type discrimination, Atmospheric environment, 177, 234–252, 2018a.

Boiyo, R., Kumar, K. R., and Zhao, T.: Spatial variations and trends in AOD climatology over East Africa during 2002–2016: a comparative study using three satellite data sets, International Journal of Climatology, 38, e1221–e1240, 2018b.

Boiyo, R., Kumar, K. R., Zhao, T., and Guo, J.: A 10-year record of aerosol optical properties and radiative forcing over three environmentally distinct AERONET sites in Kenya, East Africa, Journal of Geophysical Research: Atmospheres, 124, 1596–1617, 2019.

Breitner-Busch, S., Mücke, H.-G., Schneider, A., and Hertig, E.: Impact of climate change on non-communicable diseases due to increased ambient air pollution, Journal of Health Monitoring, 8, 103, 2023.

Briffa, J., Sinagra, E., and Blundell, R.: Heavy metal pollution in the environment and their toxicological effects on humans, Heliyon, 6, e04 691, 2020.

Bryhn, A. C. and Dimberg, P. H.: An operational definition of a statistically meaningful trend, PLoS One, 6, e19 241, 2011.

Buis, A.: Steamy relationships: How atmospheric water vapor amplifies earth's greenhouse effect, Ask NASA Climate: NASA, 2022.

Bulmer, M.: The statistical analysis of density dependence, Biometrics, pp. 901–911, 1975.

Burrows, J. P., Platt, U., and Borrell, P.: The remote sensing of tropospheric composition from space, Springer Science & Business Media, 2011.

Charlson, R. J., Lovelock, J. E., Andreae, M. O., and Warren, S. G.: Oceanic phytoplankton, atmospheric sulphur, cloud albedo and climate, Nature, 326, 655–661, 1987.

Charlson, R. J., Schwartz, S., Hales, J., Cess, R. D., Coakley Jr, J., Hansen, J., and Hofmann, D.: Climate forcing by anthropogenic aerosols, Science, 255, 423–430, 1992.

Charlson, R. J., Ackerman, A. S., Bender, F. A.-M., Anderson, T. L., and Liu, Z.: On the climate forcing consequences of the albedo continuum between cloudy and clear air, Tellus B: Chemical and Physical Meteorology, 59, 715–727, 2007.

Chen, T., Liu, Y., Ma, Q., Chu, B., Zhang, P., Liu, C., Liu, J., and He, H.: Significant source of secondary aerosol: formation from gasoline evaporative emissions in the presence of SO_2 and NH_3, Atmospheric Chemistry and Physics, 19, 8063–8081, 2019.

Chen, X., Ding, J., Wang, J., Ge, X., Raxidin, M., Liang, J., Chen, X., Zhang, Z., Cao, X., and Ding, Y.: Retrieval of fine-resolution aerosol optical depth (AOD) in semiarid urban areas using Landsat data: A case study in Urumqi, NW China, Remote Sensing, 12, 467, 2020.

Chi, Y., Zuo, S., Ren, Y., and Chen, K.: The spatiotemporal pattern of the aerosol optical depth (AOD) on the canopies of various forest types in the exurban national park: a case in ningbo city, eastern China, Advances in Meteorology, 2019, 1–12, 2019.

Christopher, S. A. and Zhang, J.: Shortwave aerosol radiative forcing from MODIS and CERES observations over the oceans, Geophysical Research Letters, 29, 6–1, 2002.

Christopher, S. A., Kliche, D. V., Chou, J., and Welch, R. M.: First estimates of the radiative forcing of aerosols generated from biomass burning using satellite data, Journal of Geophysical Research: Atmospheres, 101, 21 265–21 273, 1996.

Chrysoulakis, N. and Cartalis, C.: Improving the estimation of land surface temperature for the region of Greece: adjustment of a split window algorithm to account for the distribution of precipitable water, International Journal of Remote Sensing, 23, 871–880, 2002.

Chu, E. and Karr, J.: Environmental impact: Concept, consequences, measurement, Reference Module in Life Sciences, 2017.

Chung, S. Y., Venkatramanan, S., Elzain, H. E., Selvam, S., and Prasanna, M.: Supplement of missing data in groundwater-level variations of peak type using geostatistical methods, GIS and geostatistical techniques for groundwater science, pp. 33–41, 2019.

Chuvieco, E.: Fundamentals of satellite remote sensing: An environmental approach, CRC press, 2020.

Council, N. R. et al.: Basic research opportunities in earth science, National Research Council, pp. 1–68, 2001.

Després, V., Huffman, J. A., Burrows, S. M., Hoose, C., Safatov, A., Buryak, G., Fröhlich-Nowoisky, J., Elbert, W., Andreae, M., Pöschl, U., et al.: Primary biological aerosol particles in the atmosphere: a review, Tellus B: Chemical and Physical Meteorology, 64, 15 598, 2012.

Di Iorio, T., Di Sarra, A., Sferlazzo, D., Cacciani, M., Meloni, D., Monteleone, F., Fuà, D., and Fiocco, G.: Seasonal evolution of the tropospheric aerosol vertical profile in the central Mediterranean and role of desert dust, Journal of Geophysical Research: Atmospheres, 114, 2009.

Diner, D. J., Ackerman, T. P., Anderson, T. L., Bsenberg, J., Braverman, A. J., Charlson, R. J., Collins, W. D., Davies, R., Holben, B. N., Hostetler, C. A., et al.: Progressive

Aerosol Retrieval and Assimilation Global Observing Network (PARAGON): An integrated approach for characterizing aerosol climatic and environmental interactions, Bull. Amer. Meteo. Soc, 85, 1491–1501, 2004.

Draxler, R. and Rolph, G.: Hybrid single-particle Lagrangian integrated trajectory HYSPLIT, Model, NOAA Air Resources Laboratory, Silver Spring, MD Available at: http://www. arl. noaa. gov/ready/hysplit4. html, 2003.

Duffney, P., Stanek, L., and Brown, J.: Air pollution: Sources, regulation, and health effects, Encyclopedia of Toxicology, 2023.

Duy, V. V., Ouillon, S., and Minh, H. N.: Sea surface temperature trend analysis by Mann-Kendall test and sen's slope estimator: a study of the Hai Phong coastal area (Vietnam) for the period 1995-2020, Science of the Earth, 44, 73–91, 2022.

Ebner, H., Kornus, W., Ohlhof, T., et al.: GG... REMOTE SENSING, ISPRS Journal of Photogrammetry & Remote Sensing, 54, 332–341, 1999.

Elansky, N. F., Ponomarev, N. A., and Verevkin, Y. M.: Air quality and pollutant emissions in the Moscow megacity in 2005–2014, Atmospheric Environment, 175, 54–64, 2018.

Engledew, J.: Cosmos and Man: A Scientific History, Algora Publishing, 2018.

Eshet, A. and Raju, J. P.: Daily and Seasonal Variation of Aerosol Optical Depth and Angstrom Exponent over Ethiopia using MODIS Data, Pollution, 8, 315–329, 2022.

Falah, S., Mhawish, A., Omar, A. H., Sorek-Hamer, M., Lyapustin, A. I., Banerjee, T., Kizel, F., and Broday, D. M.: Intercomparison of aerosol types reported as part of aerosol product retrieval over diverse geographic regions, Remote Sensing, 14, 3667, 2022a.

Falah, S., Mhawish, A., Omar, A. H., Sorek-Hamer, M., Lyapustin, A. I., Banerjee, T., Kizel, F., and Broday, D. M.: Intercomparison of aerosol types reported as part of aerosol product retrieval over diverse geographic regions, Remote Sensing, 14, 3667, 2022b.

Fan, J., Comstock, J. M., and Ovchinnikov, M.: The cloud condensation nuclei and ice nuclei effects on tropical anvil characteristics and water vapor of the tropical tropopause layer, Environmental Research Letters, 5, 044 005, 2010.

Feng, Y., Chen, D., Ouyang, X., and Zhang, X.: Variability of satellite-based total aerosols and the relationship with emission, meteorology and landscape in North China during 2000–2016, Environmental Earth Sciences, 77, 1–11, 2018.

Ferronato, N. and Torretta, V.: Waste mismanagement in developing countries: A review of global issues, International journal of environmental research and public health, 16, 1060, 2019.

Fiedler, S., Schepanski, K., Knippertz, P., Heinold, B., and Tegen, I.: How important are atmospheric depressions and mobile cyclones for emitting mineral dust aerosol in North Africa?, Atmospheric Chemistry and Physics, 14, 8983–9000, 2014.

Filioglou, M., Giannakaki, E., Backman, J., Kesti, J., Hirsikko, A., Engelmann, R., O'Connor, E., Leskinen, J. T., Shang, X., Korhonen, H., et al.: Optical and geometrical aerosol particle properties over the United Arab Emirates, Atmospheric Chemistry and Physics, 20, 8909–8922, 2020.

Filonchyk, M., Hurynovich, V., and Yan, H.: Trends in aerosol optical properties over Eastern Europe based on MODIS-Aqua, Geoscience frontiers, 11, 2169–2181, 2020.

Fowler, D., Pilegaard, K., Sutton, M., Ambus, P., Raivonen, M., Duyzer, J., Simpson, D., Fagerli, H., Fuzzi, S., Schjoerring, J., et al.: Atmospheric composition change: ecosystems–atmosphere interactions, Atmospheric Environment, 43, 5193–5267, 2009.

Froyd, K., Murphy, D., Sanford, T., Thomson, D., Wilson, J., Pfister, L., and Lait, L.: Aerosol composition of the tropical upper troposphere, Atmospheric Chemistry and Physics, 9, 4363–4385, 2009.

Gaffney, J. S., Marley, N. A., et al.: Urban aerosols and their impacts: lessons learned from the World Trade Center Tragedy, American Chemical Society, 2006a.

Gaffney, J. S., Marley, N. A., et al.: Urban aerosols and their impacts: lessons learned from the World Trade Center Tragedy, American Chemical Society, 2006b.

Gehlot, S., Minnett, P. J., and Stammer, D.: Impact of Sahara dust on solar radiation at Cape Verde Islands derived from MODIS and surface measurements, Remote Sensing of Environment, 166, 154–162, 2015.

Getachew, A.: The Study of Aerosol Microphysical and Optical Parameters, Total Columnar Ozone and Water Vapor Content Derived From Sunphotometer, Ph.D. thesis, Addis Ababa University, 2009.

Getachew, B., Manjunatha, B., and Bhat, H. G.: Spatio-temporal distribution of aerosol optical depth and cloud properties over Lake Tana Basin, Upper Blue Nile River Basin, Ethiopia, Remote Sensing Applications: Society and Environment, 20, 100 401, 2020.

Gheorghe, I. F. and Ion, B.: The effects of air pollutants on vegetation and the role of vegetation in reducing atmospheric pollution, The impact of air pollution on health, economy, environment and agricultural sources, 29, 241–80, 2011.

Gitau, W., Ogallo, L., Camberlin, P., and Okoola, R.: Spatial coherence and potential predictability assessment of intraseasonal statistics of wet and dry spells over Equatorial Eastern Africa, International Journal of Climatology, 33, 2690–2705, 2013.

Graf, H.-F., Feichter, J., and Langmann, B.: Volcanic sulfur emissions: Estimates of

source strength and its contribution to the global sulfate distribution, Journal of Geophysical Research: Atmospheres, 102, 10 727–10 738, 1997.

Grythe, H.: Quantification of sources and removal mechanisms of atmospheric aerosol particles, Ph.D. thesis, Department of Environmental Science and Analytical Chemistry, Stockholm ..., 2017.

Gundel, L., Guyot-Sionnest, N., and Novakov, T.: A study of the interaction of NO_2 with carbon particles, Aerosol science and technology, 10, 343–351, 1989.

Habib, A., Chen, B., Khalid, B., Tan, S., Che, H., Mahmood, T., Shi, G., and Butt, M. T.: Estimation and inter-comparison of dust aerosols based on MODIS, MISR and AERONET retrievals over Asian desert regions, Journal of Environmental Sciences, 76, 154–166, 2019.

Hall, P. and Ooi, H.: Attributing a probability to the shape of a probability density, The Annals of Statistics, 32, 2098–2123, 2004.

Hansen, T. F., Pienaar, J., and Orzack, S. H.: A comparative method for studying adaptation to a randomly evolving environment, Evolution, 62, 1965–1977, 2008.

Hansson, K. v. S., Skov, H., Andrews, E., Quinn, P. K., and Lucia, M.: Pan-Arctic seasonal cycles and long-term trends of aerosol properties from ten observatories, Atmospheric Chemistry and Physics, 2021.

Hartz, K. H., Hatfield, M., and Amin, H.: Speciation of Ultrafine Particulate Matter Formed via Ozonolysis of Household Volatile Organic Compounds, Aerosol Chemistry and Physics, 2007.

Harvey, A. and Oryshchenko, V.: Kernel density estimation for time series data, International journal of forecasting, 28, 3–14, 2012.

Haywood, J. and Boucher, O.: Estimates of the direct and indirect radiative forcing due to tropospheric aerosols: A review, Reviews of geophysics, 38, 513–543, 2000.

Held, I. M. and Soden, B. J.: Water vapor feedback and global warming, Annual review of energy and the environment, 25, 441–475, 2000.

Helsel, D. R. and Frans, L. M.: Regional Kendall test for trend, Environmental science & technology, 40, 4066–4073, 2006.

Hidy, G.: Aerosols: an industrial and environmental science, Elsevier, 2012.

Hirsch, R. M., Slack, J. R., and Smith, R. A.: Techniques of trend analysis for monthly water quality data, Water resources research, 18, 107–121, 1982.

Hobbs, P. V., Bowdle, D. A., and Radke, L. F.: Particles in the lower troposphere over the high plains of the United States. Part I: Size distributions, elemental compositions and morphologies, Journal of climate and applied meteorology, pp. 1344–1356, 1985.

Homa, M. G., Tsidu, G. M., and Nega, D. T.: Stratospheric Aerosol Climatology over Ethiopia and Retrieval of its Size Distribution, Atmospheric Chemistry and Physics Discussions, pp. 1–14, 2017.

Hopkins, K. D. and Weeks, D. L.: Tests for normality and measures of skewness and kurtosis: Their place in research reporting, Educational and psychological measurement, 50, 717–729, 1990.

Hoppel, W.: Measurement of the size distribution and CCN supersaturation spectrum of submicron aerosols over the ocean, Journal of Atmospheric Sciences, 36, 2006–2015, 1979.

Huang, J., Fu, Q., Su, J., Tang, Q., Minnis, P., Hu, Y., Yi, Y., and Zhao, Q.: Taklimakan dust aerosol radiative heating derived from CALIPSO observations using the Fu-Liou

radiation model with CERES constraints, Atmospheric Chemistry and Physics, 9, 4011–4021, 2009.

Huang, J., Bu, L., Kumar, K. R., Khan, R., and Devi, N. L.: Investigating the relationship between aerosol and cloud optical properties inferred from the MODIS sensor in recent decades over East China, Atmospheric Environment, 239, 117 812, 2020.

Indeje, M., Semazzi, F. H., and Ogallo, L. J.: ENSO signals in East African rainfall seasons, International Journal of Climatology: A Journal of the Royal Meteorological Society, 20, 19–46, 2000.

Ininda, J. M.: Numerical simulation of the influence of the sea surface temperature anomalies on the east African seasonal: rainfall, Ph.D. thesis, University of Nairobi Research Archive, URL `http://erepository.uonbi.ac.ke:8080/`, 1994.

Izenman, A. J.: Modern multivariate statistical techniques, Regression, classification and manifold learning, 10, 978–0, 2008.

Jaenicke, R.: Tropospheric aerosols, in: International geophysics, vol. 54, pp. 1–31, Elsevier, 1993.

Jian-Ping, H., Zhong-Wei, H., Jian-Rong, B., Wu, Z., and Lei, Z.: Micro-pulse lidar measurements of aerosol vertical structure over the Loess Plateau, Atmospheric and oceanic science Letters, 1, 8–11, 2008.

Jiang, T., Su, B., and Hartmann, H.: Temporal and spatial trends of precipitation and river flow in the Yangtze River Basin, 1961–2000, Geomorphology, 85, 143–154, 2007.

Jin, J., Henzing, B., and Segers, A.: How aerosol size matters in aerosol optical depth (AOD) assimilation and the optimization using the Ångström exponent, Atmospheric Chemistry and Physics, 23, 1641–1660, 2023.

Johnson, B., Shine, K., and Forster, P.: The semi-direct aerosol effect: Impact of absorbing aerosols on marine stratocumulus, Quarterly Journal of the Royal Meteorological Society, 130, 1407–1422, 2004.

Joksić, J. D., Jovašević-Stojanović, M., Bartonova, A., Radenković, M., Yttri, K.-E., Matić-Besarabić, S., and Ignjatović, L. M.: Physical and chemical characterization of the particulate matter suspended in aerosols from the urban area of Belgrade, Journal of the serbian chemical society, 74, 1319–1333, 2009.

Joshi, H., Naja, M., Srivastava, P., Gupta, T., Gogoi, M. M., and Suresh Babu, S.: Long-Term Trends in Black Carbon and Aerosol Optical Depth Over the Central Himalayas: Potential Causes and Implications, Frontiers in Earth Science, 10, 851 444, 2022.

Jung, J., Souri, A. H., Wong, D. C., Lee, S., Jeon, W., Kim, J., and Choi, Y.: The impact of the direct effect of aerosols on meteorology and air quality using aerosol optical depth assimilation during the KORUS-AQ campaign, Journal of Geophysical Research: Atmospheres, 124, 8303–8319, 2019.

Kafle, D. and Coulter, R.: Micropulse lidar-derived aerosol optical depth climatology at ARM sites worldwide, Journal of Geophysical Research: Atmospheres, 118, 7293–7308, 2013.

Kalisa, W., Zhang, J., Igbawua, T., Henchiri, M., Mulinga, N., Nibagwire, D., and Umuhoza, M.: Spatial and temporal heterogeneity of air pollution in East Africa, Science of The Total Environment, 886, 163 734, 2023.

Kaufman, Y. J., Fraser, R. S., and Ferrare, R. A.: Satellite measurements of large-scale air pollution: Methods, Journal of Geophysical Research: Atmospheres, 95, 9895–9909, 1990.

Kaufman, Y. J., Holben, B. N., Tanré, D., Slutsker, I., Smirnov, A., and Eck, T. F.: Will aerosol measurements from Terra and Aqua polar orbiting satellites represent the

daily aerosol abundance and properties?, Geophysical Research Letters, 27, 3861–3864, 2000a.

Kaufman, Y. J., Holben, B. N., Tanré, D., Slutsker, I., Smirnov, A., and Eck, T. F.: Will aerosol measurements from Terra and Aqua polar orbiting satellites represent the daily aerosol abundance and properties?, Geophysical Research Letters, 27, 3861–3864, 2000b.

Kaufman, Y. J., Tanré, D., and Boucher, O.: A satellite view of aerosols in the climate system, Nature, 419, 215–223, 2002.

Kaur, M., Mishra, V., and Sharma, J.: Effects of topographic corrections on snow cover monitoring in Himalayan terrain using MODIS data, International Journal of Engineering Research and Technlogy, 1, 1–8, 2012.

Kerényi, A., McIntosh, R. W., Kerényi, A., and McIntosh, R. W.: Structure and Operation of Systems, Models of the Global Earth System, Sustainable Development in Changing Complex Earth Systems, 27, 11–58, 2020.

Khain, A., Rosenfeld, D., and Pokrovsky, A.: Aerosol impact on the dynamics and microphysics of deep convective clouds, Quarterly Journal of the Royal Meteorological Society: A journal of the atmospheric sciences, applied meteorology and physical oceanography, 131, 2639–2663, 2005.

Khamala, G. W., Makokha, J. W., Boiyo, R., and Kumar, K. R.: Long-term climatology and spatial trends of absorption, scattering, and total aerosol optical depths over East Africa during 2001–2019, Environmental Science and Pollution Research, 29, 61 283–61 297, 2022.

Khan, R., Kumar, K. R., Zhao, T., Ullah, W., and de Leeuw, G.: Interdecadal changes in aerosol optical depth over Pakistan based on the MERRA-2 reanalysis data during 1980–2018, Remote Sensing, 13, 822, 2021.

Kharol, S. K., Badarinath, K., Sharma, A. R., Kaskaoutis, D., and Kambezidis, H.: Multiyear analysis of Terra/Aqua MODIS aerosol optical depth and ground observations over tropical urban region of Hyderabad, India, Atmospheric environment, 45, 1532–1542, 2011.

Khattak, M. S., Babel, M., and Sharif, M.: Hydro-meteorological trends in the upper Indus River basin in Pakistan, Climate research, 46, 103–119, 2011.

Khedidji, S., Müller, K., Rabhi, L., Spindler, G., Fomba, K. W., van Pinxteren, D., Yassaa, N., Herrmann, H., et al.: Chemical Characterization of Marine Aerosols in a South Mediterranean Coastal Area Located in Bou Ismaïl, Algeria, Aerosol and Air Quality Research, 20, 2448–2473, 2020.

Kim, B.-G., Schwartz, S. E., Miller, M. A., and Min, Q.: Effective radius of cloud droplets by ground-based remote sensing: Relationship to aerosol, Journal of Geophysical Research: Atmospheres, 108, 2003.

Kokhanovsky, A. A.: Aerosol optics: light absorption and scattering by particles in the atmosphere, Springer Science & Business Media, 2008.

Koutsenogii, P. K. and Jaenicke, R.: Number concentration and size distribution of atmospheric aerosol in Siberia, Journal of aerosol science, 25, 377–383, 1994.

Kumar, K. R., Yin, Y., Sivakumar, V., Kang, N., Yu, X., Diao, Y., Adesina, A. J., and Reddy, R.: Aerosol climatology and discrimination of aerosol types retrieved from MODIS, MISR and OMI over Durban (29.88 S, 31.02 E), South Africa, Atmospheric Environment, 117, 9–18, 2015.

Kummerow, C., Simpson, J., Thiele, O., Barnes, W., Chang, A., Stocker, E., Adler, R., Hou, A., Kakar, R., Wentz, F., et al.: The status of the Tropical Rainfall Measuring Mission (TRMM) after two years in orbit, Journal of Applied Meteorology and Climatology, 39, 1965–1982, 2000.

LeBlanc, S. E., Redemann, J., Flynn, C., Pistone, K., Kacenelenbogen, M., Segal-Rosenheimer, M., Shinozuka, Y., Dunagan, S., Dahlgren, R. P., Meyer, K., et al.: Above-cloud aerosol optical depth from airborne observations in the southeast Atlantic, Atmospheric Chemistry and Physics, 20, 1565–1590, 2020.

Ledesma, R. D. and Valero-Mora, P.: Determining the number of factors to retain in EFA: An easy-to-use computer program for carrying out parallel analysis, Practical assessment, research, and evaluation, 12, 2, 2019.

Lee, H.-T., Gruber, A., Ellingson, R. G., and Laszlo, I.: Development of the HIRS outgoing longwave radiation climate dataset, Journal of Atmospheric and Oceanic Technology, 24, 2029–2047, 2007.

Lee, J., Kim, J., Song, C., Kim, S., Chun, Y., Sohn, B., and Holben, B.: Characteristics of aerosol types from AERONET sunphotometer measurements, Atmospheric Environment, 44, 3110–3117, 2010.

Lenhardt, N. and Oppenheimer, C.: Volcanism in Africa: geological perspectives, hazards, and societal implications, Extreme Natural Hazards, Disaster Risks and Societal Implications, 1, 169, 2014.

Levelt, P. F., Veefkind, J., and Boersma, K.: Trace gases, troposphere-detection from space, Journal of the Atmospheric Sciences, 56, 127–150, 2014.

Li, H., Zhang, M., Wang, L., Ma, Y., Qin, W., and Gong, W.: The effect of aerosol on downward diffuse radiation during winter haze in Wuhan, China, Atmospheric Environment, 265, 118 714, 2021a.

Li, H., Zhang, M., Wang, L., Ma, Y., Qin, W., and Gong, W.: The effect of aerosol on downward diffuse radiation during winter haze in Wuhan, China, Atmospheric Environment, 265, 118 714, 2021b.

Li, J., Min, Q., Peng, Y., Sun, Z., and Zhao, J.-Q.: Accounting for dust aerosol size distribution in radiative transfer, Journal of Geophysical Research: Atmospheres, 120, 6537–6550, 2015a.

Li, J., Min, Q., Peng, Y., Sun, Z., and Zhao, J.-Q.: Accounting for dust aerosol size distribution in radiative transfer, Journal of Geophysical Research: Atmospheres, 120, 6537–6550, 2015b.

Li, J., Ge, X., He, Q., and Abbas, A.: Aerosol optical depth (AOD): spatial and temporal variations and association with meteorological covariates in Taklimakan desert, China, PeerJ, 9, e10 542, 2021c.

Li, Z., Lau, W.-M., Ramanathan, V., Wu, G., Ding, Y., Manoj, M., Liu, J., Qian, Y., Li, J., Zhou, T., et al.: Aerosol and monsoon climate interactions over Asia, Reviews of geophysics, 54, 866–929, 2016.

Li, Z., Rosenfeld, D., and Fan, J.: Aerosols and their impact on radiation, clouds, precipitation, and severe weather events, in: Oxford Research Encyclopedia of Environmental Science, Oxford Research Encyclopedia of Environmental Science, 2017.

Liou, K.-N.: An introduction to atmospheric radiation, vol. 84, Elsevier, 2002.

Lippmann, M.: Environmental toxicants: human exposures and their health effects, New York University School of Medicine, 2000.

Liu, C., Chung, C. E., Yin, Y., and Schnaiter, M.: The absorption Ångström exponent of black carbon: from numerical aspects, Atmospheric Chemistry and Physics, 18, 6259–6273, 2018.

Liu, H., Koren, I., and Altaratz, O.: Observed decreasing trend in the upper-tropospheric cloud top temperature, npj Climate and Atmospheric Science, 6, 142, 2023.

Liu, Y., Lin, T., Hong, J., Wang, Y., Shi, L., Huang, Y., Wu, X., Zhou, H., Zhang, J., and de Leeuw, G.: Multi-dimensional satellite observations of aerosol properties and aerosol types over three major urban clusters in eastern China, Atmospheric Chemistry and Physics, 21, 12 331–12 358, 2021.

Loeb, N. G., Doelling, D. R., Wang, H., Su, W., Nguyen, C., Corbett, J. G., Liang, L., Mitrescu, C., Rose, F. G., and Kato, S.: Clouds and the earth's radiant energy system (CERES) energy balanced and filled (EBAF) top-of-atmosphere (TOA) edition-4.0 data product, Journal of Climate, 31, 895–918, 2018.

Lu, H., Xie, M., Liu, B., Liu, X., Feng, J., Yang, F., Zhao, X., You, T., Wu, Z., and Gao, Y.: Impact of atmospheric thermodynamic structures and aerosol radiation feedback on winter regional persistent heavy particulate pollution in the Sichuan-Chongqing region, China, Science of the Total Environment, 842, 156 575, 2022.

Makokha, J. W., Odhiambo, J. O., et al.: Trend analysis of aerosol optical depth and angström exponent anomaly over East Africa, Atmospheric and Climate Sciences, 7, 588–603, 2017a.

Makokha, J. W., Odhiambo, J. O., et al.: Trend analysis of aerosol optical depth and angström exponent anomaly over East Africa, Atmospheric and Climate Sciences, 2017b.

Manisalidis, I., Stavropoulou, E., Stavropoulos, A., and Bezirtzoglou, E.: Environmental and health impacts of air pollution: a review, Frontiers in public health, 8, 14, 2020.

Marchand, K., Roosen, I., Reinold, J., and Siegel, M.: Irregular Migration from and in the East and Horn of Africa, Maastricht Grduate School of Governance, 2017.

Marchand, R., Ackerman, T., Smyth, M., and Rossow, W. B.: A review of cloud top height and optical depth histograms from MISR, ISCCP, and MODIS, Journal of Geophysical Research: Atmospheres, 115, 2010.

Matthias, V., Balis, D., Bösenberg, J., Eixmann, R., Iarlori, M., Komguem, L., Mattis, I., Papayannis, A., Pappalardo, G., Perrone, M., et al.: Vertical aerosol distribution over Europe: Statistical analysis of Raman lidar data from 10 European Aerosol Research Lidar Network (EARLINET) stations, Journal of Geophysical Research: Atmospheres, 109, 2004.

McLeod, A. I.: Kendall rank correlation and Mann-Kendall trend test, R Package Kendall, 602, 1–10, 2005.

Mohammad, L., Mondal, I., Bandyopadhyay, J., Pham, Q. B., Nguyen, X. C., Dinh, C. D., and Al-Quraishi, A. M. F.: Assessment of spatio-temporal trends of satellite-based aerosol optical depth using Mann–Kendall test and Sen's slope estimator model, Geomatics, Natural Hazards and Risk, 13, 1270–1298, 2022.

Mukai, S.: Remote sensing of heavy aerosol pollution episodes: Smoke and dust, in: Remote Sensing of Aerosols, Clouds, and Precipitation, pp. 85–108, Elsevier, 2018.

Mushtaq, Z., Sharma, M., Bangotra, P., Gautam, A. S., and Gautam, S.: Atmospheric aerosols: some highlights and highlighters, past to recent years, Aerosol Science and Engineering, 6, 135–145, 2022.

Myhre, G., Stordal, F., Johnsrud, M., Kaufman, Y., Rosenfeld, D., Storelvmo, T., Kristjansson, J. E., Berntsen, T. K., Myhre, A., and Isaksen, I. S.: Aerosol-cloud interaction inferred from MODIS satellite data and global aerosol models, Atmospheric Chemistry and Physics, 7, 3081–3101, 2007a.

Myhre, G., Stordal, F., Johnsrud, M., Kaufman, Y., Rosenfeld, D., Storelvmo, T., Kristjansson, J. E., Berntsen, T. K., Myhre, A., and Isaksen, I. S.: Aerosol-cloud interaction inferred from MODIS satellite data and global aerosol models, Atmospheric Chemistry and Physics, 7, 3081–3101, 2007b.

Myhre, G., Myhre, C., Samset, B., and Storelvmo, T.: Aerosols and their relation to global climate and climate sensitivity, Nature Education Knowledge, 4, 7, 2013.

Nasri, M. and Modarres, R.: Dry spell trend analysis of Isfahan Province, Iran, International Journal of Climatology: A Journal of the Royal Meteorological Society, 29, 1430–1438, 2009.

Negash, L.: Ethiopias Indigenous Trees, Addis Ababa University, Press, Addis Ababa, 2010.

Ngaina, J. N.: Modelling aerosol-cloud-precipitation interactions for weather modification in East Africa, Ph.D. thesis, University of Nairobi, 2015.

Ngaina, J. N., Mutai, B., Ininda, J., and Muthama, J.: Monitoring spatial-temporal variability of aerosol over Kenya, Ethiopian Journal of Environmental Studies and Management, 7, 244–252, 2014.

Nicolae, V., Talianu, C., Andrei, S., Antonescu, B., Ene, D., Nicolae, D., Dandocsi, A., Toader, V.-E., Ștefan, S., Savu, T., et al.: Multiyear typology of long-range transported aerosols over Europe, Atmosphere, 10, 482, 2019.

Nourian, A., Abba, M. K., and Nasr, G. G.: Measurements and analysis of non-methane VOC (NMVOC) emissions from major domestic aerosol sprays at "source", Environment International, 146, 106–152, 2021.

Okabe, A., Satoh, T., and Sugihara, K.: A kernel density estimation method for networks, its computational method and a GIS-based tool, International Journal of Geographical Information Science, 23, 7–32, 2009.

Okuda, T.: Measurement of the specific surface area and particle size distribution of atmospheric aerosol reference materials, Atmospheric Environment, 75, 1–5, 2013.

Ostertagová, E.: Modelling using polynomial regression, Procedia Engineering, 48, 500–506, 2012.

Park, M., Hu, H., Kim, Y., Fried, A., Simpson, I. J., Jin, H., Weinheimer, A., Huey, G., Crawford, J., and Woo, J.-H.: Evaluation of the emission inventory for large point emission sources in South Korea by applying measured data from the NASA/NIER KORUS-AQ aircraft field campaign, Elementa: Science of the Anthropocene, 11, 2023.

Partal, T. and Kahya, E.: Trend analysis in Turkish precipitation data, Hydrological Processes: An International Journal, 20, 2011–2026, 2006.

Patakamuri, S. K., Muthiah, K., and Sridhar, V.: Long-term homogeneity, trend, and change-point analysis of rainfall in the arid district of Ananthapuramu, Andhra Pradesh State, India, Water, 12, 211, 2020.

Patel, M. P. and Application, S.: Study of Aerosol Optical Depth and Black Carbon concentration over Dehradun and surroundings, Indian Institute of Remote Sensing,(ISRO), 2016.

Pathak, B., Bhuyan, P. K., Gogoi, M., and Bhuyan, K.: Seasonal heterogeneity in aerosol types over Dibrugarh-North-Eastern India, Atmospheric environment, 47, 307–315, 2012.

Penner, J. E., Zhang, S. Y., and Chuang, C. C.: Soot and smoke aerosol may not warm climate, Journal of Geophysical Research: Atmospheres, 108, 2003.

Pilewskie, P.: Climate change: Aerosols heat up, Nature, 448, 541–542, 2007.

Piyush, P. M. and S, A.: Study of Aerosol Optical Depth and Black Carbon concentration over Dehradun and surroundings, Ph.D. thesis, Indian Institute of Remote Sensing ISRO, 2016.

Popescu, F. and Ionel, I.: Anthropogenic air pollution sources, Air quality, pp. 1–22, 2010.

Pöschl, U.: Atmospheric aerosols: composition, transformation, climate and health effects, Angewandte Chemie International Edition, 44, 7520–7540, 2005.

Prospero, J., Charlson, R., Mohnen, V., Jaenicke, R., Delany, A., Moyers, J., Zoller, W., and Rahn, K.: The atmospheric aerosol system: An overview, Reviews of Geophysics, 21, 1607–1629, 1983.

Pruppacher, H. R., Klett, J. D., Pruppacher, H. R., and Klett, J. D.: Microstructure of atmospheric clouds and precipitation, Microphysics of clouds and precipitation, pp. 9–55, 1978.

Quaas, J.: Approaches to observe anthropogenic aerosol-cloud interactions, Current climate change reports, 1, 297–304, 2015.

Querol, X., Zhuang, X., Alastuey, A., Viana, M., Lv, W., Wang, Y., López, A., Zhu, Z., Wei, H., and Xu, S.: Speciation and sources of atmospheric aerosols in a highly industrialised emerging mega-city in Central China, Journal of Environmental Monitoring, 8, 1049–1059, 2006.

Raes, F., Van Dingenen, R., Vignati, E., Wilson, J., Putaud, J.-P., Seinfeld, J. H., and Adams, P.: Formation and cycling of aerosols in the global troposphere, Atmospheric environment, 34, 4215–4240, 2000.

Rahman, M. M.: Recommendations on the measurement techniques of atmospheric pollutants from in situ and satellite observations: a review, Arabian Journal of Geosciences, 16, 1–28, 2023.

Rizza, U., Mancinelli, E., Morichetti, M., Passerini, G., and Virgili, S.: Aerosol optical depth of the main aerosol species over Italian cities based on the NASA/MERRA-2 model reanalysis, Atmosphere, 10, 709, 2019.

Romero-Guzmán, E. T., Reyes-Gutiérrez, L. R., Romero-Guzmán, L., Hernández-Mendoza, H., Uría-Gómez, L. C., and Gutiérrez-Reyes, J.: An Overview of Bioaerosols Suspended in the Atmosphere of Metropolitan Zone of Toluca Valley, Journal of the Mexican Chemical Society, 65, 214–224, 2021.

Rosenfeld, D., Kaufman, Y., and Koren, I.: Switching cloud cover and dynamical regimes from open to closed Benard cells in response to the suppression of precipitation by aerosols, Atmospheric Chemistry and Physics, 6, 2503–2511, 2006.

Rosenfeld, D., Andreae, M. O., Asmi, A., Chin, M., de Leeuw, G., Donovan, D. P., Kahn, R., Kinne, S., Kivekäs, N., Kulmala, M., et al.: Global observations of aerosol-cloud-precipitation-climate interactions, Reviews of Geophysics, 52, 750–808, 2014.

Salau, O., Warneke, T., Notholt, J., Shim, C., Li, Q., and Xiao, Y.: Tropospheric trace gases at Bremen measured with FTIR spectrometry, Journal of Environmental Monitoring, 11, 1529–1534, 2009.

Samson, P.: Evolution of the atmosphere: composition, structure and energy, 2018.

Satheesh, S. and Moorthy, K. K.: Radiative effects of natural aerosols: A review, Atmospheric Environment, 39, 2089–2110, 2005.

Schanda, E.: Physical fundamentals of remote sensing, Springer Science & Business Media, 2012.

Shafique, A., Cao, G., Khan, Z., Asad, M., and Aslam, M.: Deep learning-based change detection in remote sensing images: A review, Remote Sensing, 14, 871, 2022.

Shekar, R. M. and Venkataraman, C.: Direct radiative forcing from anthropogenic carbonaceous aerosols over India, Current Science, 76, 1005–1011, 1999.

Shrestha, S. and Singh, P.: 1 Global Climate System, Energy Balance, and the Hydrological Cycle, Climate Change and Water Resources, p. 1, 2014.

Simpson, J., Kummerow, C., Tao, W. K., and Adler, R. F.: On the tropical rainfall measuring mission (TRMM), Meteorology and Atmospheric physics, 60, 19–36, 1996.

Sitch, S., Huntingford, C., Gedney, N., Levy, P., Lomas, M., Piao, S., Betts, R., Ciais, P., Cox, P., Friedlingstein, P., et al.: Evaluation of the terrestrial carbon cycle, future plant geography and climate-carbon cycle feedbacks using five Dynamic Global Vegetation Models (DGVMs), Global change biology, 14, 2015–2039, 2008.

Sneyers, R. et al.: On the statistical analysis of series of observations, 143, CABI Digital Liberary, 1991.

Sporre, M.: Aerosol-Cloud-Precipitation Interactions-Studied using combinations of remote sensing and in-situ data, Lund University, 2016.

Stephenson, D., Kumar, K. R., Doblas-Reyes, F., Royer, J., Chauvin, F., and Pezzulli, S.: Extreme daily rainfall events and their impact on ensemble forecasts of the Indian monsoon, Monthly Weather Review, 127, 1954–1966, 1999.

Su, W., Liang, L., Wang, H., and Eitzen, Z. A.: Uncertainties in CERES top-of-atmosphere fluxes caused by changes in accompanying imager, Remote Sensing, 12, 2040, 2020.

Symeonidis, P.: Study of spatial and temporal variation of atmospheric optical parameters and their relation with PM 2.5 concentration over Europe using GIS technologies, Master Thesis in Geographical Information Science, 2017.

Takemura, T., Okamoto, H., Maruyama, Y., Numaguti, A., Higurashi, A., and Nakajima, T.: Global three-dimensional simulation of aerosol optical thickness distribution of various origins, Journal of Geophysical Research: Atmospheres, 105, 17 853–17 873, 2000.

Tanré, D., Kaufman, Y., Herman, M., and Mattoo, S.: Remote sensing of aerosol properties over oceans using the MODIS/EOS spectral radiances, Journal of Geophysical Research: Atmospheres, 102, 16 971–16 988, 1997.

Taylor, J. R.: Assessment of trace gas observations from the Toronto Atmospheric Observatory, University of Toronto, 2008.

Tegen, I. and Fung, I.: Modeling of mineral dust in the atmosphere: Sources, transport, and optical thickness, Journal of Geophysical Research: Atmospheres, 99, 22 897–22 914, 1994.

Tegen, I., Lacis, A. A., and Fung, I.: The influence on climate forcing of mineral aerosols from disturbed soils, Nature, 380, 419–422, 1996.

Thapa, M., Bhattarai, B., Gurung, S., Sapkota, B., and Poudyal, K.: Diurnal and Monthly Variation of Aerosol Optical Depth and Angstrom's Parameters in Kathmandu Valley, Nepal, Research Journal of Chemical Sciences, 6, 40–44, 2016.

Tian, J. and Chen, D.: Spectral, spatial, and temporal sensitivity of correlating MODIS aerosol optical depth with ground-based fine particulate matter (PM2. 5) across southern Ontario, Canadian Journal of Remote Sensing, 36, 119–128, 2010.

Tian, Y., Duan, M., Cui, X., and Tian, S.: Advancing application of satellite remote sensing technologies for linking atmospheric and built environment to health, Frontiers in Public Health, 11, 270–330, 2023.

Toledano, C., Cachorro, V., Berjon, A., De Frutos, A., Sorribas, M., De la Morena, B., and Goloub, P.: Aerosol optical depth and Ångström exponent climatology at El Arenosillo AERONET site (Huelva, Spain), Quarterly Journal of the Royal Meteorological Society: A journal of the atmospheric sciences, applied meteorology and physical oceanography, 133, 795–807, 2007.

Tomasi, C. and Lupi, A.: Primary and secondary sources of atmospheric aerosol, Atmospheric Aerosols: Life Cycles and Effects on Air Quality and Climate, pp. 1–86, 2017.

Torres-Delgado, E., Baumgardner, D., and Mayol-Bracero, O. L.: Measurement report: Impact of African aerosol particles on cloud evolution in a tropical montane cloud forest in the Caribbean, Atmospheric Chemistry and Physics, 21, 18 011–18 027, 2021.

Trenberth, K. E.: Atmospheric moisture residence times and cycling: Implications for rainfall rates and climate change, Climatic change, 39, 667–694, 1998.

Twomey, S.: The influence of pollution on the shortwave albedo of clouds, Journal of the atmospheric sciences, 34, 1149–1152, 1977.

Twomey, S. A., Piepgrass, M., and Wolfe, T.: An assessment of the impact of pollution on global cloud albedo, Tellus B, 36, 356–366, 1984.

Vaquero-Martínez, J. and Antón, M.: Review on the role of GNSS meteorology in monitoring water vapor for atmospheric physics, Remote Sensing, 13, 2287, 2021.

Verma, S., Prakash, D., Soni, M., and Ram, K.: Atmospheric aerosols monitoring: Ground and satellite-based instruments, in: Advances in Environmental Monitoring and Assessment, p. 67, IntechOpen London, UK, 2019a.

Verma, S., Prakash, D., Soni, M., and Ram, K.: Atmospheric aerosols monitoring: Ground and satellite-based instruments, in: Advances in Environmental Monitoring and Assessment, p. 67, IntechOpen London, UK, 2019b.

Wang, Y., Ali, M. A., Bilal, M., Qiu, Z., Ke, S., Almazroui, M., Islam, M. M., and Zhang, Y.: Identification of aerosol pollution hotspots in Jiangsu Province of China, Remote Sensing, 13, 2842, 2021.

Washington, R. and Todd, M. C.: Atmospheric controls on mineral dust emission from the Bodélé Depression, Chad: The role of the low level jet, Geophysical Research Letters, 32, 2005.

Wassie, S. B.: Natural resource degradation tendencies in Ethiopia: a review, Environmental systems research, 9, 1–29, 2020.

Wielicki, B. A., Cess, R. D., King, M. D., Randall, D. A., and Harrison, E. F.: Mission to planet Earth: Role of clouds and radiation in climate, Bulletin of the American Meteorological Society, pp. 2125–2153, 1995.

Wielicki, B. A., Barkstrom, B. R., Baum, B. A., Charlock, T. P., Green, R. N., Kratz, D. P., Lee, R. B., Minnis, P., Smith, G. L., Wong, T., et al.: Clouds and the Earth's Radiant Energy System (CERES): algorithm overview, IEEE Transactions on Geoscience and Remote Sensing, 36, 1127–1141, 1998.

Williams, E., Rosenfeld, D., Madden, N., Gerlach, J., Gears, N., Atkinson, L., Dunnemann, N., Frostrom, G., Antonio, M., Biazon, B., et al.: Contrasting convective regimes over the Amazon: Implications for cloud electrification, Journal of Geophysical Research: Atmospheres, 107, LBA–50, 2002.

Wu, J., Zhang, S., Yang, Q., Zhao, D., Fan, W., Zhao, J., and Shen, C.: Using particle swarm optimization to improve visibility-aerosol optical depth retrieval method, npj Climate and Atmospheric Science, 4, 49, 2021.

Wu, Y., Guo, J., Zhang, X., Tian, X., Zhang, J., Wang, Y., Duan, J., and Li, X.: Synergy of satellite and ground based observations in estimation of particulate matter in eastern China, Science of the Total Environment, 433, 20–30, 2012.

Xu, S., Qin, M., Ding, S., Zhao, Q., Liu, H., Li, C., Yang, X., Li, Y., Yang, J., and Ji, X.: The impacts of climate variation and land use changes on streamflow in the Yihe River, China, Water, 11, 887, 2019.

Yang, X., Zhao, C., Yang, Y., and Fan, H.: Long-term multi-source data analysis about the characteristics of aerosol optical properties and types over Australia, Atmospheric Chemistry and Physics, 21, 3803–3825, 2021.

Yang, Y. and Di Girolamo, L.: Impacts of 3-D radiative effects on satellite cloud detection and their consequences on cloud fraction and aerosol optical depth retrievals, Journal of Geophysical Research: Atmospheres, 113, 2008.

Yang, Z., Wang, J., Ichoku, C., Hyer, E., and Zeng, J.: Mesoscale modeling and satellite observation of transport and mixing of smoke and dust particles over northern sub-Saharan African region, Journal of Geophysical Research: Atmospheres, 118, 12–139, 2013.

Young, T. M., Shaffer, L. B., Guess, F. M., Bensmail, H., and León, R. V.: A comparison of multiple linear regression and quantile regression for modeling the internal bond of medium density fiber-board, Forest Products Journal, 58, 39, 2008.

Yu, X., Nichol, J., Lee, K. H., Li, J., and Wong, M. S.: Analysis of Long-Term Aerosol Optical Properties Combining AERONET Sunphotometer and Satellite-Based Observations in Hong Kong, Remote Sensing, 14, 5220, 2022.

Zambom, A. Z. and Ronaldo, D.: A review of kernel density estimation with applications to econometrics, International Econometric Review, 5, 20–42, 2013.

Zarenistanak, M., Dhorde, A. G., and Kripalani, R.: Trend analysis and change point detection of annual and seasonal precipitation and temperature series over southwest Iran, Journal of earth system science, 123, 281–295, 2014.

Zhang, X., Li, P., and Li, D.: Spatiotemporal variations of precipitation in the southern part of the Heihe river basin (China), 1984–2014, Water, 10, 410, 2018.

Declaration

This dissertation thesis is my original work, has not been presented for a degree in any other University and that all the sources of material used for the thesis have been dully acknowledged.

Name: Ambachew Abeje Alemu

Signature: 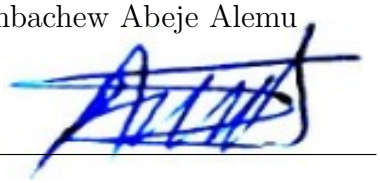

Place and time of submission: Bahir Dar University, July 2024

This thesis has been submitted for examination with my approval as University advisor.

Name: Dr. U. Jaya Prakash Raju

Signature: